RÉPUBLIQUE FRANÇAISE
Liberté Égalité Fraternité

Université de Toulouse

Doctorat de l'Université de Toulouse

préparé à l'ISAE-SUPAERO

Utilisation des mesures de phase pour positionnement précis dans un essaim de satellites

Thèse présentée et soutenue, le 6 février 2026 par

Joan Miguel BERNABEU FRIAS

École doctorale
EDMITT - Ecole Doctorale Mathématiques, Informatique et Télécommunications de Toulouse

Spécialité
Informatique et Télécommunications

Unité de recherche
ISAE-ONERA SCANR Signal communication Antennes Navigation Radar

Thèse dirigée par
Eric CHAUMETTE et Antoine BLAIS

Composition du jury
Mme Audrey GIREMUS, Présidente, Université de Bordeaux
M. Arnaud BRELOY, Rapporteur, Cnam Paris
M. Jean-Philippe OVARLEZ, Rapporteur, ONERA Palaiseau
M. Eric CHAUMETTE, Directeur de thèse, ISAE-SUPAERO
M. Antoine BLAIS, Co-directeur de thèse, ENAC

Membres invités
M. Yoan GREGOIRE, CNES
M. Lorenzo ORTEGA ESPLUGA, Co-encadrant, IPSA

Precise Positioning Using Carrier-Phase Measurements in a Swarm of Satellites

Auteur :
M. Joan Bernabeu

Encadrants :
Pr. Éric Chaumette
Pr. Lorenzo Ortega
Pr. Antoine Blais
M. Yoan Grégoire

Version 0.1 du
February 9, 2026

Acknowledgements

I would like to express my sincere gratitude to my thesis advisors for their invaluable guidance throughout this research. To Eric Chaumette, thank you for your patient support, for kindly correcting my mistakes while generously sharing your extensive knowledge, and for your crucial role in the publication process, providing corrections that took me time to internalize and progressively helping me understand how to write proper research papers. To Yoan Grégoire, thank you for your genuine curiosity in my work and your broad knowledge that enriched our discussions. To Antoine Blais, thank you for your practical tips and, together with Yoan, for proposing implementation ideas that made simulations more manageable. In particular, to Lorenzo Ortega, thank you for sitting next to me to analyze from scratch the challenges I faced throughout this research. Thank you for never making me feel embarrassed about any question, regardless of how fundamental it was, creating a safe space where I could truly learn without fear of judgment. Thank you, together with Eric, for reviewing in detail the mathematics and derivations I developed, helping me identify and solve the issues I encountered. Your approach to research and mentorship has been exemplary, and I aspire to follow your lead as a researcher.

Thank you to Professor Pau Closas for hosting me in your lab at Northeastern University. Your approach to research, combining technical expertise with genuine curiosity, has influenced my perspective on academic work. You showed me that great research can coexist with kindness and collaboration, and that engaging with students as equals creates a rich learning environment.

To my friends and family in Mataró, who welcomed me home every visit as if I'd never left. Thank you for celebrating my successes and always counting on me despite the distance. Despite my best efforts to explain my research, I suspect you'll all continue telling people I do "something with satellites and mathematics", and honestly, I prefer it that way. What matters most is that you gave me your unwavering support, for which I am deeply grateful.

To my Toulousain friends, who proved their friendship when my PhD contract was extended but my lease was not, thank you for opening your homes when I needed them. My Bostonian friends and labmates deserve a special mention; thank you for embracing me from the moment I arrived. The only downside is that now I'll miss you from across the ocean.

Finally, to my grandfather Miguel, Abuelito, who recently passed away as I was giving this manuscript its final corrections. He lived a long, full life, rising from extreme poverty to achieve a peaceful retirement in his beloved Cordoba. Like my own path, his journey led him to France as an emigrant, where he worked far from his loved ones to provide for his family. He devoted himself to ensuring his descendants would have access to education and opportunities beyond the demanding agricultural labor that defined his experience. He never complained when faced with adversity, choosing instead to focus on overcoming challenges rather than being overwhelmed by them. This resilience taught me to endure, and showed me that most difficulties I encounter are largely matters of perspective. His example has shaped me, and I dedicate this thesis to his memory.

Abstract — This thesis investigates carrier-phase enhanced time-delay estimation techniques for achieving centimeter-level inter-satellite ranging accuracy required by the NOIRE mission, a distributed radio interferometry system devised to operate in lunar orbit. The research addresses the fundamental challenge of exploiting carrier-phase information to improve ranging precision beyond conventional methods, which are limited to meter-level accuracy. The theoretical framework develops through three complementary analyses. First, the Conditional Signal Model is revisited explicitly accounting for the hardware-induced and propagation-induced phase components. While these terms were previously thought to be individually unidentifiable, this work demonstrates they can be uniquely determined under appropriate signal structure conditions. This enables the treatment of hardware phase to assess the potential of full propagation phase exploitation. Second, perfect hardware phase compensation is analyzed to establish the theoretical performance limit, representing the optimal case approachable only in specific scenarios. This analysis reveals orders-of-magnitude improvements through quadratic dependence on carrier frequency. It identifies five distinct operational regions of the Maximum Likelihood Estimator, extending the three regions previously reported in literature. The effects of Doppler, carrier frequency, and sampling frequency variations on estimation performance are systematically characterized. Third, the framework addresses realistic scenarios where phase measurements contain quantifiable uncertainty. A statistically optimal phase-aware estimator is developed through rigorous likelihood maximization. Novel results show performance transitions between conventional and optimal bounds based on phase observation quality. These are compared against both conventional methods and a naive engineering implementation that directly applies phase measurements without statistical weighting. The analysis reveals that under phase uncertainty, both phase-aware and naive implementations converge to a plateau at an error level determined by the uncertainty. Each 10 decibel increase in phase uncertainty elevates plateau levels by approximately 10 decibels, demonstrating a 1:1 correspondence between calibration quality and fundamental performance limits. The naive implementation remains at this error level for any SNR value. In contrast, the phase-aware implementation remains attached to the bound longer, even reaching lower error levels for a short SNR interval, before eventually detaching to form a second plateau at very high SNR. Monte Carlo simulations using GPS L1 C/A and Kasami sequences validate theoretical predictions. They establish quantitative relationships between calibration requirements and achievable accuracy. The results demonstrate that carrier-phase exploitation can theoretically achieve NOIRE mission requirements, though practical implementation requires signal-to-noise ratios exceeding 40 dB for the tested configurations. This analysis provides essential information for mission planning and enables exploration of alternative configurations. It establishes fundamental trade-offs between calibration quality, computational complexity, and system performance.

Keywords: Cramér-Rao bound, time-delay and Doppler estimation, band-limited signals, maximum likelihood estimator

Résumé — Cette thèse étudie les techniques d'estimation de retard temporel améliorées par la phase porteuse pour atteindre une précision de télémétrie inter-satellites au niveau centimétrique requise par la mission NOIRE, un système d'interférométrie radio distribué conçu pour opérer en orbite lunaire. La recherche aborde le défi fondamental d'exploiter l'information de phase porteuse pour améliorer la précision de télémétrie au-delà des méthodes conventionnelles, qui sont limitées à une précision métrique. Le cadre théorique se développe à travers trois analyses complémentaires. Premièrement, le modèle de signal conditionnel est revisité en tenant compte explicitement des composantes de phase induites par le matériel et par la propagation. Alors que ces termes étaient précédemment considérés comme individuellement non identifiables, ce travail démontre qu'ils peuvent être déterminés de manière unique sous des conditions de structure de signal appropriées. Cela permet le traitement de la phase matérielle pour évaluer le potentiel d'exploitation complète de la phase de propagation. Deuxièmement, la compensation parfaite de la phase matérielle est analysée pour établir la limite de performance théorique, représentant le cas optimal approchable uniquement dans des scénarios spécifiques. Cette analyse révèle des améliorations de plusieurs ordres de grandeur grâce à la dépendance quadratique de la fréquence porteuse. Elle identifie cinq régions opérationnelles distinctes de l'estimateur du maximum de vraisemblance, étendant les trois régions précédemment rapportées dans la littérature. Les effets du Doppler, de la fréquence porteuse et des variations de fréquence d'échantillonnage sur la performance d'estimation sont systématiquement caractérisés. Troisièmement, le cadre aborde des scénarios réalistes où les mesures de phase contiennent une incertitude quantifiable. Un estimateur optimal statistiquement conscient de la phase est développé par maximisation rigoureuse de la vraisemblance. De nouveaux résultats montrent des transitions de performance entre les bornes conventionnelles et optimales basées sur la qualité d'observation de phase. Ceux-ci sont comparés aux méthodes conventionnelles ainsi qu'à une implémentation naïve d'ingénierie qui applique directement les mesures de phase sans pondération statistique. L'analyse révèle que sous incertitude de phase, les implémentations conscientes de la phase et naïves convergent vers un plateau à un niveau d'erreur déterminé par l'incertitude. Chaque augmentation de 10 décibels dans l'incertitude de phase élève les niveaux de plateau d'environ 10 décibels, démontrant une correspondance 1:1 entre la qualité de calibration et les limites fondamentales de performance. L'implémentation naïve reste à ce niveau d'erreur pour toute valeur SNR. En revanche, l'implémentation consciente de la phase reste attachée à la borne plus longtemps, atteignant même des niveaux d'erreur plus bas pour un court intervalle de SNR, avant de finalement se détacher pour former un second plateau à très haut SNR. Les simulations de Monte Carlo utilisant les séquences GPS L1 C/A et Kasami valident les prédictions théoriques. Elles établissent des relations quantitatives entre les exigences de calibration et la précision atteignable. Les résultats démontrent que l'exploitation de la phase porteuse peut théoriquement satisfaire les exigences de la mission NOIRE, bien que l'implémentation pratique nécessite des rapports signal sur bruit supérieurs à 40 dB pour les configurations testées. Cette analyse fournit des informations essentielles pour la planification de mission et permet l'exploration de configurations alternatives. Elle établit des compromis fondamentaux entre la qualité de calibration, la complexité computationnelle et la performance du système.

Mots clés : Borne de Cramér-Rao, estimation du retard temporel et de l'effet Doppler, signaux à bande limitée, estimateur du maximum de vraisemblance.

Acronyms

AF	Ambiguity Function
AWGN	Additive White Gaussian Noise
BLUE	Best Linear Unbiased Estimator
CNES	Centre National d'Études Spatiales
CRB	Cramér-Rao Bound
CSM	Conditional Signal Model
DTOA	Difference in Time-of-Arrival
EDM	Euclidian Distance Matrices
FIM	Fisher Information Matrix
GNSS	Global Navigation Satellite Systems
MAP	Maximum A Posteriori
MDS	Multidimensional Scaling
MLE	Maximum-Likelihood Estimator
MP	Most Powerful
MSE	Mean-Squared Error
MVU	Minimum Variance Unbiased
NOIRE	Nanosatellites pour un Observatoire Interférométrie Radio dans l'Espace
PDF	Probability Density Function
PVT	Position, Velocity and Time
PRN	Pseudo-Random Noise Code
PPP	Precise Point Positioning
RTK	Real-Time Kinematic
RADAR	Radio Detection and Ranging
RMSE	Root-Mean-Squared Error
SBF	Slepian Bangs Formula

SNR	Signal-to-Noise Ratio
SONAR	Sound Navigation and Ranging
TDE	Time-Delay Estimation
WSS	Wide-Sense Stationary

Chapter 1

Introduction

1.1 Thesis Motivation

The Nanosatellites pour un Observatoire Interférométrie Radio dans l'Espace (NOIRE) project is a Centre National d'Études Spatiales (CNES) initiative to deploy a swarm of nanosatellites in lunar orbit for radio astronomy applications. This mission represents a shift from monolithic spacecraft to distributed satellite formations that work collaboratively to achieve scientific objectives while avoiding major drawbacks of traditional sophisticated individual satellites: high spacing costs and higher risk of mission failure upon single instrument malfunction. The NOIRE project tackles these traditional drawbacks and aims to create synthetic apertures of unprecedented size, enabling the resolution of cosmic radio sources with detail previously unattainable. This distributed approach transforms a swarm of small satellites into a powerful scientific instrument for radio astronomy observations.

As illustrated in Figure 1.1, the swarm is designed to operate in lunar orbit, positioned on the far side of the Moon during observation periods. This location provides natural shielding from Earth's electromagnetic interference and solar radiation, creating optimal conditions for sensitive radio astronomy measurements. The Moon acts as both a radiation shield and a stable gravitational anchor for the distributed interferometric array. However, this environment presents operational challenges for maintaining precise formation flying and inter-satellite coordination without the infrastructure support available in Earth orbit. One of the fundamental challenges in this collaborative satellite architecture is determining precise relative positions between satellites. When satellites work together to form a distributed telescope, the accuracy of their relative positions directly determines the quality of the synthesized observations from individual measurements. The mission requires centimeter-level precision in inter-satellite ranging. While such performance is achievable using optical directional links, the mission also requires maximum connectivity within the swarm. Consequently, RF omnidirectional links are the preferred approach, as they enable simultaneous ranging between all satellite pairs without pointing constraints. The centimeter-level accuracy then becomes a significant challenge for RF inter-satellite links, as conventional methods that rely solely on baseband signal correlation achieve precision limited by the modulation frequency rather than exploiting the much higher carrier frequency, motivating the investigation of carrier-phase enhanced techniques that can bridge the gap between conventional RF ranging capabilities and mission requirements.

This gap between mission requirements and existing capabilities motivates this thesis: developing the theoretical framework and methodologies necessary to achieve the ranging precision required for the NOIRE mission's scientific objectives, as well as establishing the requirements

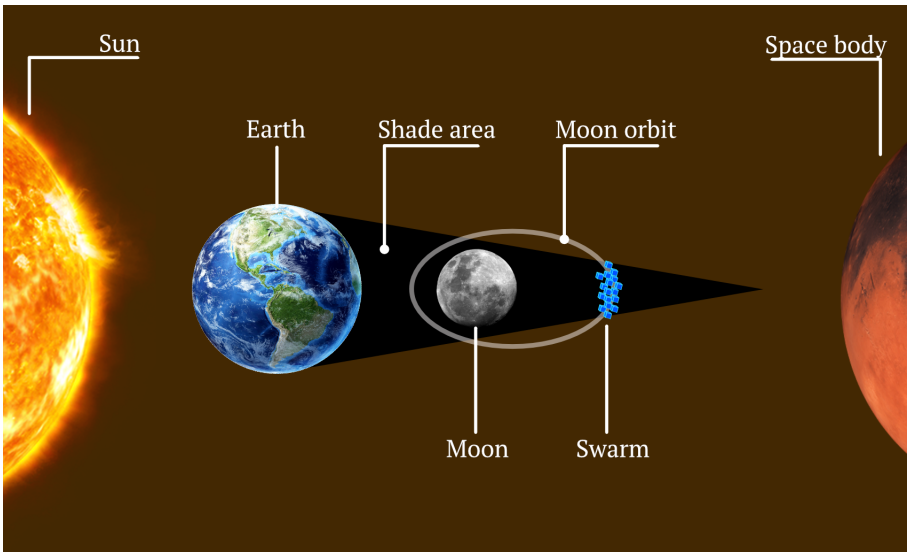

Figure 1.1: NOIRE mission concept showing the satellite swarm positioned in lunar orbit on the far side of the Moon during observation periods.

to attain such precision. This research addresses signal processing theory that will support developments in space system engineering. The work aims to bridge the gap between theoretical possibilities and practical implementation in deep space environments. The developments apply not only to the NOIRE project but also contribute to precision satellite navigation and formation flying, with potential applications to future distributed space missions requiring high-accuracy relative positioning.

1.2 Thesis Objectives

This thesis tackles the fundamental challenge of analyzing time-delay estimation using carrier-phase information, enabling subsequent NOIRE mission design stages to achieve high accuracy inter-satellite ranging. The primary objectives include:

1. Developing a comprehensive signal model that explicitly incorporates observables to compensate to different degrees carrier-phase nuisance parameters, while accounting for common error sources, including Doppler effects and signal propagation offsets.

2. Deriving theoretical performance bounds for carrier-phase based ranging systems, specifically the Cramér-Rao Bound (CRB), to establish fundamental limits on achievable estimation accuracy under various Signal-to-Noise Ratio (SNR) conditions and system configurations.

3. Designing and analyzing Maximum-Likelihood Estimators (MLEs) that exploit both carrier-phase and code-phase information, investigating their convergence properties and operational regions across different SNR regimes.

4. Characterizing the transition between code-dominated and carrier-phase dominated estimation regions, identifying the conditions under which carrier-phase measurements provide performance improvements over traditional methods.

5. Validating theoretical developments through simulations using representative signal structures and relevant scenarios, establishing practical guidelines for system design and imple-

mentation.

1.3 Thesis Outline

The manuscript is organized to progressively develop the theoretical framework for carrier-phase enhanced time-delay estimation, beginning with fundamental signal processing concepts and culminating in comprehensive performance analysis under various phase compensation scenarios.

Chapter 2 establishes the fundamental signal processing tools and concepts necessary for parameter estimation in noisy environments. The chapter introduces the Conditional Signal Model (CSM) framework that underpins deterministic parameter estimation, develops the MLE as the optimal estimation algorithm, and derives the CRB as the fundamental performance limit. The theoretical tools are then applied to ranging applications, demonstrating how time-delay estimation translates to distance measurements and establishing the stringent accuracy requirements for inter-satellite ranging in the NOIRE mission context.

Chapter 3 develops the estimation framework for signal transmission scenarios, extending the general CSM to explicitly decompose the carrier-phase term into hardware-induced and propagation-induced components. The chapter establishes parameter identifiability conditions through rigorous mathematical analysis, demonstrating that phase components previously considered unidentifiable can indeed be uniquely determined under appropriate signal structure conditions. Conventional Time-Delay Estimation (TDE) approaches are presented as the baseline performance reference, where phase information is absorbed into complex amplitude parameters. The chapter revisits established closed-form CRB expressions and MLE formulations from the state of the art for joint delay-doppler estimation, presenting results previously established in prior work while validating the framework through Monte Carlo simulations using both conventional GPS L1 C/A signals and alternative Kasami sequence configurations proposed in the literature.

Chapter 4 investigates the theoretical performance limit achievable under perfect phase compensation, where hardware-induced phase offsets are completely eliminated through ideal calibration. This analysis establishes the tightest possible estimation bounds by removing hardware phase from the parameter space, enabling exploitation of the carrier phase terms associated with time delay and Doppler. The chapter derives closed-form CRB expressions showing the quadratic dependence on carrier frequency that enables orders-of-magnitude accuracy improvements over conventional approaches. The MLE for this scenario is developed through maximization of the likelihood function under known hardware phase conditions, yielding the optimal estimator structure that achieves the theoretical bounds at high SNR. Detailed Ambiguity Function (AF) analysis characterizes the modulation structure induced by both code correlation and carrier phase variations due to delay and Doppler parameters, establishing the mathematical relationship between signal properties and time-delay estimation accuracy. The analysis identifies five distinct operational regions based on SNR levels, extending the previously known three-region model by revealing additional transitional behaviors between code-dominated and carrier-enhanced performance. These operational regions provide quantitative thresholds for system design, establishing when carrier-phase enhanced time-delay estimation justifies implementation complexity and determining the SNR requirements for achieving mission-specified accuracy.

Chapter 5 extends the framework to address practical scenarios where phase measurements contain quantifiable uncertainty characterized by variance in the hardware-phase observables. The chapter develops the statistically optimal phase-aware estimator that properly accounts for phase observation uncertainty through rigorous likelihood maximization, while also presenting the naive compensation approach as a straightforward engineering implementation that directly applies observed phase values without statistical weighting. Novel CRB expressions are derived for the

phase-aware approach, revealing an intermediate plateau whose Mean-Squared Error (MSE) level depends directly on the hardware-phase compensation uncertainty, positioned between the conventional bounds from Chapter 3 and the perfect compensation limits from Chapter 4. The analysis demonstrates distinct estimator behaviors: the naive estimator converges to the CRB plateau and remains bounded at this level regardless of SNR increases, while the phase-aware estimator exhibits richer dynamics: Initially converging to the same plateau, then departing at sufficient SNR to approach the conventional bound towards lower MSE levels, before ultimately detaching to form a second plateau when CSM conditions are not met at high SNR. Comprehensive simulation results establish the relationship between calibration accuracy requirements and achievable time-delay estimation performance, providing quantitative guidelines for system design decisions.

Chapter 6 presents the conclusions of this thesis and outlines future research directions. The chapter synthesizes the theoretical contributions across the phase compensation scenarios, demonstrating how carrier-phase exploitation can achieve the centimeter-level ranging accuracy required for the NOIRE mission while revealing fundamental trade-offs between calibration quality, SNR requirements, and computational complexity. Future research directions include comparison with established methods in the navigation literature, extension to dynamic scenarios with time-varying parameters, robustness analysis under model misspecification, and adaptation of the framework to circular phase distributions when uncertainty becomes large. These directions provide pathways for translating the theoretical contributions into practical ranging implementations for the NOIRE mission and related distributed space applications.

1.4 Thesis Contributions

This research provides several novel contributions to the field of TDE:

1. Phase identifiability analysis demonstrating that the hardware-induced phase term can be uniquely determined from observations under the CSM, contrary to conventional assumptions. This finding, established in Chapter 3, enables justified compensation of hardware-induced carrier-phase terms to exploit propagation-related phase information.

2. Analysis of optimal equipment-related phase compensation in TDE, establishing the theoretical performance limit achievable with perfect phase knowledge. This benchmark, developed in Chapter 4, determines whether phase-enhanced techniques can meet system requirements, providing quantitative guidance for technology adoption decisions.

3. Detailed AF analysis establishing the mathematical relationship between signal correlation properties and estimation accuracy in the presence of phase observables. This analysis, presented in Chapter 4, quantifies the performance improvements achievable through carrier-phase exploitation.

4. Comprehensive characterization of MLE operational regions for carrier-phase enhanced TDE, identifying five distinct behavioral regimes based on SNR and phase uncertainty levels. This analysis, conducted in Chapter 4, extends prior research that recognized only three regions, revealing additional transitional behaviors and establishing threshold conditions for regime transitions.

5. Development of the phase-aware estimation framework, e.g. CRB and MLE, that incorporates phase observation uncertainty, moving beyond binary treatment of phase as either perfectly known or completely unknown. This framework, presented in Chapter 5, bridges the gap between theoretical limits and practical implementations.

6. Identification of operational regimes and SNR thresholds where phase-aware techniques provide practical advantages, determining when sophisticated processing justifies its computational complexity over naive approaches. These guidelines, established in Chapter 5, support system design decisions for practical implementations.

7. Validating theoretical developments through simulations using representative signal structures and relevant scenarios, establishing practical guidelines for system design and implementation throughout Chapters 4, and 5.

1.5 Publications

1.5.1 International Conference Papers

Accepted and presented

- Bernabeu, J.M., Ortega, L., Blais, A., Grégoire, Y., Chaumette, E. "Time-delay and Doppler estimation with a carrier modulated by a band-limited signal." IEEE 9th International Workshop on Computational Advances in Multi-Sensor Adaptive Processing (CAMSAP), 2023.

- Bernabeu, J.M., Ortega, L., Blais, A., Grégoire, Y., Chaumette, E. "On Time-Delay Estimation Accuracy Limit Under Phase Uncertainty." 27th International Conference on Information Fusion (FUSION), pp. 1-6, 2024.

- Bernabeu, J.M., Ortega, L., Blais, A., Grégoire, Y., Chaumette, E. "Delay estimation with a carrier modulated by a band-limited signal." 32nd European Signal Processing Conference (EUSIPCO), 2024.

- Bernabeu, J.M., Ortega, L., Blais, A., Grégoire, Y., Chaumette, E. "Time-Delay Maximum-Likelihood Estimator under Phase Uncertainty." IEEE 10th International Workshop on Computational Advances in Multi-Sensor Adaptive Processing (CAMSAP), 2025.

1.5.2 Journal Publications

Published

- Bernabeu, J.M., Ortega, L., Blais, A., Grégoire, Y., Chaumette, E. "On the asymptotic performance of time-delay and Doppler estimation with a carrier modulated by a band-limited signal." EURASIP Journal on Advances in Signal Processing, vol. 2024, no. 47, 2024. https://doi.org/10.1186/s13634-024-01134-2
  Supporting open-source code: https://github.com/jbernabeu26/MLE-and-CRB-Source-Code.git

Under Submission

- Bernabeu, J.M., Ortega, L., Blais, A., Grégoire, Y., Chaumette, E. "Revisiting the conditional signal model: Application to time-delay estimation."

Under Preparation

- Bernabeu, J.M., Calatrava, H., Closas, P. "Revisiting recursive classification of satellite imaging time-series for Land-Cover Mapping."

1.6 Collaborations

1.6.1 Collaboration with Pau Closas at Northeastern University, Boston, USA

The expertise in estimation theory and statistics I developed during my thesis research created an opportunity to expand my research horizons through collaboration with Professor Pau Closas at Northeastern University. While this work focused on a different area from my main thesis topic, it proved highly complementary to my overall research development.

Our collaboration centered on deriving and testing an online recursive Bayesian estimation method for pixel-class label estimation in image processing. This project provided valuable opportunities to explore new research territory, conduct comprehensive literature reviews in Bayesian statistics, and expand my technical toolkit; skills that have enhanced my approach to my primary thesis work. This research collaboration yielded several significant outcomes: (i) Theoretical advancement: I gained substantial expertise in recursive Bayesian estimation, complementing the deterministic estimation methods central to my main thesis. This dual perspective has enriched my analytical approach to estimation problems. (ii) Expanded technical knowledge: Beyond recursive Bayesian estimation, I became proficient in fundamental academic concepts including linear basis modeling, kernel methods, kernel-approximation techniques such as Random Fourier Features, and Monte Carlo approximation methods including particle filtering. (iii) Implementation experience: I translated these theoretical concepts into practice by developing a comprehensive codebase. This implementation features a hybrid recursive Bayesian estimation approach that combines, through rigorous probabilistic derivation, a grid-based filter for discrete class label probabilities with a particle filter for modeling class-label transition fields. The system also incorporates likelihood estimation from simulated neural networks. (iv) Ongoing development: We are currently refining this codebase with more sophisticated class-label transition approximation methodologies. Once implementation is complete, the validated results will support the theoretical developments underlying an upcoming journal publication.

This collaboration has not only broadened my research portfolio but also strengthened my ability to bridge theoretical concepts with practical implementation, a skill set that continues to benefit my primary research objectives.

1.6.2 Collaboration with Dr. Daniel Medina at the German Aerospace Center (DLR)

A collaborative relationship has been established with Daniel Medina at DLR to apply the time-delay estimation theoretical framework developed in this thesis to cooperative positioning systems and benchmark it against state-of-the-art methodologies. The collaboration has two primary objectives: first, to investigate the application of carrier-phase enhanced TDE in cooperative positioning scenarios where multiple agents share ranging measurements; second, to compare the performance improvements achieved by the phase-aware estimation framework against both conventional TDE and established high-precision techniques such as Real-Time Kinematic (RTK) and Precise Point Positioning (PPP) (Teunissen 2017), following the work presented in (Medina 2020).

This collaboration was supported by a research grant funding a two-week exchange between the respective centers in Toulouse and Berlin. While unforeseen scheduling conflicts have necessitated multiple extensions of the grant period through the conclusion of this thesis, preventing the exchange from taking place as originally planned, active discussions about the collaboration's objectives and future implementation have been maintained. This partnership remains positioned to provide valuable comparative analysis once scheduling permits.

Chapter 2

Signal Processing Tools and Concepts

2.1 Introduction

The extraction of information from received signals constitutes a fundamental challenge in communication and navigation systems. To address this challenge systematically, signal processing relies on mathematical models that capture the essential characteristics of signal propagation, distortion, and noise. These models enable the development of estimation algorithms that extract parameters of interest, e.g. time-delay, Doppler shift, and carrier-phase, from noisy observations. The quality of these estimators can be assessed through comparison with theoretical performance bounds, which establish the fundamental limits of what is achievable given the available signal energy and noise conditions.

This chapter provides the theoretical basis for the carrier-based ranging techniques developed in this thesis. The signal processing framework is presented within the context of the NOIRE project requirements, where precise inter-satellite ranging is essential for radio interferometry applications. The chapter establishes the mathematical tools necessary for analyzing time-delay estimation performance when exploiting carrier-phase measurements, and demonstrates their application to ranging systems with particular emphasis on Global Navigation Satellite Systems (GNSS)-like architectures.

The chapter is structured to build from fundamental statistical concepts to specialized estimation frameworks. Section 2.2 reviews the essential concepts of random variables, random processes, and their role in parameter estimation. Section 2.3 introduces the CSM that forms the basis for deterministic parameter estimation in noisy environments. Section 2.4 establishes metrics for evaluating estimator performance, including bias, variance, and MSE. Sections 2.4.3 and 2.4.2 develop the MLE and CRB, providing both practical estimation algorithms and theoretical performance limits. Sections 2.5 and 2.6 apply these tools to carrier-based ranging problems relevant to the NOIRE mission.

2.2 Background on Deterministic Parameter Estimation

Parameter estimation concerns the extraction of unknown deterministic quantities from observations corrupted by random disturbances. The framework distinguishes between deterministic

parameters, fixed but unknown quantities, and random variables that model uncertainty and noise processes.

A random variable X represents a mapping from a sample space to real or complex values, characterized by its Probability Density Function (PDF). For continuous random variables, the statistical behavior is fully described by the probability density function $p_X(x)$. The observed signal samples depend on a set of parameters, which can be either known or unknown. The unknown parameters may originate from various sources including media propagation effects, hardware inefficiencies, or imperfections, and may represent physical quantities such as acceleration, time delay, etc. These parameters of interest are grouped into a vector of unknowns denoted by $\boldsymbol{\theta}$. The dependence of the signal on these parameters is explicitly expressed through its PDF, denoted by $P(\mathbf{x};\boldsymbol{\theta})$, where $\mathbf{x} = [x(1), \ldots, x(N)]$ contains N realizations of X.

Deterministic parameter estimation begins with representing the received signal through a mathematical model with an associated PDF, where unknown parameters are treated as fixed but unknown values rather than random variables with prior distributions. This assumption applies naturally to physical phenomena such as time-delay and Doppler shift, which remain constant over sufficiently short observation intervals. The choice of deterministic estimation over Bayesian methods is motivated by its analytical tractability for TDE problems: when combined with the Gaussian noise assumption in the CSM framework, this approach enables derivation of explicit expressions for estimators and performance bounds, providing direct insight into the relationship between system parameters and achievable accuracy. In contrast, Bayesian methods would require specification of prior distributions, that often result in intractable integral problems that must be solved through numerical approximation methods, obscuring fundamental system relationships. Moreover, the incorporation of prior information introduces the risk of model misspecification, where incorrect priors can degrade estimator performance below that of deterministic methods. This issue becomes particularly problematic when reliable prior knowledge is unavailable or when system parameters vary across different operational conditions.

2.3 Conditional Signal Model

The Conditional Signal Model (CSM) (Van Trees 2002, §8.4.4) (Stoica 1990) provides the mathematical framework for describing deterministic signals embedded in stochastic noise, where the deterministic component is characterized by a set of unknown parameters. The general vector formulation of the CSM for multiple sources is expressed as,

$$\mathbf{x} = \mathbf{B}(\boldsymbol{\theta})\boldsymbol{\alpha} + \mathbf{n}, \tag{2.1}$$

where $\mathbf{x} \in \mathbb{C}^N$ represents the N-dimensional observation vector, $\mathbf{B}(\boldsymbol{\theta}) = [\mathbf{b}(\boldsymbol{\theta}_1), \ldots, \mathbf{b}(\boldsymbol{\theta}_L)] \in \mathbb{C}^{N\times L}$ denotes the matrix of known signal structures with each column parameterized by the unknown deterministic parameter vector $\boldsymbol{\theta}_\ell$ with $\ell = 1, \ldots, L$, $\boldsymbol{\alpha} = (\alpha_1, \ldots, \alpha_L)^{\mathrm{T}} \in \mathbb{C}^L$ constitutes the vector of signal amplitudes, and $\mathbf{n} \in \mathbb{C}^N$ represents additive noise.

Throughout this manuscript, the single-source case where $L = 1$ is considered, for which the model reduces to,

$$\mathbf{x} = \alpha\mathbf{b}(\boldsymbol{\theta}) + \mathbf{n}, \tag{2.2}$$

where $\mathbf{b}(\boldsymbol{\theta}) \in \mathbb{C}^N$ denotes the known signal structure parameterized by the unknown deterministic parameter vector $\boldsymbol{\theta}$, and $\alpha \in \mathbb{C}$ constitutes the signal amplitude. The noise term $\mathbf{n}$ is commonly modeled as a circularly-symmetric centered complex Gaussian random vector

$$\mathbf{n} \sim \mathcal{CN}(\mathbf{0}, \sigma_n^2\mathbf{I}_N), \tag{2.3}$$

where σ_n^2 denotes the noise variance and $\mathbf{I}_N$ is the $N \times N$ identity matrix. For real-valued signals, the corresponding distribution becomes $\mathbf{n} \sim \mathcal{N}(\mathbf{0}, \sigma_n^2 \mathbf{I}_N)$. While this Gaussian assumption simplifies analysis and often reflects physical noise processes, the framework extends to more general noise distributions when required by specific applications (Ollila 2012).

The CSM exhibits broad applicability across diverse signal processing domains due to its generality, with the specific structure of $\mathbf{b}(\boldsymbol{\theta})$ adapted to particular use cases. In Radio Detection and Ranging (RADAR) and Sound Navigation and Ranging (SONAR) applications, $\boldsymbol{\theta}$ typically encompasses time-delay and Doppler parameters (Mengali 2013). For communication systems, it may include carrier frequency offset, symbol timing, and channel parameters. In navigation applications relevant to this thesis, the parameter vector contains propagation delay and phase terms critical for ranging accuracy.

Under the Gaussian noise assumption, the observation vector $\mathbf{x}$ follows a complex normal distribution

$$\mathbf{x} \sim \mathcal{CN}(\alpha \mathbf{b}(\boldsymbol{\theta}), \sigma_n^2 \mathbf{I}_N) \tag{2.4}$$

with the corresponding probability density function

$$P(\mathbf{x}; \boldsymbol{\theta}, \alpha, \sigma_n^2) = \frac{1}{\pi^N (\sigma_n^2)^N} \exp\left\{ -\frac{1}{\sigma_n^2} \|\mathbf{x} - \alpha \mathbf{b}(\boldsymbol{\theta})\|^2 \right\}. \tag{2.5}$$

This probabilistic characterization enables the derivation of statistical inference tools that extract information about the unknown parameters from the received signal. The likelihood function enables the derivation of the MLE, which identifies parameter values that maximize the probability of observing the received data. On the other hand, the Fisher Information Matrix (FIM) derived from this likelihood establishes the CRB (Kay 1993), providing the theoretical minimum variance achievable by any unbiased estimator. These tools, developed in subsequent sections, quantify both the practical estimation algorithms and fundamental performance limits for parameter extraction under the CSM framework.

2.4 Estimation Quality Assessment

An estimator is a function that maps observed data to an estimate of an unknown parameter. Since the observed data is random, the output of this function, and thus the estimator itself, is also a random variable. Given the signal model in equation (2.2) and its associated observations, the estimator seeks to determine the parameter values that best explain the received signal. The validity of the estimator depends on how well the assumed model represents the actual signal characteristics. For the CSM in equation (2.2), the complete vector of unknown true parameters is denoted by $\boldsymbol{\epsilon} = [\sigma_n^2, \alpha, \boldsymbol{\theta}^{\mathrm{T}}]^{\mathrm{T}}$.

The performance of parameter estimators is characterized through several fundamental metrics that quantify accuracy and precision. Accuracy refers to how close an estimate is to the true parameter value on average, measured through the estimator's bias. Precision quantifies the consistency of estimates across multiple realizations, measured through the estimator's variance. An ideal estimator exhibits both high accuracy (low bias) and high precision (low variance), as defined next:

- The bias of an estimator $\hat{\boldsymbol{\epsilon}}$ measures its systematic deviation from the true parameter value

$$\mathrm{Bias}(\hat{\boldsymbol{\epsilon}}) = \mathrm{E}\{\hat{\boldsymbol{\epsilon}}\} - \boldsymbol{\epsilon}, \tag{2.6}$$

  where $\mathrm{E}\{\cdot\}$ is the expectation operator. An estimator is unbiased if $\mathrm{E}\{\hat{\boldsymbol{\epsilon}}\} = \boldsymbol{\epsilon}$ for all parameter values. While unbiasedness is desirable, biased estimators may achieve lower overall error through variance reduction.

- The variance quantifies the spread of estimates around their expected value. For a scalar estimator, it is defined as,

$$\mathrm{Var}(\hat{\epsilon}) = \mathrm{E}\left\{(\hat{\epsilon} - \mathrm{E}\{\hat{\epsilon}\})^2\right\}. \tag{2.7}$$

  For vector estimators, the covariance matrix captures both individual variances and cross-correlations between parameter estimates

$$\mathbf{Cov}(\hat{\boldsymbol{\epsilon}}) = \mathrm{E}\left\{(\hat{\boldsymbol{\epsilon}} - \mathrm{E}\{\hat{\boldsymbol{\epsilon}}\})(\hat{\boldsymbol{\epsilon}} - \mathrm{E}\{\hat{\boldsymbol{\epsilon}}\})^{\mathrm{T}}\right\}. \tag{2.8}$$

These performance metrics can be derived from the signal model and its associated PDF. For the CSM introduced in Section 2.3, the Gaussian noise assumption enables closed-form expressions for both the estimator statistics and their theoretical bounds. The likelihood function $P(\mathbf{x}; \boldsymbol{\epsilon})$ provides the basis for deriving these metrics, establishing the relationship between observation quality, system parameters, and achievable estimation performance.

The bias and variance of an estimator define the expected estimation error. Such estimation error is often characterized as the MSE.

- The MSE is defined as,

$$\mathrm{MSE}(\hat{\boldsymbol{\epsilon}}) = \mathrm{E}\{(\hat{\boldsymbol{\epsilon}} - \boldsymbol{\epsilon})(\hat{\boldsymbol{\epsilon}} - \boldsymbol{\epsilon})^{\mathrm{T}}\}. \tag{2.9}$$

  It can be related to the bias-variance decomposition as,

$$\mathrm{MSE}(\hat{\boldsymbol{\epsilon}}) = \mathrm{Var}(\hat{\boldsymbol{\epsilon}}) + \mathrm{Bias}(\hat{\boldsymbol{\epsilon}})^{\mathrm{T}}\mathrm{Bias}(\hat{\boldsymbol{\epsilon}}), \tag{2.10}$$

  where $\mathrm{Var}(\hat{\boldsymbol{\epsilon}}) = \mathrm{E}\{(\hat{\boldsymbol{\epsilon}} - \mathrm{E}\{\hat{\boldsymbol{\epsilon}}\})(\hat{\boldsymbol{\epsilon}} - \mathrm{E}\{\hat{\boldsymbol{\epsilon}}\})^{\mathrm{T}}\}$. For unbiased estimators, the bias term vanishes and the MSE equals the variance, justifying the common practice of focusing on variance minimization in estimation problems. A lower bound for $\boldsymbol{\epsilon}$, for instance the CRB, establishes the theoretical minimum variance achievable by any unbiased estimator, providing $\mathrm{Var}(\hat{\boldsymbol{\epsilon}}) \geq \mathrm{CRB}_{\boldsymbol{\epsilon}}$. Therefore, for unbiased estimators, the MSE is fundamentally limited by the CRB, which depends on the Fisher Information contained in the observations.

The relationship between these variance, bias and MSE performance metrics leads to two critical properties of estimators: Efficiency and Consistency.

- Efficiency measures how well an estimator utilizes the available information by comparing its variance to the CRB, which as explained in later sections, defines the minimum variance with which a parameter can be estimated based on the signal model's statistical properties. Let $\hat{\boldsymbol{\epsilon}}_N$ denote an estimator based on N signal samples. An efficient estimator asymptotically achieves the CRB, meaning that $\lim_{N\to\infty} \mathrm{Var}(\hat{\boldsymbol{\epsilon}}_N) = \mathrm{CRB}_{\boldsymbol{\epsilon}}$, indicating optimal performance in the asymptotic regime.

- Consistency, in the mean squared sense, characterizes the asymptotic behavior, requiring that both bias and variance approach zero as the number of observations N increases, ensuring $\mathrm{MSE}(\hat{\boldsymbol{\epsilon}}) \to \mathbf{0}$ as $N \to \infty$. These properties together establish whether an estimator can achieve theoretical performance limits and improve with additional data.

The following sections develop the two fundamental tools for parameter estimation under the CSM framework: the MLE, which provides a systematic method for obtaining parameter estimates from observations, and the CRB, which establishes the theoretical performance limits against which any estimator can be evaluated.

2.4.1 Minimum Variance Unbiased Estimator

For time-delay estimation in ranging systems, finding the Minimum Variance Unbiased (MVU) estimator (Kay 1993, §5) would be of significant interest as it would guarantee optimal ranging accuracy by achieving the lowest possible variance among all unbiased estimators. An MVU estimator for time-delay would directly minimize the ranging error variance $\sigma_D^2 = c^2\sigma_\tau^2$, where σ_D^2 denotes the variance of the distance estimate, c is the speed of light, and σ_τ^2 represents the variance of the time-delay estimate, providing the best possible precision for inter-satellite distance measurements critical to the NOIRE mission. The MVU estimator, when it exists, has the minimum variance among all unbiased estimators. An efficient estimator (one that achieves the CRB) is necessarily the MVU estimator, though the MVU does not always achieve the CRB. The CRB represents a theoretical lower bound that may not always be attainable.

Finding the MVU estimator requires first identifying a sufficient statistic (Kay 1993, §5.4), then applying the Rao-Blackwell-Lehmann-Scheffé theorem to obtain an unbiased estimator based on that sufficient statistic. A sufficient statistic $T(\mathbf{x})$ for $\boldsymbol{\epsilon}$ captures all the information about $\boldsymbol{\epsilon}$ contained in the observations $\mathbf{x}$. Formally, a statistic is sufficient if the conditional distribution $P(\mathbf{x}|T(\mathbf{x}), \boldsymbol{\epsilon})$ does not depend on $\boldsymbol{\epsilon}$. The factorization theorem provides a practical test: $T(\mathbf{x})$ is sufficient if and only if the likelihood can be factored as,

$$P(\mathbf{x}; \boldsymbol{\epsilon}) = g(T(\mathbf{x}), \boldsymbol{\epsilon})h(\mathbf{x}) \tag{2.11}$$

where g is a function that depends on $\mathbf{x}$ only through $T(\mathbf{x})$, and h is a function depending only on $\mathbf{x}$. However, it can occur in practice that the MVU estimator, if it exists, cannot be found. For instance, the PDF of the data may not be known precisely enough to model it accurately. Even when the PDF is known, as in the study conducted in the present manuscript which considers the CSM and Gaussian noise assumption, the MVU approach relies on the theory of sufficient statistics, which is not always applicable. For complex signal models with multiple parameters and nonlinear phase terms, sufficient statistics may not exist in a useful form, or deriving an unbiased estimator from them becomes analytically intractable.

The minimum variance achievable by the MVU estimator can be quantified through lower bounds on the estimator variance. While several such bounds exist in the literature (Kay 1993), this study employs the CRB due to its widespread adoption in TDE studies and its straightforward, well-established derivation procedure. The CRB provides a systematic approach to characterizing fundamental performance limits and will be introduced in the following section.

2.4.2 Cramér-Rao Bound

The CRB establishes the fundamental limit on the variance of any unbiased estimator, providing a benchmark against which practical estimators can be evaluated. For the vector parameter $\boldsymbol{\epsilon}$, the CRB is obtained from the inverse of the FIM (Kay 1993, §3)

$$\mathrm{CRB}_{\boldsymbol{\epsilon}|\boldsymbol{\epsilon}} = \mathbf{F}_{\boldsymbol{\epsilon}|\boldsymbol{\epsilon}}^{-1}, \qquad \mathbf{F}_{\boldsymbol{\epsilon}|\boldsymbol{\epsilon}}^{-1} = -\mathrm{E}\left\{ \frac{\partial^2 \ln P(\mathbf{x}; \boldsymbol{\epsilon})}{\partial \boldsymbol{\epsilon}\, \partial \boldsymbol{\epsilon}^{\mathrm{T}}} \right\}, \tag{2.12}$$

The inequality $\mathrm{Cov}(\hat{\boldsymbol{\epsilon}}) \succeq \mathrm{CRB}_{\boldsymbol{\epsilon}}$ holds for any unbiased estimator $\hat{\boldsymbol{\epsilon}}$, with the matrix inequality understood in the positive semidefinite sense. The MVU estimator, when it exists, attains this bound, making the CRB both a theoretical limit and a benchmark for optimal estimation.

Slepian-Bangs Formula for Gaussian Models

For Gaussian observation models, the FIM can be conveniently obtained through the Slepian Bangs Formula (SBF) (Van Trees 2002). The formula applies to both real and complex Gaussian

distributions, with distinct expressions for each case.

For real-valued observations $\mathbf{x} \sim \mathcal{N}(\mathbf{m}_\mathbf{x}(\boldsymbol{\epsilon}), \mathbf{C}_\mathbf{x}(\boldsymbol{\epsilon}))$, the SBF formula yields

$$[\mathbf{F}(\boldsymbol{\epsilon})]_{k,l} = \frac{\partial \mathbf{m}_\mathbf{x}(\boldsymbol{\epsilon})}{\partial \epsilon_k}^{\mathrm{T}} \mathbf{C}_\mathbf{x}^{-1}(\boldsymbol{\epsilon}) \frac{\partial \mathbf{m}_\mathbf{x}(\boldsymbol{\epsilon})}{\partial \epsilon_l} + \frac{1}{2}\mathrm{tr}\left(\mathbf{C}_\mathbf{x}^{-1}(\boldsymbol{\epsilon}) \frac{\partial \mathbf{C}_\mathbf{x}(\boldsymbol{\epsilon})}{\partial \epsilon_k} \mathbf{C}_\mathbf{x}^{-1}(\boldsymbol{\epsilon}) \frac{\partial \mathbf{C}_\mathbf{x}(\boldsymbol{\epsilon})}{\partial \epsilon_l} \right) \tag{2.13a}$$

where $\mathrm{tr}(\cdot)$ denotes the matrix trace operator.

For complex-valued observations $\mathbf{x} \sim \mathcal{CN}(\mathbf{m}_\mathbf{x}(\boldsymbol{\epsilon}), \mathbf{C}_\mathbf{x}(\boldsymbol{\epsilon}))$, the corresponding formula becomes,

$$[\mathbf{F}(\boldsymbol{\epsilon})]_{k,l} = 2\Re\left\{ \frac{\partial \mathbf{m}_\mathbf{x}(\boldsymbol{\epsilon})}{\partial \epsilon_k}^{\mathrm{H}} \mathbf{C}_\mathbf{x}^{-1}(\boldsymbol{\epsilon}) \frac{\partial \mathbf{m}_\mathbf{x}(\boldsymbol{\epsilon})}{\partial \epsilon_l} \right\} + \mathrm{tr}\left(\mathbf{C}_\mathbf{x}^{-1}(\boldsymbol{\epsilon}) \frac{\partial \mathbf{C}_\mathbf{x}(\boldsymbol{\epsilon})}{\partial \epsilon_k} \mathbf{C}_\mathbf{x}^{-1}(\boldsymbol{\epsilon}) \frac{\partial \mathbf{C}_\mathbf{x}(\boldsymbol{\epsilon})}{\partial \epsilon_l} \right) \tag{2.13b}$$

The key differences from the real-valued case are the factor of 2 in the first term due to the complex nature of the signal, the Hermitian transpose replacing the standard transpose, and the absence of the factor 1/2 in the trace term. These formulas decompose the Fisher information into two contributions: the first term captures information from parameter-dependent mean variations, while the second term accounts for parameter-dependent covariance structure. For the CSM with white Gaussian noise where $\mathbf{C}_\mathbf{x} = \sigma_n^2\mathbf{I}$, the covariance is independent of the signal parameters $\boldsymbol{\eta}$, causing the trace term to vanish for these parameters.

Both equations are interchangeable in the sense that, given a complex signal model, one can rearrange it into an equivalent real-valued formulation by decomposing the complex observations into their real and imaginary components. Specifically, the complex observation vector $\mathbf{x} \in \mathbb{C}^N$ can be represented as a real-valued vector $\underline{\mathbf{x}} = [\Re\{\mathbf{x}\}^\mathrm{T}, \Im\{\mathbf{x}\}^\mathrm{T}]^\mathrm{T} \in \mathbb{R}^{2N}$, allowing the application of (2.13a) instead of (2.13b), as demonstrated in subsequent chapters.

2.4.3 Maximum Likelihood Estimator

The constraints in finding the MVU estimator encourage practical studies to resort to suboptimal estimators. In doing so, the actual performance loss relative to the MVU estimator remains unknown, since the minimum variance of the MVU estimator cannot be determined. However, the variance of a suboptimal estimator can be determined and compared to the CRB, and, if it meets system specifications, its use becomes acceptable for the problem at hand.

For the TDE assessment in this manuscript, the MLE (Kay 1993, §7) presents the most appropriate choice for several reasons. First, the complete statistical characterization of the signal model is known through the CSM with Gaussian noise assumption, enabling full exploitation of the likelihood function. Second, the time-delay estimation problem with carrier-phase observables is inherently nonlinear due to the sinusoidal carrier term, introduced in later chapters as $e^{-j\omega_c\tau}$, , making linear estimators such as Best Linear Unbiased Estimator (BLUE) (Kay 1993, §6) unsuitable as they cannot exploit the fine phase structure that provides the precision improvement. The MLE, unrestricted by linearity constraints, can fully process this nonlinear phase information. Third, for high-SNR scenarios, which could be assumed to some extent for inter-satellite ranging with dedicated signals, the MLE approaches optimal performance by achieving the CRB asymptotically. Fourth, the MLE provides a systematic approach for deriving estimators, facilitating both theoretical analysis and practical implementation even when closed-form solutions are not available.

MLE for the Conditional Signal Model

The MLE is defined as,

$$\hat{\boldsymbol{\epsilon}}_\mathrm{ML} = \arg\max_{\boldsymbol{\epsilon}} P(\mathbf{x}; \boldsymbol{\epsilon}) \tag{2.14}$$

and has the crucial property of asymptotic efficiency: as the number of observations or SNR increases, the MLE variance approaches the CRB (Kay 1993, §7.5).

For the CSM with Gaussian noise from equation (2.2), the likelihood function is,

$$P(\mathbf{x};\boldsymbol{\epsilon}) = \frac{1}{(\pi\sigma_n^2)^N}\exp\left\{-\frac{1}{\sigma_n^2}\|\mathbf{x}-\alpha\mathbf{b}(\boldsymbol{\theta})\|^2\right\}. \tag{2.15}$$

The MLE seeks the parameter vector $\boldsymbol{\epsilon}$ that maximizes this likelihood or equivalently the log-likelihood to eliminate the exponential term

$$\hat{\boldsymbol{\epsilon}} = \arg\max_{\boldsymbol{\epsilon}}\{\ln P(\mathbf{x};\boldsymbol{\epsilon})\} = \arg\max_{\boldsymbol{\epsilon}}\left\{-N\ln(\pi) - N\ln(\sigma_n^2) - \frac{1}{\sigma_n^2}\|\mathbf{x}-\alpha\mathbf{b}(\boldsymbol{\theta})\|^2\right\}. \tag{2.16}$$

The noise variance estimator $\hat{\sigma}_n^2$ is obtained by setting the partial derivative of the log-likelihood to zero

$$\frac{\partial \ln P(\mathbf{x};\boldsymbol{\epsilon})}{\partial\sigma_n^2} = -\frac{N}{\sigma_n^2} + \frac{\|\mathbf{x}-\alpha\mathbf{b}(\boldsymbol{\theta})\|^2}{(\sigma_n^2)^2} = 0, \tag{2.17}$$

yielding the maximum likelihood estimate of the noise variance

$$\hat{\sigma}_n^2 = \frac{1}{N}\|\mathbf{x}-\alpha\mathbf{b}(\boldsymbol{\theta})\|^2. \tag{2.18}$$

Substituting this estimate into the log-likelihood and omitting constant terms, the MLE problem reduces to

$$(\hat{\boldsymbol{\theta}},\hat{\alpha}) = \arg\max_{\boldsymbol{\theta},\alpha}\left\{-\ln(\|\mathbf{x}-\alpha\mathbf{b}(\boldsymbol{\theta})\|^2)\right\} = \arg\min_{\boldsymbol{\theta},\alpha}\|\mathbf{x}-\alpha\mathbf{b}(\boldsymbol{\theta})\|^2. \tag{2.19}$$

Let $\boldsymbol{\Pi}_{\mathbf{b}} = \mathbf{b}(\boldsymbol{\theta})(\mathbf{b}(\boldsymbol{\theta})^{\mathrm{H}}\mathbf{b}(\boldsymbol{\theta}))^{-1}\mathbf{b}(\boldsymbol{\theta})^{\mathrm{H}}$ denote the orthogonal projector onto the vector space spanned by $\mathbf{b}(\boldsymbol{\theta})$, also referred to as the data space. Then $\boldsymbol{\Pi}_{\mathbf{b}}^{\perp} = \mathbf{I} - \boldsymbol{\Pi}_{\mathbf{b}}$ is the orthogonal projector onto the noise space, and the norm to be minimized can be decomposed as,

$$\|\mathbf{x}-\alpha\mathbf{b}(\boldsymbol{\theta})\|^2 = \|(\boldsymbol{\Pi}_{\mathbf{b}}+\boldsymbol{\Pi}_{\mathbf{b}}^{\perp})(\mathbf{x}-\alpha\mathbf{b}(\boldsymbol{\theta}))\|^2 = \|\boldsymbol{\Pi}_{\mathbf{b}}(\mathbf{x}-\alpha\mathbf{b}(\boldsymbol{\theta}))\|^2 + \|\boldsymbol{\Pi}_{\mathbf{b}}^{\perp}\mathbf{x}\|^2. \tag{2.20}$$

Using the definition of the projectors

$$\|\mathbf{x}-\alpha\mathbf{b}(\boldsymbol{\theta})\|^2 = \left\|\mathbf{b}(\boldsymbol{\theta})(\mathbf{b}(\boldsymbol{\theta})^{\mathrm{H}}\mathbf{b}(\boldsymbol{\theta}))^{-1}\mathbf{b}(\boldsymbol{\theta})^{\mathrm{H}}\mathbf{x} - \alpha\mathbf{b}(\boldsymbol{\theta})\right\|^2 + \|\boldsymbol{\Pi}_{\mathbf{b}}^{\perp}\mathbf{x}\|^2. \tag{2.21}$$

The minimization proceeds in two steps. First, minimize with respect to $\boldsymbol{\theta}$ by maximizing the projection term

$$\hat{\boldsymbol{\theta}} = \arg\min_{\boldsymbol{\theta}}\|\boldsymbol{\Pi}_{\mathbf{b}}^{\perp}\mathbf{x}\|^2 = \arg\max_{\boldsymbol{\theta}}\|\boldsymbol{\Pi}_{\mathbf{b}}\mathbf{x}\|^2. \tag{2.22}$$

Once $\hat{\boldsymbol{\theta}}$ is obtained, minimize with respect to α by nulling the first term

$$\hat{\alpha} = (\mathbf{b}(\hat{\boldsymbol{\theta}})^{\mathrm{H}}\mathbf{b}(\hat{\boldsymbol{\theta}}))^{-1}\mathbf{b}(\hat{\boldsymbol{\theta}})^{\mathrm{H}}\mathbf{x} = \frac{\mathbf{b}(\hat{\boldsymbol{\theta}})^{\mathrm{H}}\mathbf{x}}{\|\mathbf{b}(\hat{\boldsymbol{\theta}})\|^2}. \tag{2.23}$$

Substituting the estimate $\hat{\alpha}$ back into the likelihood removes the dependence on α, producing the compressed log-likelihood function

$$\Lambda_c(\boldsymbol{\theta}) = \frac{|\mathbf{b}^{\mathrm{H}}(\boldsymbol{\theta})\mathbf{x}|^2}{\|\mathbf{b}(\boldsymbol{\theta})\|^2}. \tag{2.24}$$

Hence, the maximum-likelihood estimate of the parameter vector is obtained as,

$$\hat{\boldsymbol{\theta}}_{\mathrm{ML}} = \arg\max_{\boldsymbol{\theta}}\Lambda_c(\boldsymbol{\theta}). \tag{2.25}$$

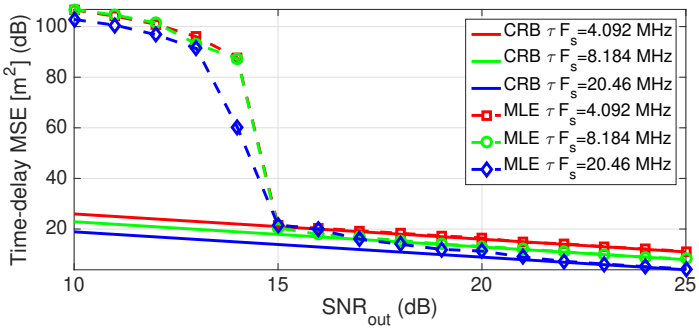

Figure 2.1: Figure from (Das 2020b) illustrating the three operating regions of an MLE of the time-delay for a synthetically generated GPS L1 C/A PRN code.

For carrier-based ranging where the phase term contains delay information, the MLE must account for the carrier-phase contribution. This leads to a modified estimator structure that exploits both the envelope and phase of the received signal, potentially achieving superior performance compared to traditional envelope-based detectors. For most practical problems, closed-form solutions for the MLE do not exist due to the nonlinear dependence of the signal model on the parameters of interest. In such cases, numerical optimization approaches are employed, with grid search methods being a common solution where the likelihood function is evaluated over a discretized parameter space to identify the maximum.

2.4.4 Asymptotic Efficiency and Threshold Effects

As established in (Kay 1993, §7.1), if the PDF of the data $\mathbf{x}$ satisfies some *regularity conditions*, then the MLE of the $\boldsymbol{\theta}$ is asymptotically distributed for large data records. Under this condition, the MLE has been shown to be asymptotically unbiased and to asymptotically attain the CRB, exhibiting asymptotic efficiency, as

$$\lim_{N\to\infty} \text{var}(\hat{\boldsymbol{\theta}}_{\text{MLE}}) = \text{CRB}(\boldsymbol{\theta}), \tag{2.26}$$

where N represents the number of observations. For the CSM, this convergence also occurs as the SNR increases, with the MLE variance approaching the CRB in the high-SNR regime (Renaux 2006). However, at low SNR values, the MLE performance deviates significantly from the CRB. These threshold phenomena establish distinct operational regions, as illustrated in Figure 2.1. This figure presents simulation results for CRB and MLE across various sampling frequency F_s values, using a synthetic GPS L1 C/A PRN code (Dunn 2012). The regions identified are: (i) the a priori region at low SNR values, where the MLE exhibits unreliable behavior with high variance and no convergence properties; (ii) the threshold region where performance transitions rapidly, with estimation accuracy improving dramatically over small SNR increases as the estimator begins to exploit the signal structure; and (iii) the asymptotic region where the MLE achieves the theoretical bound with variance converging to the CRB. The threshold SNR level separating these regions depends critically on the signal bandwidth, observation duration, and as demonstrated in this study, on the presence of carrier-phase information, which introduces additional ambiguities that modify the convergence behavior and shift the operational regime boundaries.

2.5 Ranging with Time-delay Estimates

Range determination (Teunissen 2017, §1.2.2) through time-delay estimation forms the basis of numerous positioning and navigation systems across diverse domains including satellite navigation, RADAR systems, SONAR applications, etc. The measure of the distance between nodes often constitutes the elemental information used in positioning techniques such as Difference in Time-of-Arrival (DTOA) (Kaplan 2006) or Euclidian Distance Matrices (EDM) (Dokmanic 2015). The fundamental relationship between distance and propagation time is,

$$d = c\tau \tag{2.27}$$

where d is the range, c is the speed of light, and τ is the propagation delay. The ranging precision is directly related to the time-delay estimation variance through

$$\sigma_d^2 = c^2\sigma_\tau^2 \tag{2.28}$$

This variance relationship reveals the stringent requirements on time-delay estimation for high-precision ranging. For centimeter-level ranging accuracy, the time-delay must be estimated with sub-nanosecond precision, as an error of 1 nanosecond translates to approximately 30 centimeters in range. The challenge intensifies for millimeter-level accuracy, requiring time-delay precision on the order of picoseconds.

Ranging systems employ different architectures depending on synchronization capabilities and operational constraints. One-way ranging requires synchronized clocks between transmitter and receiver, measuring the time-of-flight directly from transmission to reception. Two-way ranging eliminates clock synchronization requirements by measuring the round-trip propagation time, at the cost of doubled measurement duration and potentially more motion-induced errors. Pseudo-ranging, commonly used in GNSS, measures apparent ranges that include clock biases, requiring multiple measurements to separate geometric range from timing errors.

The achievable ranging precision depends fundamentally on the signal bandwidth and SNR. Wider bandwidth signals provide better ranging accuracy because they produce narrower autocorrelation peaks, enabling finer discrimination of the propagation delay (Van Trees 2001b). This relationship motivates the use of spread-spectrum signals in modern ranging systems, where high-rate pseudorandom codes achieve wide bandwidth while maintaining favorable correlation properties. The spreading codes provide processing gain against noise while the wide bandwidth enables precise delay resolution.

Error sources in ranging systems (Kaplan 2006, §7.2) extend beyond thermal noise to include multipath propagation, clock instabilities, atmospheric delays, and hardware group delays. Multipath creates ambiguities in TDE as reflected signals interfere with the direct path. Clock instabilities manifest as time-varying biases that corrupt range measurements over extended periods. Atmospheric delays introduce range-dependent errors that vary with signal frequency and propagation conditions. Hardware delays in transmit and receive chains introduce systematic biases that affect ranging measurements (Teunissen 2017, §17.6).

2.5.1 Carrier-Phase Measurements in Ranging Systems

Carrier-phase measurements provide superior precision compared to code-phase measurements due to the fundamental relationship between wavelength and ranging resolution, as established by the well-known rule of thumb (Van Sickle 2023), which states that the maximum available resolution in ranges is approximately 1% of the wavelength. This interpretation can also be seen as an indication of ambiguity, especially when atmospheric effects are removed, as they are the

primary sources of error (Teunissen 2017, §1.2.4). For typical navigation and communication signals, carrier wavelengths range from centimeters to decimeters, while code chips can represent meters to hundreds of meters. This significant scale difference, as depicted in Fig. 2.5, directly translates to potential improvements in ranging accuracy.

The pseudorange observation equation (Teunissen 2017, §1.2.5) relates the code-phase measurement to the true range and error sources

$$\rho = D + c(\delta t_r - \delta t_s) + \Delta_{\text{atm}} + \epsilon_\rho \tag{2.29}$$

where D is the geometric range, δt_r and δt_s are receiver and satellite clock offsets, Δ_{atm} represents atmospheric propagation delays including tropospheric and ionospheric effects, and ϵ_ρ is the measurement noise. The carrier-phase observation equation follows a similar structure but incorporates an additional integer ambiguity term

$$\phi = D + c(\delta t_r - \delta t_s) + \Delta_{\text{atm}} + \lambda N + \epsilon_\phi \tag{2.30}$$

where λ is the carrier wavelength, N is the integer ambiguity representing the unknown number of complete carrier cycles between transmitter and receiver, and ϵ_ϕ is phase measurement noise in range-equivalent units. The ionospheric component within Δ_{atm} exhibits opposite-sign dispersion for code and carrier measurements, advancing the carrier phase while delaying the code pseudorange.

Despite the unkown integer ambiguity term λN in carrier-phase measurements, they provide superior accuracy because both the ambiguity scale λ and measurement noise ϵ_ϕ are substantially smaller than their code-phase counterparts, satisfying $\lambda \ll \lambda_{\text{code}}$ and $\epsilon_\phi \ll \epsilon_\rho$. The integer ambiguity represents a constant bias resolvable through sophisticated algorithms, whereas thermal noise fundamentally limits instantaneous precision. For example, for GPS L1/CA signal (Dunn 2012) has $\lambda \approx 19$ cm, while $\lambda_{\text{code}} \approx 293$ m.

2.5.2 Application Example: GNSS Systems

GNSS systems exemplify practical implementation of the time-delay-based ranging principles and measurement equations presented in the previous subsection. Satellites transmit precisely timed signals containing ranging codes and navigation data, enabling receivers to extract both pseudorange and carrier-phase observables from the same transmitted signal structure.

Modern GNSS receivers implement correlation-based processing to generate pseudorange measurements following the code-phase observation equation, while simultaneously tracking carrier loops to produce carrier-phase observables. The pseudorange measurements are related to the unknown receiver position through

$$\rho_i = \|\mathbf{x}_r - \mathbf{x}_i\| + c\delta t_r + \epsilon_i, \quad i = 1, \ldots, M \tag{2.31}$$

where ρ_i denotes the pseudorange to satellite i, $\mathbf{x}_r$ represents the unknown receiver position, $\mathbf{x}_i$ is the known satellite position, δt_r accounts for receiver clock bias, and $M \geq 4$ satellites are required to solve for the three position coordinates plus clock offset. The DTOA positioning problem consists of solving this system of nonlinear equations to determine $\mathbf{x}_r$ and δt_r, typically linearized through iterative least-squares methods around an approximate receiver position. The atmospheric delay term Δ_{atm} decomposes into ionospheric and tropospheric components exhibiting distinct frequency-dependent characteristics, enabling mitigation through dual-frequency observations or atmospheric correction models. This dual-observable architecture exploits the complementary properties of both measurement types: pseudoranges provide unambiguous initialization, while carrier-phase tracking delivers the precision necessary for high-accuracy applications once integer ambiguities are resolved.

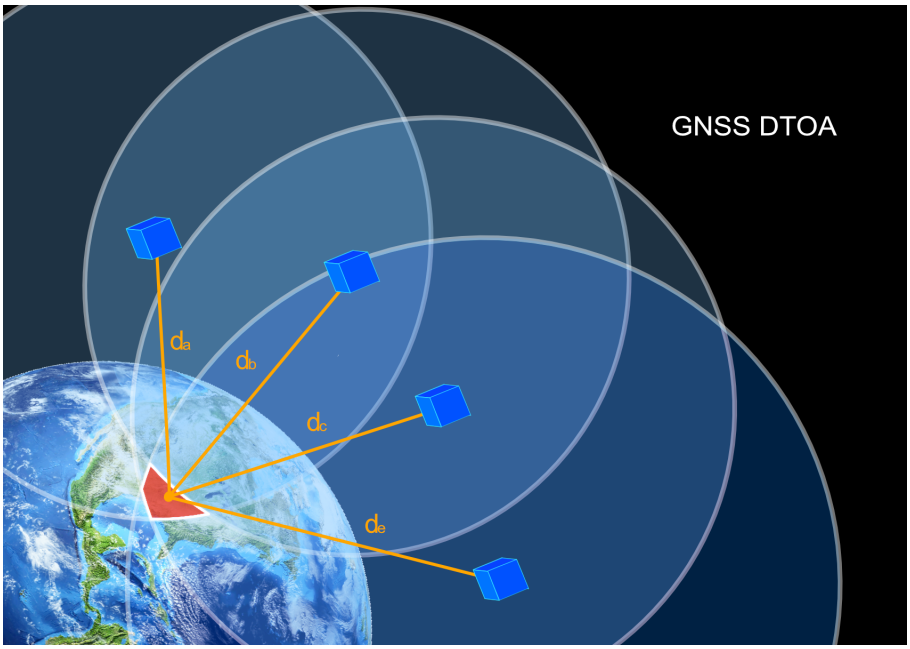

Figure 2.2: DTOA positioning implementation using GNSS satellites. Earth-based receivers perform ranging measurements to multiple GNSS satellites simultaneously, utilizing the measured time-delays to estimate pseudoranges. The receiver position is determined by solving the intersection of spherical surfaces centered at satellite positions with radii equal to the measured pseudoranges. Measurement errors including atmospheric propagation delays, satellite and receiver clock biases introduce uncertainty in the computed position, quantified through metrics such as Dilution of Precision (DOP) that characterize how satellite geometry affects positioning accuracy.

Figure 2.2 illustrates the DTOA positioning implementation where each pseudorange measurement, denoted as "d", defines a spherical surface centered at the satellite position. The receiver location is determined by solving the nonlinear system of equations through iterative methods such as least-squares estimation, with the geometric arrangement of satellites influencing positioning accuracy through the Dilution of Precision effect.

Standard positioning services deliver meter-level accuracy through pseudorange-only processing, while precision applications achieve centimeter-level performance by exploiting carrier-phase measurements following ambiguity resolution. In traditional GNSS processing, carrier-phase information is typically employed in the second step of the positioning solution, during the computation of the Position, Velocity and Time (PVT). However, the approach developed in this thesis differs fundamentally from this conventional two-step process. Rather than using phase information solely for refining the final position estimate, this work exploits carrier-phase knowledge to enhance the time-delay estimation τ itself. The subsequent chapters demonstrate that incorporating phase observables directly into the time-delay estimation framework enables improved accuracy in τ beyond what conventional code-only methods achieve. These enhanced time-delay estimates can then be used with traditional PVT computation methods, providing a more robust basis for the positioning solution. The NOIRE mission's centimeter-level ranging requirements necessitate this carrier-phase exploitation adapted to inter-satellite ranging.

2.6 Link to NOIRE Mission

The NOIRE mission (Cecconi 2018) requires centimeter-level inter-satellite ranging accuracy to maintain the spatial coherence necessary for distributed radio interferometry in lunar orbit. The constellation architecture consists of two types of agents: anchors whose positions are known (up to measurement noise) and tags whose positions must be determined through a set of inter-distance measurements between agents. This distributed system relies on precise ranging between all satellite pairs to establish and maintain the geometric configuration and image reconstruction process required for interferometric observations. Measurement errors directly degrade the quality of the synthesized interferometric image, regardless of individual observation quality, as conceptually illustrated in Figure 2.3. Without precise knowledge of both anchor and tag positions, the individual measurements cannot be properly combined, resulting in reconstruction artifacts and degraded image quality. This requirement motivates the investigation of carrier-phase enhanced time-delay estimation techniques developed throughout this manuscript.

Recent work by Chaumette et al. (Chaumette 2025) established a fundamental limitation for distributed positioning systems: there exists a floor on achievable positioning precision that depends on the variance of inter-agent distance measurements. Specifically, for fixed distance measurement variance σ_d^2, reducing position estimate variance $\sigma_p^2 \to 0$ through improved positioning algorithms cannot eliminate the positioning error floor. This result demonstrates that constellation-level positioning accuracy, as required for the DTOA approach depicted in Figure 2.4, is fundamentally limited by the quality of the ranging measurements between satellite pairs. Such conclusion establishes the importance of minimizing time-delay estimation variance through enhanced measurement techniques. The theoretical tools presented in this chapter provide the framework for assessing time-delay estimation performance in subsequent chapters. The CSM introduced in Section 2.3 characterizes the structure of ranging signals corrupted by noise. The quality assessment metrics developed in Section 2.4 enable quantification of estimator performance through bias, variance, and mean squared error. The MLE derived in Section 2.4.3 provides the estimation algorithm for extracting time-delay information from noisy observations. The CRB established in Section 2.4.2 defines the fundamental variance limits achievable by any unbiased estimator. The quadratic dependence of the Fisher Information on carrier frequency indicates that explicit treatment of carrier-phase contributions could yield performance improvements. For carrier frequencies in the GHz range compared to code rates in the MHz range, as illustrated for GPS L1 C/A signals in Figure 2.5, this frequency ratio could translate to variance reductions of several orders of magnitude, enabling the transition from meter-level code ranging to centimeter-level precision.

These estimation tools are applied in subsequent chapters to analyze carrier-phase enhanced TDE under different phase calibration assumptions. The analysis considers scenarios ranging from perfect phase compensation, where all phase terms are assumed known, to realistic cases where phase uncertainties arise from calibration limitations and hardware imperfections. The resulting performance bounds and estimator behaviors will establish the feasibility of carrier-phase techniques for the NOIRE mission by quantifying the required SNR levels, defining operational regimes where the estimators achieve their theoretical limits, and identifying threshold conditions below which performance degrades. This information directly supports mission design decisions regarding signal power budgets, observation durations, phase calibration requirements, and system architectures necessary to meet the centimeter-level ranging accuracy requirement for the distributed interferometric constellation depicted in Figure 1.1.

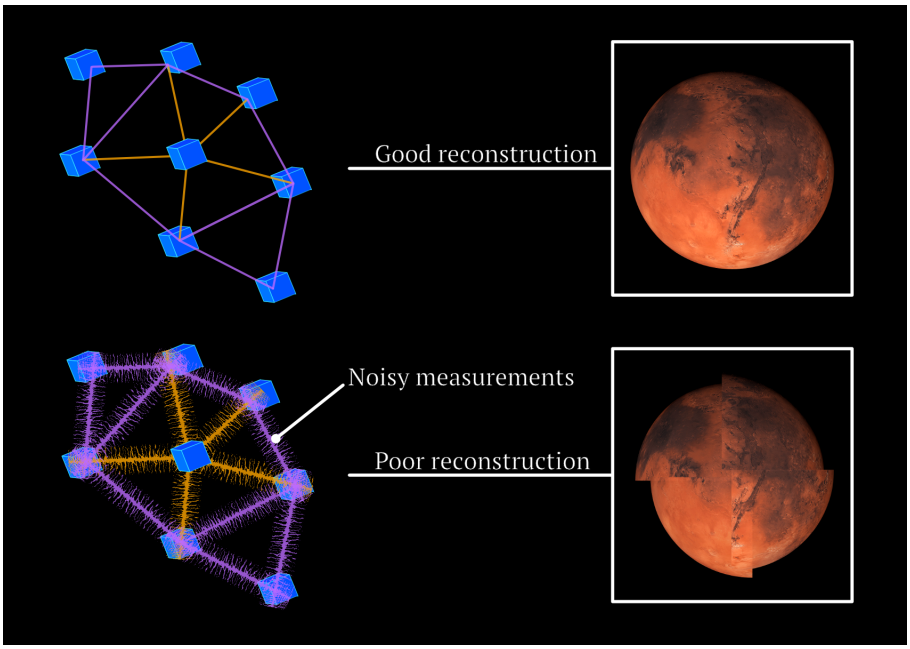

Figure 2.3: Distributed interferometry requires precise spatial arrangement of measurements to avoid reconstruction artifacts. Measurement errors and incertitudes degrade the quality of the distributed image reconstruction, regardless of individual observation quality. Each interferometric baseline provides a spatial frequency component that must be accurately positioned to synthesize the complete observational map without gaps or overlapping information, highlighting the critical importance of inter-satellite ranging accuracy for mission success.

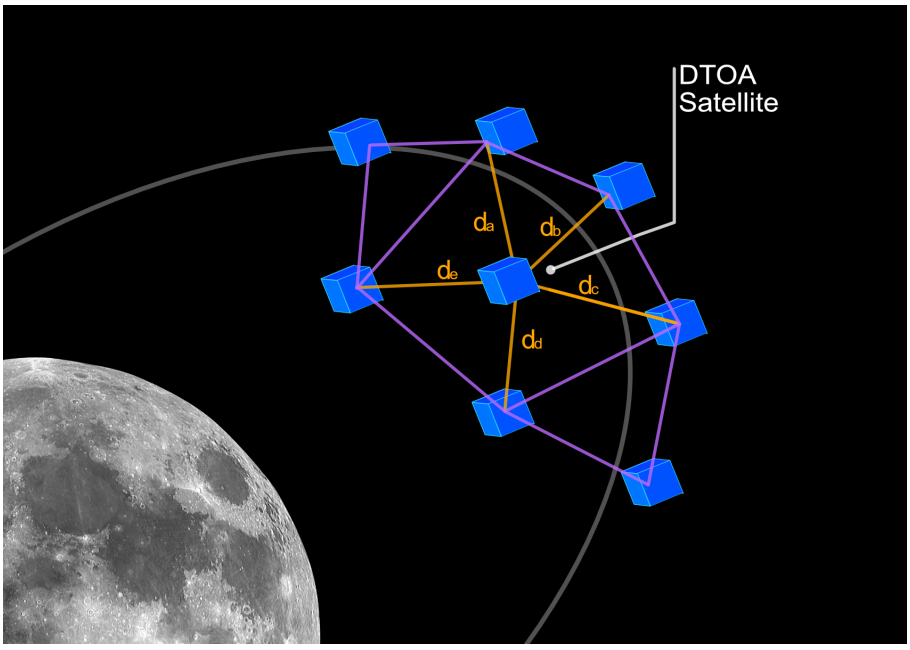

Figure 2.4: Differential Time-of-Arrival (DTOA) positioning principle for satellite constellations, also applicable to swarm formations. For absolute positioning accuracy, the constellation requires knowledge of at least four reference positions to establish the global coordinate frame and prevent solutions that are only relative to the constellation geometry.

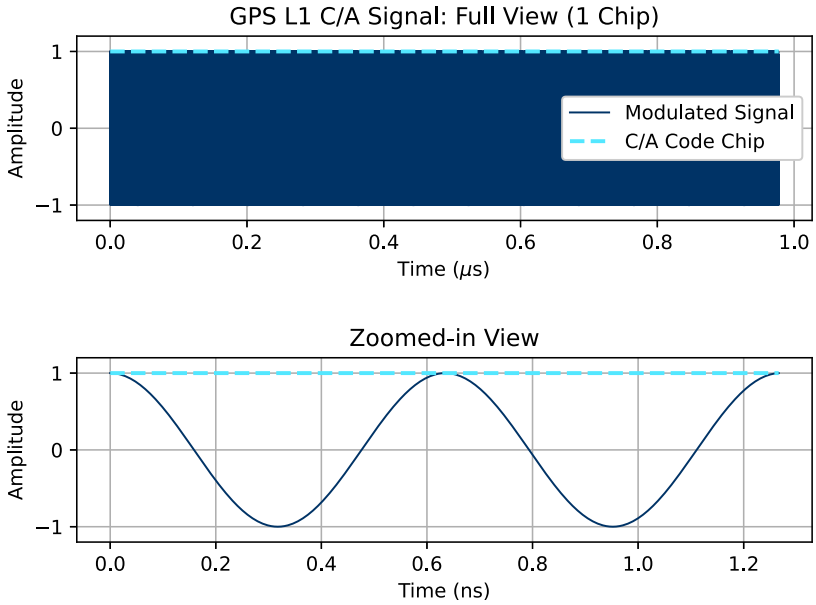

Figure 2.5: GPS L1 C/A signal structure illustrating carrier-phase precision advantage. The upper plot displays a complete GPS L1 C/A code chip modulated by the L1 carrier at 1575.42 MHz over a one-microsecond interval. The lower plot provides a magnified view showing two carrier cycles spanning approximately 1.3 nanoseconds. There are exactly 1540 carrier periods within one L1 C/A code chip, demonstrating the fundamental principle that carrier-phase measurements offer significantly finer temporal resolution than code-phase measurements. The carrier wavelength provides sub-nanosecond ranging precision compared to the microsecond-scale code chip duration, with this factor of 1540 representing the theoretical improvement potential when exploiting carrier-phase information over code-only measurements.

Chapter 3

Time-Delay Estimation

3.1 Introduction

Parameter estimation from noisy observations constitutes a fundamental problem in statistical signal processing, with applications spanning radar, communications, and navigation systems. Chapter 2 introduced the fundamental concepts of deterministic parameter estimation, including the CSM framework, MLE, and CRB as general tools for statistical inference. This chapter builds on that work to establish the formal estimation framework for signal transmission scenarios, presenting the theoretical developments and conventional approaches that constitute the state of the art in TDE.

The CSM framework provides a versatile approach for modeling received signals in wireless communication and radar systems, where propagation phenomena alter signal waveforms as they traverse transmission channels. This chapter extends the general CSM to explicitly model signal transmission effects, decomposing phase terms into hardware-induced and propagation-induced components. Through rigorous identifiability analysis, the conditions under which these phase components can be uniquely determined from observations are established, supporting the subsequent developments in carrier-phase exploitation. Conventional TDE approaches typically absorb phase terms into the signal amplitude to reduce computational complexity, an assumption historically justified by treating hardware-induced phase offsets as unidentifiable nuisance parameters. This chapter presents these conventional methods as the baseline against which enhanced estimation techniques are evaluated. The identifiability analysis reveals that this simplification, while computationally convenient, discards potentially valuable phase information that could enhance ranging accuracy when properly exploited.

The chapter is organized as follows. Section 3.2 establishes fundamental principles of time-delay estimation through correlation-based methods and introduces the AF framework that characterizes estimator behavior and resolution limits throughout this manuscript. Section 3.3 specializes the CSM framework to signal transmission scenarios, introducing the decomposition of phase into hardware-induced and propagation-induced components and establishing the discretization procedure from continuous-time to discrete-time representations. Section 3.4 develops specific signal models for time-delay estimation under various assumptions regarding Doppler effects and signal bandwidth, deriving the propagation-induced phase functions for wideband, narrowband, and delay-only scenarios. Section 3.5 presents conventional TDE approaches where phase information is absorbed into complex amplitude parameters, deriving both the MLE and CRB expressions and validating them through simulations with representative GNSS signals, thereby establishing the baseline performance reference. Section 3.6.1 demonstrates through rigorous identifiability

analysis that phase components can be uniquely determined under appropriate signal structure conditions, contradicting the conventional assumption and laying the theoretical groundwork for the phase compensation strategies developed in Chapters 4 and 5.

3.2 Time-Delay Estimation Principles

This section develops the fundamental principles underlying time-delay estimation. The correlation-based interpretation of maximum likelihood estimation provides intuitive understanding of how delay information is extracted from noisy observations, while the AF framework characterizes the fundamental resolution limits and trade-offs in joint delay-doppler estimation. These principles are extensively used throughout this manuscript to analyze estimator behavior under different signal models and phase compensation scenarios.

Time-delay estimation leverages the correlation between transmitted and received signals to estimate the propagation delay, which allows for the computation of the range in (2.27) before positioning. The correlation-based methods described in this section represent specific implementations of the general MLE framework introduced in Section 2.4.3, where the likelihood function for time-delay parameters reduces to correlation maximization operations. For a signal $c(t)$ transmitted at time $t = 0$ and received as $r(t) = \alpha c(t - \tau) + n(t)$, the cross-correlation function

$$R_{cr}(\tau') = \mathrm{E}\{c^*(t)r(t + \tau')\}, \tag{3.1}$$

exhibits a peak at $\tau' = \tau$, enabling delay estimation through correlation maximization. The precision of this estimate depends on the signal's autocorrelation properties, characterized by its effective bandwidth and duration. For spread-spectrum signals commonly employed in ranging applications, the codes are designed with sharp autocorrelation functions to provide good delay resolution. The main lobe width of the autocorrelation function, approximately inversely proportional to the signal bandwidth, determines the fundamental resolution capability. Gold codes like GPS L1C/A (Dunn 2012) and Kasami sequences (Kasami 1966), commonly used in navigation and communication systems, respectively, provide favorable autocorrelation and cross-correlation properties, essential for multiple-access environments.

The AF $\Xi(\tau, f_d)$, extensively used in this manuscript to justify MLE behaviors, generalizes the noiseless cross-correlation concept to joint delay-doppler estimation

$$\Xi(\tau, f_d) = \int_{-\infty}^{\infty} c(t)c^*(t - \tau)e^{-j2\pi f_d t}dt, \tag{3.2}$$

This function characterizes the signal's ability to discriminate both delay and Doppler simultaneously, revealing fundamental trade-offs in waveform design. The AF's squared magnitude represents the output of a matched filter without the noise contribution, when the actual delay and Doppler differ from the assumed values, quantifying estimation accuracy degradation due to parameter mismatch. Its formulation treats the received signal deterministically and does not consider it as a Wide-Sense Stationary (WSS) process. In practical implementations, the joint delay-doppler search space is discretized into a three-dimensional grid, considering the magnitude of the correlation as the third axis, as illustrated in Figure 3.1, where the estimator evaluates the likelihood function across candidate parameter values to identify the global maximum corresponding to the MLE solution. The MLE for time-delay, derived from the CSM framework, takes the form of a correlation maximization when the signal amplitude is unknown (Kay 1993, §7.15). This estimator converges to the CRB asymptotically, providing optimal performance in high-SNR conditions.

These fundamental principles define the characterization of estimator behavior and support the conceptual framework for time-delay estimation. The following section formalizes the CSM

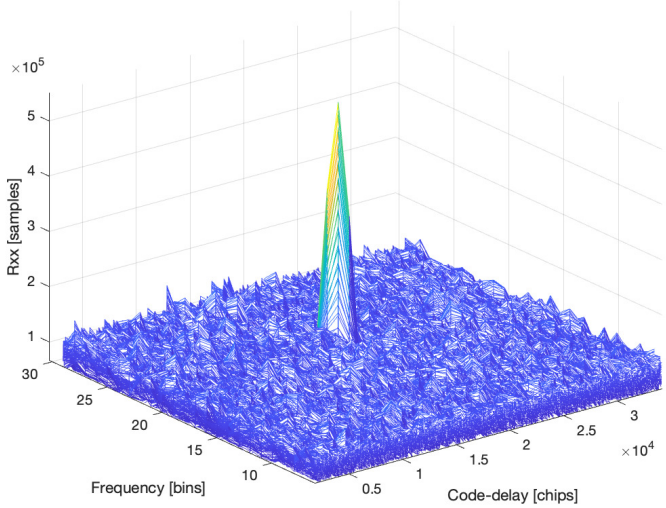

Figure 3.1: Three-dimensional correlation surface for joint delay–Doppler estimation generated using the open-source codebase from (Bernabeu 2022). The surface represents the magnitude of the noisy correlation output (i.e., the ambiguity function combined with measurement noise) across code delay, expressed in subchips. Chips represent the bits of GPS L1 C/A PRNs, and subchips are samples of such chips. In this case, chips were sampled at approximately 34 samples/chip. The Doppler frequency was evaluated in 500 Hz bins over a 7 kHz search window, and a coherent integration time of 20 ms was employed.

for signal transmission scenarios, developing the mathematical framework that enables practical implementation of these correlation principles through explicit signal models and discretization procedures.

3.3 CSM for Signal Transmission

The correlation-based principles and AF framework presented in Section 3.2 form the conceptual framework for TDE. This section extends the single-source CSM framework from Section 2.3 to signal transmission scenarios, developing the mathematical formulation that enables practical implementation of these principles. The CSM is frequently employed to model received signals in communication and detection systems, accounting for various propagation phenomena that alter the signal's waveform as it traverses the transmission channel. These phenomena include, but are not limited to, signal path losses, multipath fading, angle-dependent array responses, and Doppler shifts, which are inherent characteristics of wireless communication channels. The continuous-time baseband representation at the output of the Hilbert filter (Van Trees 2001a) is

$$x(t) = \alpha b(t;\boldsymbol{\theta}) + n(t) = \alpha a(t;\boldsymbol{\eta})e^{j\varphi} + n(t), \quad n(t) \sim \mathcal{CN}(0,\sigma_n^2), \quad \boldsymbol{\theta} = [\varphi, \boldsymbol{\eta}^{\mathrm{T}}]^{\mathrm{T}}, \tag{3.3}$$

where $\alpha \in \mathbb{R}^+$ and φ is a global phase factor primarily accounting for the overall path loss and other non-modeled effects such as transmitter and receiver miscalibration, and the channel-induced perturbations are parameterized by the vector $\boldsymbol{\eta}$.

For practical implementation, the continuous-time formulation requires discretization. By the Nyquist-Shannon theorem (Shannon 2006), a band-limited signal $c(t)$ with bandwidth B sampled

at $f_s \geq B$ can be perfectly reconstructed as,

$$c(t) = \sum_{n=N_1'}^{N_2'} c(nT_s)\text{sinc}(\pi f_s(t - nT_s)). \tag{3.4}$$

In the frequency domain, the discrete-time Fourier transform of the samples yields

$$C(f) = T_s \sum_{n=N_1'}^{N_2'} c(nT_s)e^{-j2\pi f nT_s}, \quad f \in [-B/2, B/2]. \tag{3.5}$$

Extracting $N' = N_2' - N_1' + 1$ samples of (3.4) at sampling frequency f_s yields the discrete vector-form CSM

$$\mathbf{x} = \alpha\mathbf{a}(\boldsymbol{\eta})e^{j\varphi} + \mathbf{n}, \quad \mathbf{x} = \begin{pmatrix} x(N_1'\mathrm{T_s}) \\ \vdots \\ x(N_2'\mathrm{T_s}) \end{pmatrix}, \quad \mathbf{n} = \begin{pmatrix} n(N_1'\mathrm{T_s}) \\ \vdots \\ n(N_2'\mathrm{T_s}) \end{pmatrix}, \tag{3.6}$$

where the discrete steering vector is,

$$\mathbf{a}(\boldsymbol{\eta}) = \begin{pmatrix} a(N_1'\mathrm{T_s};\boldsymbol{\eta}) \\ \vdots \\ a(N_2'\mathrm{T_s};\boldsymbol{\eta}) \end{pmatrix}, \tag{3.7}$$

with $\mathbf{n} \sim \mathcal{CN}(\mathbf{0}, \sigma_n^2\mathbf{I}_{N'})$ and sampling period $\mathrm{T_s} = 1/f_s$.

3.4 CSM for Time-Delay Estimation

Building upon the signal transmission model established in (3.6), this section specializes the framework to time-delay estimation scenarios by explicitly decomposing the phase terms into hardware-induced and propagation-induced components. The parameter vector $\boldsymbol{\eta}$ is specified to contain the time delay τ as the primary parameter of interest, along with auxiliary propagation parameters. The section derives the specific form of the propagation-induced phase function $\psi(\boldsymbol{\eta})$ from the physics of signal propagation with relative motion, then presents three specialized signal models under different bandwidth and motion assumptions: wideband, narrowband, and delay-only cases. These models are employed in the correlation-based time-delay estimation principles developed in Section 3.2 and in the conventional estimation approaches presented in Section 3.5.

3.4.1 General framework with Auxiliary Parameters

In the context of TDE, the received signal after the Hilbert filter is described as (3.6), where the parameter vector $\boldsymbol{\eta}$ is now specified to $\boldsymbol{\eta} = [\tau, \boldsymbol{\omega}^{\mathrm{T}}]^{\mathrm{T}}$, and contains the delay τ as its primary component, with $\boldsymbol{\omega}$ capturing additional propagation phenomena, for instance the Doppler effect.

The CSM in (3.6) introduces a global phase term φ to maintain generality and ensure broad applicability across a wide range of signal transmission scenarios. In this formulation, φ encapsulates hardware-specific distortions, while the propagation-induced phase is implicitly embedded within the complex waveform vector $\mathbf{a}(\boldsymbol{\eta})$, since it is assumed to be parametrized by the same vector of unknowns $\boldsymbol{\eta}$. This representation simplifies the model while allowing for flexibility, but also hinders the distinct physical mechanisms that give rise to phase shifts. To enable finer-grained characterization, this section makes that distinction explicit. The propagation effects are modeled through a complex waveform structure, with

$$\mathbf{x} = \alpha\mathbf{a}(\boldsymbol{\eta})e^{j\varphi} + \mathbf{n} \quad \Leftrightarrow \quad \mathbf{a}(\boldsymbol{\eta}) = \mathbf{c}(\boldsymbol{\eta})e^{j\psi(\boldsymbol{\eta})} \tag{3.8}$$

where $\psi(\boldsymbol{\eta})$ captures propagation-induced phase shifts and $\mathbf{c}(\boldsymbol{\eta})$ denotes the baseband waveform. In this case, the residual phase term φ in (3.6) is interpreted solely as a hardware-induced offset accounting for imperfections such as antenna mismatches, front-end delays, cable phase shifts etc.

3.4.2 Delay-Doppler Case

Having established the general framework for time-delay estimation with auxiliary parameters $\boldsymbol{\omega}$ in the previous section, this section shows the case of the classical RADAR/communication scenario where the Doppler frequency is considered. In this case, $\boldsymbol{\eta} = [\tau, b]^{\mathrm{T}}$ where b representing the time dilation or compression factor caused by relative motion between the transmitter and receiver.

Signal Model Derivation

For the joint delay-doppler problem, this phase function emerges from the physics of signal propagation with relative motion. This section derives the specific form of $\psi(\boldsymbol{\eta})$ for moving targets, from the signal transmission model established in (3.6).

The time-varying range equation for relative motion between satellites, under non-relativistic conditions ($|v| \ll c$), is (Le Chevalier 2002, §1)

$$c \cdot \tau(t) = R(t - \tau(t)), \quad R(t - \tau(t)) = R_0 + \mathbf{v}(t - \tau(t)), \tag{3.9}$$

where $\tau(t)$ is the instantaneous time delay, c is the speed of light, and $R(t - \tau(t))$ represents the instantaneous range between the transmitter located at P_t and the receiver located at P_r. Here, R_0 denotes the initial range at time $t = 0$, and v represents the radial velocity, assumed constant, with $v > 0$ for increasing range (satellites moving apart) and $v < 0$ for decreasing range (satellites approaching). Solving for the time delay $\tau(t)$ yields

$$\tau(t) = \frac{R_0 + vt}{c - v} = \frac{R_0/c}{1 - v/c} + \frac{v/c}{1 - v/c}t. \tag{3.10}$$

Defining the normalized Doppler parameter $b = v/c$, this becomes

$$\tau(t) = \frac{\tau_0}{1 - b} + \frac{b}{1 - b}t, \tag{3.11}$$

where $\tau_0 = R_0/c$ is the initial propagation delay. The parameter b takes values in $(-1, 1)$ for non-relativistic motion, with $b > 0$ indicating increasing delay (negative Doppler shift, satellites receding) and $b < 0$ indicating decreasing delay (positive Doppler shift, satellites approaching). This general formulation accommodates arbitrary relative motion directions within the satellite constellation. Under the assumption $|b| \ll 1$ (valid when $v \ll c$), the Taylor expansion of the term $(1 + b)^{-1}$ yields $(1 + b)^{-1} \approx 1 - b$, which allows to rewrite (3.11) as,

$$\tau(t) \approx \tau_0(1 - b) + bt = \tau_0 + b(t - \tau_0). \tag{3.12}$$

This approximation shows that the time delay consists of a constant term τ_0 plus a time-varying Doppler component. Applying this delay to the baseband signal $c(t)$ (3.8), the received signal becomes $c(t - \tau(t))$. Meanwhile, the carrier phase term adjusts according to the time-varying delay as

$$e^{j\omega_c(t-\tau(t))}e^{-j\omega_c t} \to e^{-j\omega_c\tau(t)} = e^{-j\omega_c(\tau+b(t-\tau))}, \tag{3.13}$$

where the subscript on τ_0 is dropped for notational simplicity. This leads to the reformulation of (3.8) as

$$\mathbf{a}(\boldsymbol{\eta}) = \mathbf{c}(\boldsymbol{\eta})e^{j\psi(\boldsymbol{\eta})}, \quad \psi(\boldsymbol{\eta}) = -\omega_c(\tau + b(n\mathrm{T_s} - \tau)) \tag{3.14}$$

with the parameter vector $\boldsymbol{\eta} = [\tau, b]^{\mathrm{T}}$ containing the time delay τ as the primary parameter and the normalized Doppler shift parameter b.

Incorporating the derived phase function into the extended CSM framework requires distinguishing between wideband and narrowband signal models based on their treatment of Doppler effects. Let B denote the bandwidth of the baseband signal $\mathbf{c}(t)$, and $f_c = \omega_c/(2\pi)$ the carrier frequency. When relative motion induces a Doppler factor $(1 + b)$, the received signal experiences both frequency shifting and time scaling. The impact of time scaling on the baseband signal depends critically on the fractional bandwidth B/f_c. For narrowband signals where $B/f_c \ll 1$, the Doppler-induced bandwidth change ($B \to B + f_c \cdot b$) is negligible compared to the original bandwidth, allowing the time scaling effect on the baseband to be ignored. However, for wideband signals where B/f_c is significant, i.e. $B/f_c > 0.1$, the relative bandwidth change becomes substantial.

Wideband Assumption

Under the wideband assumption where B/f_c is significant, the Doppler effect contracts and dilates the signal's waveform according to the velocity-induced time scaling factor $(1 + b)$, modifying equation (3.14) to:

$$\mathbf{a}(\boldsymbol{\eta}) = \mathbf{c}\left((t - \tau)(1 + b)\right) e^{j\psi(\boldsymbol{\eta})}. \tag{3.15}$$

Narrowband Assumption

Under the narrowband assumption where $B/f_c \ll 1$, the baseband signal remains unaffected by Doppler scaling and only the carrier phase experiences Doppler modulation. Under this representation, equation (3.14) becomes,

$$\mathbf{a}(\boldsymbol{\eta}) = \mathbf{c}(t - \tau)e^{j\psi(\boldsymbol{\eta})}. \tag{3.16}$$

Delay-only Assumption

For scenarios where the relative radial motion is negligible or when computational efficiency is prioritized, the Doppler parameter can be set to zero, $b = 0$. This reduces the parameter vector to $\eta = \tau$ and correspondingly updates the complete parameter set to

$$\boldsymbol{\epsilon} = [\sigma_n^2, \alpha, \boldsymbol{\theta}^T]^T, \quad \boldsymbol{\theta}^T = [\varphi, \eta], \quad \eta = \tau. \tag{3.17}$$

Under this assumption, the signal model (3.14) simplifies to

$$\mathbf{a}(\eta) = \mathbf{c}(t - \tau)e^{j\psi(\eta)}, \quad \psi(\tau) = -\omega_c\tau. \tag{3.18}$$

This simplified model forms the basis for most numerical simulations presented in subsequent chapters.

3.5 Conventional CSM for Time-Delay Estimation

Conventional TDE strategies apply model simplifications to reduce computational complexity by grouping phase terms into the signal amplitude. This approach was historically justified by the assumption that the hardware-induced phase φ and the carrier-phase component $\omega_c\tau$ from the propagation-induced phase $\psi(\boldsymbol{\eta})$ in (3.14) were not independently identifiable, and therefore

both φ and $\omega_c\tau$ were absorbed as nuisance parameters into the complex amplitude. However, as demonstrated in Section 3.6.1, these phase components are indeed identifiable, which motivates exploring alternative compensation strategies.

Conventional approaches apply the following simplification to the model in (3.8),

$$\alpha\mathbf{c}(\boldsymbol{\eta})e^{j\varphi}e^{-j\omega_c(\tau+b(t-\tau))} \Rightarrow \tilde{\alpha}\mathbf{c}(\boldsymbol{\eta})e^{-j\omega_c b(t-\tau)}, \tag{3.19}$$

where $\tilde{\alpha} = \alpha e^{j(\varphi-\omega_c\tau)} \in \mathbb{C}$, resulting in the conventional signal model

$$\mathbf{x} = \tilde{\alpha}\mathbf{c}(\boldsymbol{\eta})e^{-j\omega_c b(t-\tau)} + \mathbf{n}, \quad \mathbf{n} \sim \mathcal{CN}(\mathbf{0}, \sigma_n^2\mathbf{I}), \quad \tilde{\alpha} \in \mathbb{C}, \tag{3.20}$$

where the global-phase is defined as $\phi(\boldsymbol{\eta}) = \omega_c b(t-\tau)$. Such simplification allows for the derivation of estimation performance bounds without requiring explicit treatment of the phase terms φ and $\omega_c\tau$. However, by treating the carrier-phase component as part of an unknown complex amplitude rather than as a time delay dependent term, this conventional approach inherently discards the carrier-phase information $\omega_c\tau$, which contains range measurements that could potentially enhance estimation accuracy.

3.5.1 Maximum Likelihood Estimator

The MLE for the conventional model is well known (Medina 2020; Das 2019; Lubeigt 2023b) and treats $\tilde{\alpha}$ as an unknown deterministic parameter. Following the definitions established in Sec. 2.4.3 for the discrete-time model in (3.6), the log-likelihood function is

$$\mathcal{L}(\boldsymbol{\eta}, \tilde{\alpha}) = -\frac{1}{\sigma_n^2}\|\mathbf{x} - \tilde{\alpha}\mathbf{a}(\boldsymbol{\eta})\|^2. \tag{3.21}$$

Maximizing over $\tilde{\alpha}$ yields

$$\widehat{\tilde{\alpha}}(\boldsymbol{\eta}) = \frac{\mathbf{a}(\boldsymbol{\eta})^{\mathrm{H}}\mathbf{x}}{\|\mathbf{a}(\boldsymbol{\eta})\|^2}. \tag{3.22}$$

Substituting back into the likelihood function gives the conventional MLE

$$\widehat{\boldsymbol{\eta}}_{\mathrm{co}} = \arg\max_{\boldsymbol{\eta}} \frac{|\mathbf{a}(\boldsymbol{\eta})^{\mathrm{H}}\mathbf{x}|^2}{\|\mathbf{a}(\boldsymbol{\eta})\|^2}. \tag{3.23}$$

3.5.2 Cramér-Rao Bound

The CRB for the conventional signal model in (3.20) has been extensively documented in the literature (Yau 1992; Van Trees 2002; Medina 2020). This section presents the theoretical bound and its closed-form expressions that characterize the fundamental performance limits when carrier-phase information is absorbed into the complex amplitude.

The SBF (2.13a) is applied to obtain the FIM for the parameters of interest. Following (Medina 2020), the complex amplitude $\tilde{\alpha} = \rho e^{j\phi}$ can be decomposed into magnitude ρ and phase ϕ parameters. The inverse of the FIM yields the complete CRB structure for the full parameter vector $\boldsymbol{\epsilon} = [\sigma_n^2, \rho, \phi, \boldsymbol{\eta}^{\mathrm{T}}]^{\mathrm{T}}$

$$\mathrm{CRB}_{\sigma_n^2|\boldsymbol{\epsilon}} = \frac{1}{N'}(\sigma_n^2)^2, \tag{3.24}$$

$$\mathbf{CRB}_{\boldsymbol{\zeta}|\boldsymbol{\epsilon}} = \begin{bmatrix} \mathrm{CRB}_{\rho|\boldsymbol{\epsilon}} & \mathbf{CRB}_{\rho,\boldsymbol{\theta}|\boldsymbol{\epsilon}}^{\mathrm{T}} \\ \mathbf{CRB}_{\rho,\boldsymbol{\theta}|\boldsymbol{\epsilon}} & \mathbf{CRB}_{\boldsymbol{\theta}|\boldsymbol{\epsilon}} \end{bmatrix}, \quad \mathbf{CRB}_{\boldsymbol{\theta}} = \begin{bmatrix} \mathrm{CRB}_{\phi|\boldsymbol{\epsilon}} & \mathbf{CRB}_{\boldsymbol{\eta},\phi|\boldsymbol{\epsilon}}^{\mathrm{T}} \\ \mathbf{CRB}_{\boldsymbol{\eta},\phi|\boldsymbol{\epsilon}} & \mathbf{CRB}_{\boldsymbol{\eta}|\boldsymbol{\epsilon}} \end{bmatrix}, \tag{3.25}$$

where $\boldsymbol{\zeta} = [\rho, \boldsymbol{\theta}^{\mathrm{T}}]^{\mathrm{T}}$ and $\boldsymbol{\theta} = [\phi, \boldsymbol{\eta}^{\mathrm{T}}]^{\mathrm{T}}$. The bounds for the amplitude ρ, phase ϕ, and propagation parameters $\boldsymbol{\eta}$ are obtained through block-matrix inversion

$$\mathrm{CRB}_{\rho|\boldsymbol{\epsilon}} = \frac{\sigma_n^2}{2\|\mathbf{a}(\boldsymbol{\eta})\|^2} + \rho^2 \frac{\Re\{\mathbf{a}^{\mathrm{H}}(\boldsymbol{\eta}) \frac{\partial \mathbf{a}(\boldsymbol{\eta})}{\partial \boldsymbol{\eta}^{\mathrm{T}}}\} \mathbf{CRB}_{\boldsymbol{\eta}} \Re\{\mathbf{a}^{\mathrm{H}}(\boldsymbol{\eta}) \frac{\partial \mathbf{a}(\boldsymbol{\eta})}{\partial \boldsymbol{\eta}^{\mathrm{T}}}\}^{\mathrm{T}}}{\|\mathbf{a}(\boldsymbol{\eta})\|^4}, \tag{3.26a}$$

$$\mathbf{CRB}_{\boldsymbol{\eta}|\boldsymbol{\epsilon}} = \frac{\sigma_n^2}{2\rho^2 f_s} [\boldsymbol{\Phi}_{\mathrm{co}}(\boldsymbol{\eta})]^{-1}, \tag{3.26b}$$

$$\mathrm{CRB}_{\phi|\boldsymbol{\epsilon}} = \frac{\sigma_n^2}{2\rho^2} \frac{1}{\|\mathbf{a}(\boldsymbol{\eta})\|^2} + \frac{\Im\{\mathbf{a}^{\mathrm{H}}(\boldsymbol{\eta}) \frac{\partial \mathbf{a}(\boldsymbol{\eta})}{\partial \boldsymbol{\eta}^{\mathrm{T}}}\} \mathbf{CRB}_{\boldsymbol{\eta}} \Im\{\mathbf{a}^{\mathrm{H}}(\boldsymbol{\eta}) \frac{\partial \mathbf{a}(\boldsymbol{\eta})}{\partial \boldsymbol{\eta}^{\mathrm{T}}}\}^{\mathrm{T}}}{\|\mathbf{a}(\boldsymbol{\eta})\|^4}, \tag{3.26c}$$

$$\mathbf{CRB}_{\boldsymbol{\eta},\phi|\boldsymbol{\epsilon}} = -\mathbf{CRB}_{\boldsymbol{\eta}|\boldsymbol{\epsilon}} \frac{\Im\{\mathbf{a}^{\mathrm{H}}(\boldsymbol{\eta}) \frac{\partial \mathbf{a}(\boldsymbol{\eta})}{\partial \boldsymbol{\eta}^{\mathrm{T}}}\}^{\mathrm{T}}}{\|\mathbf{a}(\boldsymbol{\eta})\|^2}, \tag{3.26d}$$

where the information matrix is defined as

$$\boldsymbol{\Phi}_{\mathrm{co}}(\boldsymbol{\eta}) = \Re\left\{ \left(\frac{\partial \mathbf{a}(\boldsymbol{\eta})}{\partial \boldsymbol{\eta}^{\mathrm{T}}} \right)^{\mathrm{H}} \boldsymbol{\Pi}^{\perp}_{\mathbf{a}(\boldsymbol{\eta})} \frac{\partial \mathbf{a}(\boldsymbol{\eta})}{\partial \boldsymbol{\eta}^{\mathrm{T}}} \right\}, \tag{3.27}$$

with the projector operator $\boldsymbol{\Pi}^{\perp}_{\mathbf{a}(\boldsymbol{\eta})} = \mathbf{I}_N - \boldsymbol{\Pi}_{\mathbf{a}(\boldsymbol{\eta})}$ denoting the projection onto the orthogonal complement of $\mathbf{a}(\boldsymbol{\eta})$,

$$\boldsymbol{\Pi}_{\mathbf{a}(\boldsymbol{\eta})} = \frac{\mathbf{a}(\boldsymbol{\eta})\mathbf{a}(\boldsymbol{\eta})^{\mathrm{H}}}{\|\mathbf{a}(\boldsymbol{\eta})\|^2}. \tag{3.28}$$

By expanding $\boldsymbol{\Pi}_{\mathbf{a}(\boldsymbol{\eta})}$, equation (3.27) can be rewritten as

$$\begin{aligned} \boldsymbol{\Phi}_{\mathrm{co}}(\boldsymbol{\eta}) = \Re\left\{ \left(\frac{\partial \mathbf{a}(\boldsymbol{\eta})}{\partial \boldsymbol{\eta}^{\mathrm{T}}} \right)^{\mathrm{H}} \left(\frac{\partial \mathbf{a}(\boldsymbol{\eta})}{\partial \boldsymbol{\eta}^{\mathrm{T}}} \right) \right\} \\ - \frac{\Re\{\mathbf{a}(\boldsymbol{\eta})^H \frac{\partial \mathbf{a}(\boldsymbol{\eta})}{\partial \boldsymbol{\eta}^{\mathrm{T}}}\}^{\mathrm{T}} \Re\{\mathbf{a}(\boldsymbol{\eta})^H \frac{\partial \mathbf{a}(\boldsymbol{\eta})}{\partial \boldsymbol{\eta}^{\mathrm{T}}}\}}{\|\mathbf{a}(\boldsymbol{\eta})\|^2} \\ - \frac{\Im\{\mathbf{a}(\boldsymbol{\eta})^H \frac{\partial \mathbf{a}(\boldsymbol{\eta})}{\partial \boldsymbol{\eta}^{\mathrm{T}}}\}^{\mathrm{T}} \Im\{\mathbf{a}(\boldsymbol{\eta})^H \frac{\partial \mathbf{a}(\boldsymbol{\eta})}{\partial \boldsymbol{\eta}^{\mathrm{T}}}\}}{\|\mathbf{a}(\boldsymbol{\eta})\|^2}, \end{aligned} \tag{3.29}$$

which provides a convenient formulation for comparison in subsequent chapters.

Closed-form expressions are derived to facilitate practical interpretation and analysis. These expressions exploit the signal model structure and provide explicit dependencies on system parameters. Computing the closed-form representation requires calculating the signal derivatives with respect to the parameters. This procedure is also employed in Chapters 4 and 5, with detailed explanations provided in Appendix B.3. The results presented here are direcly obtained from (Medina 2020; Das 2019). For the signal model under consideration, the partial derivative with respect to $\boldsymbol{\eta}$ yields

$$\frac{\partial \mathbf{a}(\boldsymbol{\eta})}{\partial \boldsymbol{\eta}} = -\mathbf{Q}\mathbf{v}(n\mathrm{T_s} - \tau) e^{-j\omega_c b(t-\tau)}. \tag{3.30}$$

Under the band-limited assumption, the derivative terms in equation (3.30) can be expressed in continuous time-domain via the Nyquist-Shannon theorem, and further manipulated to yield a closed-form of the FIM in equation (3.29). The matrix $\mathbf{Q}$ and continuous-time vector $\mathbf{v}(t-\tau)$ are defined as

$$\mathbf{Q} = \begin{bmatrix} -j\omega_c b & 0 & 1 \\ 0 & j\omega_c & 0 \end{bmatrix}, \quad \mathbf{v}(t-\tau) = \begin{bmatrix} c(t;\boldsymbol{\eta}) \\ (t-\tau)c(t;\boldsymbol{\eta}) \\ \dot{c}(t;\boldsymbol{\eta}) \end{bmatrix}. \tag{3.31}$$

where $\dot{c}(t;\boldsymbol{\eta})$ is the first time-derivative of $c(t;\boldsymbol{\eta})$. These terms allow to express the derivatives from the FIM in equation (3.29) as,

$$\left(\frac{\partial a(t;\boldsymbol{\eta})}{\partial \boldsymbol{\eta}^{\mathrm{T}}}\right)^{\mathrm{H}} \frac{\partial a(t;\boldsymbol{\eta})}{\partial \boldsymbol{\eta}^{\mathrm{T}}} = \mathbf{Q}\Big(\mathbf{v}(t-\tau)\,\mathbf{v}^{\mathrm{H}}(t-\tau)\Big)\mathbf{Q}^{\mathrm{H}}, \tag{3.32a}$$

$$a(t;\boldsymbol{\eta})^{\mathrm{H}} \frac{\partial a(t;\boldsymbol{\eta})}{\partial \boldsymbol{\eta}^{\mathrm{T}}} = -\Big(\mathbf{v}(t-\tau)c^{*}(t;\boldsymbol{\eta})\Big)^{\mathrm{T}}\mathbf{Q}^{\mathrm{T}}, \tag{3.32b}$$

for which the Nyquist-Shannon theorem establishes the equivalence

$$\lim_{(N_1',N_2')\to(-\infty,\infty)} T_s \sum_{n=N_1'}^{N2'} \mathbf{v}(n\mathrm{T_s};\boldsymbol{\eta})\,\mathbf{v}^{\mathrm{H}}(n\mathrm{T_s};\boldsymbol{\eta}) = f_s \int_{-\infty}^{\infty} \mathbf{v}(t;\boldsymbol{\eta})\,\mathbf{v}^{\mathrm{H}}(t;\boldsymbol{\eta})\,dt = f_s\mathbf{W}, \tag{3.33a}$$

$$\lim_{(N_1',N_2')\to(-\infty,\infty)} T_s \sum_{n=N_1'}^{N2'} \mathbf{v}(n\mathrm{T_s};\boldsymbol{\eta})\mathbf{c}(n\mathrm{T_s};\boldsymbol{\eta}) = f_s \int_{-\infty}^{\infty} \mathbf{v}(t;\boldsymbol{\eta})c^{*}(t;\boldsymbol{\eta})\,dt = f_s\mathbf{w}, \tag{3.33b}$$

where the vector $\mathbf{w}$ and matrix $\mathbf{W}$ contain the signal correlation terms

$$\mathbf{w} = \begin{bmatrix} w_1 \\ w_2 \\ w_3 \end{bmatrix}, \quad \mathbf{W} = \begin{bmatrix} w_1 & w_2^{*} & w_3^{*} \\ w_2 & W_{2,2} & w_4^{*} \\ w_3 & w_4 & W_{3,3} \end{bmatrix}, \tag{3.34}$$

whose individual elements are derived in more detail in Appendix B.3. The result in (3.33) leads to the following reformulation of the derivatives in equation (3.32),

$$\left(\frac{\partial \mathbf{a}(\boldsymbol{\eta})}{\partial \boldsymbol{\eta}^{\mathrm{T}}}\right)^{\mathrm{H}} \frac{\partial \mathbf{a}(\boldsymbol{\eta})}{\partial \boldsymbol{\eta}^{\mathrm{T}}} = f_s\mathbf{Q}\mathbf{W}\mathbf{Q}^{\mathrm{H}}, \quad \mathbf{a}(\boldsymbol{\eta})^{\mathrm{H}} \frac{\partial \mathbf{a}(\boldsymbol{\eta})}{\partial \boldsymbol{\eta}^{\mathrm{T}}} = -f_s\left(\mathbf{Q}\mathbf{w}\right)^{\mathrm{T}}, \tag{3.35}$$

and consequently to the closed-form FIM structure,

$$\begin{aligned} \boldsymbol{\Phi}_{\mathrm{co}}(\boldsymbol{\eta}) &= \Re\left\{\mathbf{Q}\mathbf{W}\mathbf{Q}^{H} - \frac{(\mathbf{Q}\mathbf{w})(\mathbf{Q}\mathbf{w})^{H}}{w_1}\right\}, \\ &= \Re\left\{\mathbf{Q}\mathbf{W}\mathbf{Q}^{H}\right\} - \frac{\Re\{\mathbf{Q}\mathbf{w}\}\Re\{\mathbf{Q}\mathbf{w}\}^{\mathrm{T}}}{w_1} - \frac{\Im\{\mathbf{Q}\mathbf{w}\}\Im\{\mathbf{Q}\mathbf{w}\}^{\mathrm{T}}}{w_1}, \qquad (3.36a) \\ &= \begin{bmatrix} W_{3,3} - \frac{|w_3|^2}{w_1} & \omega_c\Im\left\{w_4 - \frac{w_2w_3}{w_1}\right\} \\ \omega_c\Im\left\{w_4 - \frac{w_2w_3}{w_1}\right\} & \omega_c^2\left(W_{2,2} - \frac{w_2^2}{w_1}\right) \end{bmatrix}. \qquad (3.36b) \end{aligned}$$

An important structural property of $\boldsymbol{\Phi}_{\mathrm{co}}(\boldsymbol{\eta})$ in (3.36) emerges for the real-valued baseband signals employed in this analysis. The off-diagonal coupling terms contain the imaginary part operator $\Im\{w_4 - \frac{w_2w_3}{w_1}\}$, which vanishes for real baseband signals since all correlation integrals $w_k \in \mathbb{R}$. Consequently, the conventional FIM becomes diagonal, indicating that time-delay and Doppler parameters are statistically decoupled in conventional estimation. This property enables independent parameter optimization without statistical penalty, contrasting with the enhanced frameworks developed in subsequent chapters where explicit carrier-phase treatment introduces parameter coupling through the carrier frequency terms.

Figure 3.2 presents simulation results validating the conventional CRB (3.36) and MLE (3.23) using three representative GNSS signals: GPS L1 C/A (1575.42 MHz), GPS L5-I (1176.45 MHz), and Galileo E5 (1191.795 MHz). Following the methodology in (Medina 2020), atmospheric delays and instrumental biases are excluded to isolate fundamental signal characteristics. The time-delay estimation results in Figure 3.2a show asymptotic convergence of the conventional MLE to the

theoretical CRB across all configurations, confirming the mathematical correctness of the closed-form expressions. Different asymptotic performance levels reflect varying sampling frequencies and signal bandwidths, with wider bandwidth signals achieving lower bounds. Code-based ranging remains far from centimeter-level precision, with GPS L1 C/A achieving meter-level accuracy and Galileo E5 reaching decimeter-level performance. For phase estimation in Figure 3.2b, normalized carrier wavelengths enable direct comparison across carrier frequencies. For real-valued baseband signals, phase estimation performance depends solely on carrier frequency f_c and SNR, independent of code structure, as Fisher Information for phase scales with ω_c as seen in equation (3.31). This normalization allows all signals to converge to the same theoretical bound.

These results demonstrate that achieving centimeter-level ranging through code-based time-delay estimation alone is not feasible. The only viable approach requires exploiting phase measurements through techniques such as RTK or PPP. However, these methodologies rely on differential corrections or precise products, a priori not unavailable in space scenarios, presenting a technical challenge for the NOIRE mission. This motivates the enhanced time-delay estimation frameworks developed in subsequent chapters that exploit carrier-phase information directly within the ranging process.

The performance bound obtained for the GPS L1 C/A signal establishes a baseline conventional approach for TDE, providing one reference against which the carrier-phase enhanced methods developed in subsequent chapters are evaluated.

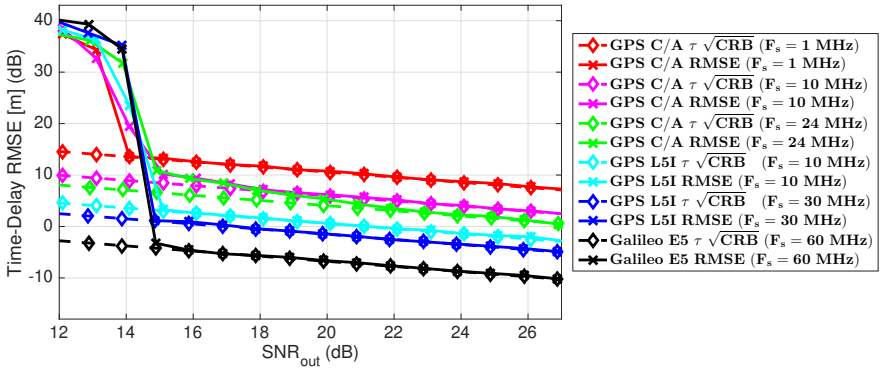

(**a**)

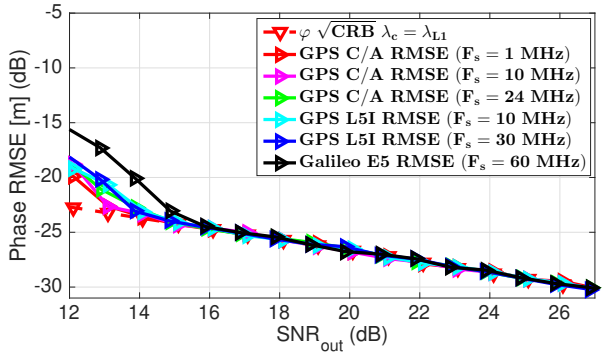

(**b**)

Figure 3.2: Validation of theoretical bounds for (a) time-delay and (b) phase estimation using GPS L1 C/A, GPS L5-I, and Galileo E5 signals. The asymptotic convergence of the MLE to the CRB confirms the derived expressions.

3.6 Towards Enhanced Time-delay Estimation Methods

The signal processing framework presented in this chapter establishes the basis for conventional time-delay estimation, where the hardware-induced phase term φ is typically absorbed into a complex amplitude parameter. However, the NOIRE mission's centimeter-level ranging requirements demand exploitation of all available signal information, particularly the carrier-phase component that offers wavelength-scale precision. While conventional approaches treat the carrier phase as a nuisance parameter, the identifiability analysis that follows demonstrate that both hardware-induced and propagation-induced phase components can be uniquely determined under appropriate conditions. This revelation motivates the development of an extended estimation framework in Chapter 4 that explicitly incorporates phase observables, enabling performance improvements of several orders of magnitude when partial or complete phase compensation is achievable through calibration or auxiliary measurements.

3.6.1 Parameter Identifiability

The concept of parameter identifiability concerns whether the unknown parameters of a statistical model can be uniquely determined from the observed data. Identifiability is essential, as it guarantees that the parameters are distinguishable from the observations and allows the derivation of lower bounds on their estimation error.

Formally, let the observed data $\mathbf{x} \in \mathbb{C}^N$ follow the probability density function (PDF) $P(\mathbf{x};\boldsymbol{\epsilon})$, parameterized by the vector $\boldsymbol{\epsilon}$. The parameter vector is identifiable if there exists a unique mapping between the parameter space and the space of PDFs, i.e.,

$$\forall\,(\boldsymbol{\epsilon}_1,\boldsymbol{\epsilon}_2)\,|\boldsymbol{\epsilon}_1 \neq \boldsymbol{\epsilon}_2 \;\Rightarrow\; P(\mathbf{x};\boldsymbol{\epsilon}_1) \neq P(\mathbf{x};\boldsymbol{\epsilon}_2), \tag{3.37}$$

or equivalently,

$$P(\mathbf{x};\boldsymbol{\epsilon}_1) = P(\mathbf{x};\boldsymbol{\epsilon}_2) \;\Rightarrow\; \boldsymbol{\epsilon}_1 = \boldsymbol{\epsilon}_2. \tag{3.38}$$

For the signal model in (3.8), $P(\mathbf{x};\boldsymbol{\epsilon})$ follows a complex Gaussian distribution. Assuming $\mathbf{b}(\boldsymbol{\theta}) = \mathbf{a}(\boldsymbol{\eta})e^{j\varphi}$, the equality $P(\mathbf{x};\boldsymbol{\epsilon}_1) = P(\mathbf{x};\boldsymbol{\epsilon}_2)$ requires equality of their means and covariance matrices. Hence, equation (3.38) becomes

$$P(\mathbf{x};\boldsymbol{\epsilon}_1) = P(\mathbf{x};\boldsymbol{\epsilon}_2) \;\Leftrightarrow\; \begin{pmatrix}\mathbf{b}(\boldsymbol{\theta}_1)\alpha_1 = \mathbf{b}(\boldsymbol{\theta}_2)\alpha_2 \\ (\sigma_n^2)_1 = (\sigma_n^2)_2\end{pmatrix} \;\Rightarrow\; \boldsymbol{\epsilon}_1 = \boldsymbol{\epsilon}_2. \tag{3.39}$$

where $\alpha_1, \alpha_2 \in \mathbb{R}$. To facilitate the analysis, the model can be expressed in real-valued form

$$\underline{\mathbf{x}} = \begin{bmatrix}\Re\{\mathbf{x}\}\\ \Im\{\mathbf{x}\}\end{bmatrix} \in \mathbb{R}^{2N}, \quad \underline{\mathbf{b}}(\boldsymbol{\theta}) = \begin{bmatrix}\Re\{\mathbf{b}(\boldsymbol{\theta})\}\\ \Im\{\mathbf{b}(\boldsymbol{\theta})\}\end{bmatrix} \in \mathbb{R}^{2N}, \quad \underline{\mathbf{n}} = \begin{bmatrix}\Re\{\mathbf{n}\}\\ \Im\{\mathbf{n}\}\end{bmatrix} \in \mathbb{R}^{2N}, \tag{3.40}$$

where $\underline{\mathbf{n}} \sim \mathcal{N}\left(\mathbf{0}, \frac{\sigma_n^2}{2}\mathbf{I}_{2N}\right)$, and where the following relationship applies to ensure equivalent results hold in both domains:

$$\underline{\mathbf{A}}^T\underline{\mathbf{B}} = \Re\{\mathbf{A}\}^T\Re\{\mathbf{B}\} + \Im\{\mathbf{A}\}^T\Im\{\mathbf{B}\} = \Re\left\{\mathbf{A}^H\mathbf{B}\right\}. \tag{3.41}$$

being $\underline{\mathbf{A}}$ and $\underline{\mathbf{B}}$ are two vectors expressed in such real-valued representation.

From (3.39), the equality of Gaussian means can be expressed as

$$\mathbf{b}(\boldsymbol{\theta}_1)\alpha_1 = \mathbf{b}(\boldsymbol{\theta}_2)\alpha_2 \Leftrightarrow \|\mathbf{b}(\boldsymbol{\theta}_1)\alpha_1 - \mathbf{b}(\boldsymbol{\theta}_2)\alpha_2\|^2 = 0 \Leftrightarrow \|\underline{\mathbf{b}}(\boldsymbol{\theta}_1)\alpha_1 - \underline{\mathbf{b}}(\boldsymbol{\theta}_2)\alpha_2\|^2 = 0.$$

This equality condition implies that both signal vectors are collinear, or equivalently,

$$\|\underline{\mathbf{b}}(\boldsymbol{\theta}_1)\alpha_1 - \underline{\mathbf{b}}(\boldsymbol{\theta}_2)\alpha_2\|^2 = 0 \Leftrightarrow \underline{\mathbf{b}}(\boldsymbol{\theta}_1) = \underline{\mathbf{b}}(\boldsymbol{\theta}_2)\frac{\alpha_2}{\alpha_1} \Leftrightarrow |\underline{\mathbf{b}}(\boldsymbol{\theta}_1)^T\underline{\mathbf{b}}(\boldsymbol{\theta}_2)| = \|\underline{\mathbf{b}}(\boldsymbol{\theta}_1)\|\|\underline{\mathbf{b}}(\boldsymbol{\theta}_2)\|.$$

Under the hypothesis $H_1 : \boldsymbol{\theta}_1 \neq \boldsymbol{\theta}_2$, this perfect alignment cannot hold, and instead,

$$H_1 : \boldsymbol{\theta}_1 \neq \boldsymbol{\theta}_2 \;\Rightarrow\; \begin{cases} |\underline{\mathbf{b}}(\boldsymbol{\theta}_1)^T \underline{\mathbf{b}}(\boldsymbol{\theta}_2)| < \|\underline{\mathbf{b}}(\boldsymbol{\theta}_1)\| \|\underline{\mathbf{b}}(\boldsymbol{\theta}_2)\|, \\ \qquad\qquad \Updownarrow \\ |\Re\{\mathbf{b}(\boldsymbol{\theta}_1)^H \mathbf{b}(\boldsymbol{\theta}_2)\}| < \|\mathbf{b}(\boldsymbol{\theta}_1)\| \|\mathbf{b}(\boldsymbol{\theta}_2)\|. \end{cases} \tag{3.42}$$

In this case, the distance between the two mean vectors is nonzero

$$\|\underline{\mathbf{b}}(\boldsymbol{\theta}_1)\alpha_1 - \underline{\mathbf{b}}(\boldsymbol{\theta}_2)\alpha_2\|^2 \neq 0.$$

Therefore, if the equality $\|\underline{\mathbf{b}}(\boldsymbol{\theta}_1)\alpha_1 - \underline{\mathbf{b}}(\boldsymbol{\theta}_2)\alpha_2\|^2 = 0$ were ever satisfied under H_1, it would necessarily imply $(\alpha_1, \boldsymbol{\theta}_1) = (\alpha_2, \boldsymbol{\theta}_2)$, contradicting the assumption $\boldsymbol{\theta}_1 \neq \boldsymbol{\theta}_2$. This contradiction confirms that different parameter pairs produce distinct mean vectors, and thus distinct PDFs.

Consequently, the sufficient condition ensuring identifiability can be written as

$$|\mathbf{b}(\boldsymbol{\theta}_1)^H \mathbf{b}(\boldsymbol{\theta}_2)| < \|\mathbf{b}(\boldsymbol{\theta}_1)\| \|\mathbf{b}(\boldsymbol{\theta}_2)\|, \quad \forall\, \boldsymbol{\theta}_1 \neq \boldsymbol{\theta}_2. \tag{3.43}$$

This inequality guarantees that the signal vectors corresponding to distinct parameter values are never collinear, which ensures a one-to-one mapping between the parameter vector $\boldsymbol{\epsilon}$ and the PDF $P(\mathbf{x}; \boldsymbol{\epsilon})$. Hence, the parameters of the model are identifiable.

3.6.2 Application to Signal Transmission

Under the observation model in (3.6), the general identifiability condition in (3.43) particularizes to the signal model $\mathbf{b}(\boldsymbol{\theta}) = \mathbf{a}(\boldsymbol{\eta})e^{j\varphi}$. In this case, (3.43) becomes

$$\left|\mathbf{a}(\boldsymbol{\eta}_1)^H \mathbf{a}(\boldsymbol{\eta}_2)\right| < \|\mathbf{a}(\boldsymbol{\eta}_1)\| \, \|\mathbf{a}(\boldsymbol{\eta}_2)\|, \quad \forall\, \boldsymbol{\eta}_1 \neq \boldsymbol{\eta}_2, \tag{3.44}$$

which asserts that distinct parameter vectors $\boldsymbol{\eta}_1$ and $\boldsymbol{\eta}_2$ must produce distinct signal vectors $\mathbf{a}(\boldsymbol{\eta}_1)$ and $\mathbf{a}(\boldsymbol{\eta}_2)$ that are not collinear in the complex space. In other words, $\mathbf{a}(\boldsymbol{\eta})$ must vary sufficiently with $\boldsymbol{\eta}$ such that its realizations do not become linearly dependent.

To demonstrate this formally, consider two parameter vectors

$$\boldsymbol{\epsilon}_1 = [\alpha_1, \varphi_1, \boldsymbol{\eta}_1], \qquad \boldsymbol{\epsilon}_2 = [\alpha_2, \varphi_2, \boldsymbol{\eta}_2],$$

and assume the equality $P(\mathbf{x}; \boldsymbol{\epsilon}_1) = P(\mathbf{x}; \boldsymbol{\epsilon}_2)$. Following (3.39), equality of the Gaussian PDFs implies equality of their mean vectors

$$\mathbf{a}(\boldsymbol{\eta}_1)\, \alpha_1 e^{j\varphi_1} = \mathbf{a}(\boldsymbol{\eta}_2)\, \alpha_2 e^{j\varphi_2}. \tag{3.45}$$

Rearranging terms gives

$$\mathbf{a}(\boldsymbol{\eta}_1) = \mathbf{a}(\boldsymbol{\eta}_2)\, \frac{\alpha_2}{\alpha_1} e^{j(\varphi_2 - \varphi_1)}. \tag{3.46}$$

Taking the inner product of both sides of (3.45) with $\mathbf{a}(\boldsymbol{\eta}_2)$ and normalizing by the corresponding norms as shown in Appendix A, yields

$$\frac{\left|\mathbf{a}(\boldsymbol{\eta}_1)^H \mathbf{a}(\boldsymbol{\eta}_2)\right|}{\|\mathbf{a}(\boldsymbol{\eta}_1)\| \, \|\mathbf{a}(\boldsymbol{\eta}_2)\|} = 1. \tag{3.47}$$

Equation (3.47) corresponds to equality in the Cauchy–Schwarz inequality, which occurs if and only if $\mathbf{a}(\boldsymbol{\eta}_1)$ and $\mathbf{a}(\boldsymbol{\eta}_2)$ are linearly dependent. This situation violates (3.44), which requires the strict inequality

$$\left|\mathbf{a}(\boldsymbol{\eta}_1)^H \mathbf{a}(\boldsymbol{\eta}_2)\right| < \|\mathbf{a}(\boldsymbol{\eta}_1)\| \, \|\mathbf{a}(\boldsymbol{\eta}_2)\|,$$

for all $\boldsymbol{\eta}_1 \neq \boldsymbol{\eta}_2$. Therefore, equality in (3.45) can only occur if

$$[\alpha_1, \varphi_1, \boldsymbol{\eta}_1] = [\alpha_2, \varphi_2, \boldsymbol{\eta}_2],$$

which proves that the parameter vector $\boldsymbol{\epsilon}$ is identifiable under condition (3.44).

This result shows that the identifiability of $\boldsymbol{\epsilon}$ is entirely governed by the identifiability of $\boldsymbol{\eta}$. The vector $\boldsymbol{\eta}$ captures propagation-induced effects on the baseband signal $\mathbf{a}(\boldsymbol{\eta})$, while φ accounts for hardware-induced phase shifts. If the signal structure $\mathbf{a}(\boldsymbol{\eta})$ guarantees that distinct $\boldsymbol{\eta}$ yield distinct signal vectors, i.e. satisfying (3.44), then φ is also uniquely identifiable. This overturns the conventional view that the hardware phase φ cannot be separated from the propagation-dependent phase $\psi(\boldsymbol{\eta})$ in in $\phi(\boldsymbol{\eta}) = \varphi + \psi(\boldsymbol{\eta})$. Hence, when $\psi(\boldsymbol{\eta})$ can be independently characterized through the baseband model, the hardware phase φ becomes uniquely determinable, enabling improved parameter recovery and reduced ambiguity in time-delay estimation.

3.7 Conclusion

This chapter established the theoretical basis for time-delay estimation by extending the general CSM framework to signal transmission scenarios. The conventional approach, which constitutes the current state of the art, absorbs the carrier-phase information into a complex amplitude parameter due to prior belief that propagation and hardware phase terms could not be individually estimated, which in turn reduced the complexity of TDE assessments. This simplification, while mathematically convenient, inherently discards the fine phase structure that could potentially enhance ranging precision. The theoretical analysis demonstrates that conventional TDE methods achieve well-established performance bounds, as validated through simulations with GPS and Galileo signals. The MLE and CRB derivations provide the baseline performance metrics against which enhanced methods can be evaluated. Crucially, the identifiability analysis in Section 3.6.1 reveals that both hardware-induced phase φ and propagation-induced phase components are uniquely determinable under appropriate conditions, contradicting the historical assumption that justified treating them as nuisance parameters. This finding motivates the exploration of alternative phase compensation strategies that explicitly exploit carrier-phase observables. The conventional framework is used to develop the enhanced estimation methods presented in subsequent chapters, where partial or complete phase compensation enables performance improvements necessary to meet the NOIRE mission's centimeter-level ranging requirements.

Chapter 4

Time-Delay Estimation with Optimal Phase Compensation

4.1 Introduction

The exploitation of carrier-phase measurements in time-delay estimation systems offers theoretical performance improvements of several orders of magnitude compared to code-based methods. This chapter examines the limiting case where hardware-induced phase offsets (Teunissen 2017, §17.6) can be perfectly compensated, establishing the theoretical performance limits achievable when the carrier phase purely reflects propagation-induced delays. While this scenario represents an idealization not achievable in practice, its analysis is considered of interest from a theoretical point of view to determine the Most Powerful (MP) test (De Maio 2016, 1.3.1), representing the upper bound for the achievable performance. This serves a critical role in system design by establishing performance benchmarks and determining whether theoretical limits meet application-specific requirements.

Building upon the identifiability analysis presented in Section 3.6.1, which demonstrated that hardware-induced phase φ satisfies the necessary and sufficient conditions for unique parameter recovery, this chapter develops the conditional signal model and associated performance bounds under perfect phase knowledge. The theoretical developments presented in this chapter build upon the framework established in (Bernabeu 2023b; Bernabeu 2023a).

The chapter is organized as follows. Section 4.2 formulates the signal model under perfect phase compensation, establishing the mathematical framework where hardware-induced phase offsets are completely eliminated. Section 4.3 derives the constrained MLE that exploits carrier-phase information while maintaining the real-valued amplitude constraint. Section 4.4 develops the corresponding CRB expressions that quantify optimal achievable performance, with closed-form formulations presented in Section 4.4.1 for wide-band, narrow-band, and delay-only scenarios. Section 4.5 analyzes the ambiguity function structure and its connection to the FIM, revealing how carrier-phase modulation creates the characteristic comb pattern that determines estimation accuracy. Section 4.6 establishes the simulation framework and presents numerical results that validate the theoretical predictions and demonstrate the orders-of-magnitude improvement possible when carrier-phase information is fully exploited.

4.2 Signal Model under Perfect Phase Compensation

Perfect compensation of the phase term φ represents the case where this hardware-induced phase offset is completely known and can be removed from the received signal. Building upon the signal transmission model from Section 3.3, the perfect phase compensation scenario can be expressed as,

$$\begin{cases} \mathbf{x} = \alpha \mathbf{c}(\boldsymbol{\eta}) e^{j(\varphi + \psi(\boldsymbol{\eta}))} + \mathbf{n}, \quad \mathbf{n} \sim \mathcal{CN}\left(\mathbf{0}, \sigma_n^2 \mathbf{I}_{N'}\right) \\ x_a = \varphi \end{cases}, \quad \alpha \in \mathbb{R}^+, \tag{4.1}$$

where x_a represents the perfectly known hardware-induced phase, enabling phase compensation

$$\mathbf{x} e^{-j x_a} = \mathbf{x} e^{-j\varphi} = \alpha \mathbf{c}(\boldsymbol{\eta}) e^{j\psi(\boldsymbol{\eta})} + \mathbf{n}. \tag{4.2}$$

Following the discretization procedure established in Section 3.3, the discrete observation vector contains $N' = N_2' - N_1' + 1$ samples with $\mathbf{n} \sim \mathcal{CN}(\mathbf{0}, \sigma_n^2 \mathbf{I}_{N'})$ and sampling period $\mathrm{T_s} = 1/f_s$ where $f_s \geq B$. The complete vector of unknown parameters is,

$$\boldsymbol{\epsilon} = [\sigma_n^2, \boldsymbol{\zeta}^{\mathrm{T}}]^{\mathrm{T}}, \quad \boldsymbol{\zeta} = [\alpha, \boldsymbol{\theta}^{\mathrm{T}}]^{\mathrm{T}}, \quad \boldsymbol{\theta} = [\varphi, \boldsymbol{\eta}^{\mathrm{T}}]^{\mathrm{T}}, \quad \boldsymbol{\eta} = [\tau, b]^{\mathrm{T}} \tag{4.3}$$

.

4.3 Maximum Likelihood Estimator

This section derives the MLE for $\boldsymbol{\eta}$ under the perfect phase compensation scenario established in Section 4.2. The MLE determines the optimal TDE performance achievable for the signal model in equation (4.1), which assumes perfect knowledge of the hardware-induced phase φ. The efficiency property of the CSM MLE, defined as its ability to attain the CRB, derived in the subsequent section, establishes the SNR threshold above which optimal time-delay estimation performance is realized.

4.3.1 Constrained Maximum Likelihood Framework

Since φ is known through x_a, the likelihood function for (4.1) of the phase-compensated signal $\mathbf{x} e^{-j x_a} = \mathbf{x} e^{-j\varphi}$ yields

$$P(\mathbf{x} e^{-j\varphi}; \boldsymbol{\epsilon}) = \frac{1}{(\pi \sigma_n^2)^{N'}} \exp\left(-\frac{\|\mathbf{x} e^{-j\varphi} - \alpha \mathbf{c}(\boldsymbol{\eta}) e^{j\psi(\boldsymbol{\eta})}\|^2}{\sigma_n^2} \right). \tag{4.4}$$

Defining $\mathbf{a}(\boldsymbol{\eta}) = \mathbf{c}(\boldsymbol{\eta}) e^{j\psi(\boldsymbol{\eta})}$ and $\mathbf{x} \leftarrow \mathbf{x} e^{-j\varphi}$, the log-likelihood function becomes,

$$\mathcal{S}_0(\mathbf{x}; \boldsymbol{\epsilon}) = \frac{\|\mathbf{x} - \mathbf{a}(\boldsymbol{\eta})\alpha\|^2}{\sigma_n^2} + N' \ln(\pi \sigma_n^2). \tag{4.5}$$

To facilitate the derivation, the complex signal model is expressed in real-valued form

$$\underline{\mathbf{x}} = \begin{bmatrix} \Re\{\mathbf{x}\} \\ \Im\{\mathbf{x}\} \end{bmatrix} \in \mathbb{R}^{2N'}, \quad \underline{\mathbf{a}}(\boldsymbol{\eta}) = \begin{bmatrix} \Re\{\mathbf{a}(\boldsymbol{\eta})\} \\ \Im\{\mathbf{a}(\boldsymbol{\eta})\} \end{bmatrix} \in \mathbb{R}^{2N'}, \tag{4.6}$$

noting that $\|\mathbf{x} - \mathbf{a}(\boldsymbol{\eta})\alpha\|^2 = \|\underline{\mathbf{x}} - \underline{\mathbf{a}}(\boldsymbol{\eta})\alpha\|^2$ and the relationship in (3.41) holds.

The nuisance parameters σ_n^2 and α must be eliminated through their maximum likelihood estimates. For σ_n^2, setting the derivative with respect to σ_n^2 to zero yields

$$\widehat{\sigma_n^2} = \frac{\|\underline{\mathbf{x}} - \underline{\mathbf{a}}(\boldsymbol{\eta})\alpha\|^2}{N'}. \tag{4.7}$$

Substituting this estimate back into $\mathcal{S}_0$ produces

$$\begin{aligned}\mathcal{S}_1(\mathbf{x};\boldsymbol{\eta},\alpha) &= N' + N'\ln\left(\frac{\pi\|\underline{\mathbf{x}}-\underline{\mathbf{a}}(\boldsymbol{\eta})\alpha\|^2}{N'}\right)\\ &= N'\ln\left(\|\underline{\mathbf{x}}-\underline{\mathbf{a}}(\boldsymbol{\eta})\alpha\|^2\right)+\text{const},\end{aligned} \tag{4.8}$$

where the constant terms do not depend on the parameters of interest. Therefore

$$\widehat{\boldsymbol{\zeta}} = \arg\min_{\boldsymbol{\theta},\alpha\in\mathbb{R}^+}\{\|\underline{\mathbf{x}}-\underline{\mathbf{a}}(\boldsymbol{\eta})\alpha\|^2\}. \tag{4.9}$$

The cost function can be decomposed using the projectors defined in (3.28). The norm decomposes as,

$$\|\underline{\mathbf{x}}-\underline{\mathbf{a}}(\boldsymbol{\eta})\alpha\|^2 = \|(\boldsymbol{\Pi}_{\underline{\mathbf{a}}(\boldsymbol{\eta})}+\boldsymbol{\Pi}^{\perp}_{\underline{\mathbf{a}}(\boldsymbol{\eta})})(\underline{\mathbf{x}}-\underline{\mathbf{a}}(\boldsymbol{\eta})\alpha)\|^2 = \|\boldsymbol{\Pi}_{\underline{\mathbf{a}}(\boldsymbol{\eta})}(\underline{\mathbf{x}}-\underline{\mathbf{a}}(\boldsymbol{\eta})\alpha)\|^2 + \|\boldsymbol{\Pi}^{\perp}_{\underline{\mathbf{a}}(\boldsymbol{\eta})}\underline{\mathbf{x}}\|^2. \tag{4.10}$$

Expanding the first term yields

$$\begin{aligned}\|\boldsymbol{\Pi}_{\underline{\mathbf{a}}(\boldsymbol{\eta})}(\underline{\mathbf{x}}-\underline{\mathbf{a}}(\boldsymbol{\eta})\alpha)\|^2 &= \left\|\underline{\mathbf{a}}(\boldsymbol{\eta})\left(\frac{\underline{\mathbf{a}}(\boldsymbol{\eta})^{\mathrm{T}}\underline{\mathbf{x}}}{\underline{\mathbf{a}}(\boldsymbol{\eta})^{\mathrm{T}}\underline{\mathbf{a}}(\boldsymbol{\eta})}-\alpha\right)\right\|^2\\ &= \|\underline{\mathbf{a}}(\boldsymbol{\eta})\|^2\left(\widehat{\alpha}_u(\boldsymbol{\eta})-\alpha\right)^2,\end{aligned} \tag{4.11}$$

where the unconstrained amplitude estimate is,

$$\widehat{\alpha}_u(\boldsymbol{\eta}) = \frac{\underline{\mathbf{a}}(\boldsymbol{\eta})^{\mathrm{T}}\underline{\mathbf{x}}}{\underline{\mathbf{a}}(\boldsymbol{\eta})^{\mathrm{T}}\underline{\mathbf{a}}(\boldsymbol{\eta})} = \frac{\Re\{\mathbf{a}(\boldsymbol{\eta})^{\mathrm{H}}\mathbf{x}\}}{\|\mathbf{a}(\boldsymbol{\eta})\|^2}. \tag{4.12}$$

The cost function thus becomes,

$$\mathcal{S}_1(\mathbf{x};\boldsymbol{\zeta}) = \|\underline{\mathbf{a}}(\boldsymbol{\eta})\|^2(\widehat{\alpha}_u(\boldsymbol{\eta})-\alpha)^2 + \|\boldsymbol{\Pi}^{\perp}_{\underline{\mathbf{a}}(\boldsymbol{\eta})}\underline{\mathbf{x}}\|^2. \tag{4.13}$$

The optimization proceeds by considering two cases based on the sign of $\widehat{\alpha}_u(\boldsymbol{\eta})$,

$$\begin{aligned}\text{if}\quad \widehat{\alpha}_u(\boldsymbol{\eta})>0 \Leftrightarrow \underline{\mathbf{a}}(\boldsymbol{\eta})^{\mathrm{T}}\underline{\mathbf{x}}>0:&\\ &\hat{\alpha}=\min\{(\alpha-\widehat{\alpha}_u(\boldsymbol{\eta}))^2\}\\ &2(\alpha-\widehat{\alpha}_u(\boldsymbol{\eta}))=0\\ &\widehat{\alpha}=\widehat{\alpha}_u(\boldsymbol{\eta}).\end{aligned} \tag{4.14}$$

Since $\widehat{\alpha}_u(\boldsymbol{\eta})$ yields positive values, which after the subtraction in the cost function produce negative contributions, the minimum of the quadratic term is achieved when $\alpha=\widehat{\alpha}_u(\boldsymbol{\eta})$ under the constraint $\alpha>0$.

$$\begin{aligned}\text{if}\quad \widehat{\alpha}_u(\boldsymbol{\eta})\leq 0 \Leftrightarrow \underline{\mathbf{a}}(\boldsymbol{\eta})^{\mathrm{T}}\underline{\mathbf{x}}\leq 0:&\\ &\hat{\alpha}=\min\{(\alpha-\widehat{\alpha}_u(\boldsymbol{\eta}))^2\}\\ &2(\alpha-\widehat{\alpha}_u(\boldsymbol{\eta}))=0\\ &\widehat{\alpha}=0.\end{aligned} \tag{4.15}$$

In this case, $\widehat{\alpha}_u(\boldsymbol{\eta})$ takes negative values which, after the subtraction operation, turn positive in the cost function. Under the constraint $\alpha\in\mathbb{R}^+$, the minimum is achieved at the boundary. However, this case implies no signal is received, as indicated by the signal model $\mathbf{x}=\alpha\mathbf{a}(\boldsymbol{\eta})+\mathbf{n}=\mathbf{n}$, representing a detection failure rather than a valid parameter estimate.

Under the assumption that signal is present and the first case in (4.14) applies, substituting $\widehat{\alpha}=\widehat{\alpha}_u(\boldsymbol{\eta})$ eliminates the first term, reducing the cost function to

$$\mathcal{S}_2(\mathbf{x};\widehat{\alpha},\boldsymbol{\eta}) = \|\boldsymbol{\Pi}^{\perp}_{\underline{\mathbf{a}}(\boldsymbol{\eta})}\underline{\mathbf{x}}\|^2. \tag{4.16}$$

Since minimizing $\|\mathbf{\Pi}^{\perp}_{\underline{\mathbf{a}}(\boldsymbol{\eta})}\underline{\mathbf{x}}\|^2$ is equivalent to maximizing $\|\mathbf{\Pi}_{\underline{\mathbf{a}}(\boldsymbol{\eta})}\underline{\mathbf{x}}\|^2$, and using the property that $\|\underline{\mathbf{x}}\|^2$ is constant

$$\widehat{\boldsymbol{\eta}} = \arg\max_{\boldsymbol{\eta}} \|\mathbf{\Pi}_{\underline{\mathbf{a}}(\boldsymbol{\eta})}\underline{\mathbf{x}}\|^2 = \arg\max_{\boldsymbol{\eta}} \frac{|\underline{\mathbf{a}}(\boldsymbol{\eta})^{\mathrm{T}}\underline{\mathbf{x}}|^2}{\|\underline{\mathbf{a}}(\boldsymbol{\eta})\|^2}. \tag{4.17}$$

Using the relationship $|\underline{\mathbf{a}}^{\mathrm{T}}\underline{\mathbf{x}}|^2 = \Re\{\mathbf{a}^{\mathrm{H}}\mathbf{x}\}^2 + \Im\{\mathbf{a}^{\mathrm{H}}\mathbf{x}\}^2$ and the constraint $\Re\{\mathbf{a}(\boldsymbol{\eta})^{\mathrm{H}}\mathbf{x}\} > 0$ ensuring $\widehat{\alpha} > 0$, the cost function simplifies to

$$\mathcal{S}_2(\mathbf{x}; \widehat{\alpha}, \boldsymbol{\eta}) = -\Re\left\{\frac{\mathbf{a}(\boldsymbol{\eta})^{\mathrm{H}}\mathbf{x}}{\|\mathbf{a}(\boldsymbol{\eta})\|}\right\}^2. \tag{4.18}$$

Therefore, the optimal estimator is obtained by maximizing

$$\widehat{\boldsymbol{\eta}}_o = \arg\max_{\boldsymbol{\eta}} \left\{\Re\left\{\frac{\mathbf{a}(\boldsymbol{\eta})^{\mathrm{H}}\mathbf{x}}{\|\mathbf{a}(\boldsymbol{\eta})\|}\right\}^2\right\}, \tag{4.19}$$

subject to the constraint $\Re\{\mathbf{a}(\boldsymbol{\eta})^{\mathrm{H}}\mathbf{x}\} > 0$.

4.4 Cramér-Rao Bound

With the signal model for perfect phase compensation established, the derivation of fundamental performance bounds becomes possible through FIM analysis, as established in (Kay 1993, §3). This section derives the CRB corresponding to the case where φ is perfectly known.

The parameter vector under perfect phase knowledge reduces to $\boldsymbol{\epsilon} = [\sigma_n^2, \alpha, \boldsymbol{\eta}^{\mathrm{T}}]^{\mathrm{T}}$ since φ is no longer an unknown parameter. The FIM is derived from

$$\mathbf{F}_{\boldsymbol{\epsilon}} = \mathrm{E}\left\{-\frac{\partial^2 \ln P(\mathbf{x}; \boldsymbol{\epsilon})}{\partial \boldsymbol{\epsilon} \partial \boldsymbol{\epsilon}^{\mathrm{T}}}\right\}, \tag{4.20}$$

where $P(\mathbf{x}; \boldsymbol{\epsilon})$ corresponds to the likelihood of the phase-compensated signal. Given the complex Gaussian nature of the signal model under study, the FIM can be derived from (2.13b). Alternatively, this section derives the FIM by reformulating the signal model in (4.1) with its real-valued equivalent and applying the SBF in (2.13a), as explained in more detail in Appendix B.1.3. The resulting FIM has a block structure

$$\mathbf{F}_{\boldsymbol{\epsilon}} = \begin{bmatrix} \frac{N'}{(\sigma_n^2)^2} & \mathbf{0}^{\mathrm{T}} \\ \mathbf{0} & \mathbf{F}_{\boldsymbol{\zeta}|\boldsymbol{\epsilon}} \end{bmatrix}, \tag{4.21}$$

and,

$$\mathbf{F}_{\boldsymbol{\zeta}|\boldsymbol{\epsilon}} = \begin{bmatrix} \mathrm{F}_{\alpha|\boldsymbol{\epsilon}} & \mathbf{F}_{\alpha,\boldsymbol{\eta}|\boldsymbol{\epsilon}} \\ \mathbf{F}_{\boldsymbol{\eta},\alpha|\boldsymbol{\epsilon}} & \mathbf{F}_{\boldsymbol{\eta}|\boldsymbol{\epsilon}} \end{bmatrix} = \frac{2}{\sigma_n^2} \begin{bmatrix} \|\underline{\mathbf{a}}(\boldsymbol{\eta})\|^2 & \alpha \underline{\mathbf{a}}(\boldsymbol{\eta})^{\mathrm{T}} \frac{\partial \underline{\mathbf{a}}(\boldsymbol{\eta})}{\partial \boldsymbol{\eta}^{\mathrm{T}}} \\ \alpha \left(\underline{\mathbf{a}}(\boldsymbol{\eta})^{\mathrm{T}} \frac{\partial \underline{\mathbf{a}}(\boldsymbol{\eta})}{\partial \boldsymbol{\eta}^{\mathrm{T}}}\right)^{\mathrm{T}} & \alpha^2 \left(\frac{\partial \underline{\mathbf{a}}(\boldsymbol{\eta})}{\partial \boldsymbol{\eta}^{\mathrm{T}}}\right)^{\mathrm{T}} \frac{\partial \underline{\mathbf{a}}(\boldsymbol{\eta})}{\partial \boldsymbol{\eta}^{\mathrm{T}}} \end{bmatrix}, \tag{4.22}$$

where $\underline{\mathbf{a}}(\boldsymbol{\eta}) = \underline{\mathbf{c}}(\boldsymbol{\eta})e^{j\psi(\boldsymbol{\eta})}$ denotes the real-valued representation of the complex steering vector

$$\underline{\mathbf{a}}(\boldsymbol{\eta}) = \begin{bmatrix} \Re\{\mathbf{a}(\boldsymbol{\eta})\} \\ \Im\{\mathbf{a}(\boldsymbol{\eta})\} \end{bmatrix} \in \mathbb{R}^{2N'}, \quad \frac{\partial \underline{\mathbf{a}}(\boldsymbol{\eta})}{\partial \boldsymbol{\eta}^{\mathrm{T}}} = \begin{bmatrix} \Re\left\{\frac{\partial \mathbf{a}(\boldsymbol{\eta})}{\partial \boldsymbol{\eta}^{\mathrm{T}}}\right\} \\ \Im\left\{\frac{\partial \mathbf{a}(\boldsymbol{\eta})}{\partial \boldsymbol{\eta}^{\mathrm{T}}}\right\} \end{bmatrix} \in \mathbb{R}^{2N'}. \tag{4.23}$$

By considering,

$$\Re\{\mathbf{A}^H\mathbf{A}\} = \Re\{\mathbf{A}\}^T\Re\{\mathbf{A}\} + \Im\{\mathbf{A}\}^T\Im\{\mathbf{A}\}, \tag{4.24}$$

the following relationships apply

$$\left(\frac{\partial \underline{\mathbf{a}}(\boldsymbol{\eta})}{\partial \boldsymbol{\eta}^{\mathrm{T}}}\right)^{\mathrm{T}} \frac{\partial \underline{\mathbf{a}}(\boldsymbol{\eta})}{\partial \boldsymbol{\eta}^{\mathrm{T}}} = \Re\left\{\frac{\partial \mathbf{a}(\boldsymbol{\eta})}{\partial \boldsymbol{\eta}^{\mathrm{T}}}\right\}^{\mathrm{T}} \Re\left\{\frac{\partial \mathbf{a}(\boldsymbol{\eta})}{\partial \boldsymbol{\eta}^{\mathrm{T}}}\right\} + \Im\left\{\frac{\partial \mathbf{a}(\boldsymbol{\eta})}{\partial \boldsymbol{\eta}^{\mathrm{T}}}\right\}^{\mathrm{T}} \Im\left\{\frac{\partial \mathbf{a}(\boldsymbol{\eta})}{\partial \boldsymbol{\eta}^{\mathrm{T}}}\right\}$$
$$= \Re\left\{\left(\frac{\partial \mathbf{a}(\boldsymbol{\eta})}{\partial \boldsymbol{\eta}^{\mathrm{T}}}\right)^{\mathrm{H}} \frac{\partial \mathbf{a}(\boldsymbol{\eta})}{\partial \boldsymbol{\eta}^{\mathrm{T}}}\right\}, \tag{4.25a}$$

$$\underline{\mathbf{a}}(\boldsymbol{\eta})^{\mathrm{T}} \frac{\partial \underline{\mathbf{a}}(\boldsymbol{\eta})}{\partial \boldsymbol{\eta}^{\mathrm{T}}} = \Re\{\mathbf{a}(\boldsymbol{\eta})\}^{\mathrm{T}} \Re\left\{\frac{\partial \mathbf{a}(\boldsymbol{\eta})}{\partial \boldsymbol{\eta}^{\mathrm{T}}}\right\} + \Im\{\mathbf{a}(\boldsymbol{\eta})\}^{\mathrm{T}} \Im\left\{\frac{\partial \mathbf{a}(\boldsymbol{\eta})}{\partial \boldsymbol{\eta}^{\mathrm{T}}}\right\}$$
$$= \Re\left\{\mathbf{a}(\boldsymbol{\eta})^{\mathrm{H}} \frac{\partial \mathbf{a}(\boldsymbol{\eta})}{\partial \boldsymbol{\eta}^{\mathrm{T}}}\right\}, \tag{4.25b}$$

which allow to rewrite (4.22) as

$$\mathbf{F}_{\boldsymbol{\zeta}|\boldsymbol{\epsilon}} = \frac{2}{\sigma_n^2}\begin{bmatrix} \|\mathbf{a}(\boldsymbol{\eta})\|^2 & \alpha\Re\left\{\mathbf{a}(\boldsymbol{\eta})^{\mathrm{H}} \frac{\partial \mathbf{a}(\boldsymbol{\eta})}{\partial \boldsymbol{\eta}^{\mathrm{T}}}\right\} \\ \alpha\Re\left\{\mathbf{a}(\boldsymbol{\eta})^{\mathrm{H}} \frac{\partial \mathbf{a}(\boldsymbol{\eta})}{\partial \boldsymbol{\eta}^{\mathrm{T}}}\right\}^{\mathrm{T}} & \alpha^2\Re\left\{\left(\frac{\partial \mathbf{a}(\boldsymbol{\eta})}{\partial \boldsymbol{\eta}^{\mathrm{T}}}\right)^{\mathrm{H}} \frac{\partial \mathbf{a}(\boldsymbol{\eta})}{\partial \boldsymbol{\eta}^{\mathrm{T}}}\right\} \end{bmatrix} = \frac{2}{\sigma_n^2}\mathbf{\Phi}_{\mathrm{op}}(\boldsymbol{\eta}), \tag{4.26}$$

where the subscript "op" designates the optimal phase compensation approach that is being analyzed. The CRB for the parameter vector $\boldsymbol{\eta}$ is directly obtained by inverting $\mathbf{F}_{\boldsymbol{\zeta}|\boldsymbol{\epsilon}}$ by blocks (Seber 2008, §15), as detailed in Appendix B.2. This is,

$$\mathbf{CRB}_{\boldsymbol{\eta}|\boldsymbol{\epsilon}} = \frac{\sigma_n^2}{2}\left[\mathbf{F}_{\boldsymbol{\eta}|\boldsymbol{\epsilon}} - \mathbf{F}_{\boldsymbol{\eta},\alpha|\boldsymbol{\epsilon}}\mathbf{F}_{\alpha|\boldsymbol{\epsilon}}^{-1}\mathbf{F}_{\alpha,\boldsymbol{\eta}|\boldsymbol{\epsilon}}\right]^{-1} = \frac{\sigma_n^2}{2\alpha^2}\left[\mathbf{\Phi}_{\mathrm{op}}(\boldsymbol{\eta})\right]^{-1}, \tag{4.27}$$

with

$$\mathbf{\Phi}_{\mathrm{op}}(\boldsymbol{\eta}) = \Re\left\{\left(\frac{\partial \mathbf{a}(\boldsymbol{\eta})}{\partial \boldsymbol{\eta}^{\mathrm{T}}}\right)^{\mathrm{H}} \frac{\partial \mathbf{a}(\boldsymbol{\eta})}{\partial \boldsymbol{\eta}^{\mathrm{T}}}\right\} - \frac{\Re\left\{\mathbf{a}(\boldsymbol{\eta})^{\mathrm{H}} \frac{\partial \mathbf{a}(\boldsymbol{\eta})}{\partial \boldsymbol{\eta}^{\mathrm{T}}}\right\}^{\mathrm{T}} \Re\left\{\mathbf{a}(\boldsymbol{\eta})^{\mathrm{H}} \frac{\partial \mathbf{a}(\boldsymbol{\eta})}{\partial \boldsymbol{\eta}^{\mathrm{T}}}\right\}}{\|\mathbf{a}(\boldsymbol{\eta})\|^2}. \tag{4.28}$$

Compared to the conventional FIM expression in equation (3.29), where

$$\mathbf{\Phi}_{\mathrm{co}}(\boldsymbol{\eta}) = \Re\left\{\left(\frac{\partial \mathbf{a}(\boldsymbol{\eta})}{\partial \boldsymbol{\eta}^{\mathrm{T}}}\right)^{\mathrm{H}} \frac{\partial \mathbf{a}(\boldsymbol{\eta})}{\partial \boldsymbol{\eta}^{\mathrm{T}}}\right\}$$
$$- \frac{\Re\{\mathbf{a}(\boldsymbol{\eta})^H \frac{\partial \mathbf{a}(\boldsymbol{\eta})}{\partial \eta^{\mathrm{T}}}\}^{\mathrm{T}} \Re\{\mathbf{a}(\boldsymbol{\eta})^H \frac{\partial \mathbf{a}(\boldsymbol{\eta})}{\partial \boldsymbol{\eta}^{\mathrm{T}}}\}}{\|\mathbf{a}(\boldsymbol{\eta})\|^2}$$
$$- \frac{\Im\{\mathbf{a}(\boldsymbol{\eta})^H \frac{\partial \mathbf{a}(\boldsymbol{\eta})}{\partial \eta^{\mathrm{T}}}\}^{\mathrm{T}} \Im\{\mathbf{a}(\boldsymbol{\eta})^H \frac{\partial \mathbf{a}(\boldsymbol{\eta})}{\partial \boldsymbol{\eta}^{\mathrm{T}}}\}}{\|\mathbf{a}(\boldsymbol{\eta})\|^2},$$

$\mathbf{\Phi}_{\mathrm{op}}(\boldsymbol{\eta})$ in equation (4.28) is missing the imaginary terms containing the product between $\mathbf{a}(\boldsymbol{\eta})$ and $\frac{\partial \mathbf{a}(\boldsymbol{\eta})}{\partial \boldsymbol{\eta}}$. The complex phase term $e^{j\phi}$, which appeared after the decomposition in phase and magnitude of the complex amplitude α' discussed in Section 3.5.2, causes that its SBF implementation yields an imaginary results for the crossed-terms derivatives, similar to the situation in equation (B.9). However, in this case φ is assumed perfectly know and compensated, thus removing its associated SBF terms from the FIM.

4.4.1 Closed-form expressions

Closed-form expressions provide analytical solutions expressed through elementary functions and finite algebraic operations, enabling direct evaluation without numerical methods or iterative procedures. For the FIM term in (4.28), closed-form expressions are derived following the analytical framework of (Das 2020b; Lubeigt 2020; Medina 2020), where the baseband signal products are

expressed in matrix form to systematically derive the terms populating (4.28). This matrix representation provides a more comprehensive notion of the contributions from carrier-phase, baseband signal structure, and Doppler effects, revealing how each component influences the achievable estimation accuracy. The following subsections present these closed-form expressions for different model assumptions considered for equation (4.1), i.e. the wide-band, narrow-band, and delay-only scenarios.

To facilitate time-derivative computations, the continuous-time signal model representation from (3.3) is employed in the following sections, thanks to the band-limited assumption and the Nyquist-Shannon theorem, with its discrete-time equivalent given in (3.6) and (3.7).

Wide-band assumption

Under the wide-band assumption described in Section 3.4.2, the derivative term in (4.28) is expressed as,

$$\frac{\partial a(t;\boldsymbol{\eta})}{\partial \boldsymbol{\eta}} = \begin{pmatrix} \frac{\partial a(t;\boldsymbol{\eta})}{\partial \tau} \\ \frac{\partial a(t;\boldsymbol{\eta})}{\partial b} \end{pmatrix} = - \begin{pmatrix} (1-b)\dot{c}(t;\boldsymbol{\eta}) + jw_c(1-b)c(t;\boldsymbol{\eta}) \\ \frac{\partial c(t;\boldsymbol{\eta})}{\partial b} + jw_c(t-\tau)c(t;\boldsymbol{\eta}) \end{pmatrix} e^{j\psi(t;\boldsymbol{\eta})}, \tag{4.29}$$

where $\dot{c}(t;\boldsymbol{\eta}) \equiv \frac{\partial c(t;\boldsymbol{\eta})}{\partial \tau}$. Note that, in the conventional CSM (3.20) case where $\psi(t;\boldsymbol{\eta}) = b(t-\tau)$, such derivative yields

$$\frac{\partial a(t;\boldsymbol{\eta})}{\partial \boldsymbol{\eta}} = \begin{pmatrix} \frac{\partial a(t;\boldsymbol{\eta})}{\partial \tau} \\ \frac{\partial a(t;\boldsymbol{\eta})}{\partial b} \end{pmatrix} = - \begin{pmatrix} (1-b)\dot{c}(t;\boldsymbol{\eta}) - jw_c\, b\, c(t;\boldsymbol{\eta}) \\ \frac{\partial c(t;\boldsymbol{\eta})}{\partial b} + jw_c(t-\tau)c(t;\boldsymbol{\eta}) \end{pmatrix} e^{j\psi(t;\boldsymbol{\eta})}. \tag{4.30}$$

Comparing equation (4.29) against equation (4.29) shows that the key difference lies in the contribution of the additional carrier-phase term $e^{j\omega_c\tau}$. The derivative $\frac{\partial a(t;\boldsymbol{\eta})}{\partial \tau}$ in equation (4.29) contains the term $jw_c(1-b)c(t;\boldsymbol{\eta})$ rather than just $jw_c b\, c(t;\boldsymbol{\eta})$. This distinction is significant, since the Doppler parameter typically satisfies $b \ll 1$ (Sec. 3.4.2), which would reduce the contribution when multiplied by ω_c. In the case of equation (4.29), the factor $(1-b) \approx 1$ preserves the full magnitude of the carrier frequency contribution. Consequently, the term $\omega_c(1-b)$ introduces the complete carrier frequency influence into the FIM, becoming a dominant contribution in most practical systems. For instance, for the GPS L1 C/A signal where $\omega_c = 2\pi f_c$ with $f_c = 1575.42$ MHz, this carrier-phase term has a strong implication in estimation performance due to the large magnitude of ω_c.

The partial derivative $\frac{\partial c(t;\boldsymbol{\eta})}{\partial b} = \frac{\partial c((t-\tau)(1-b))}{\partial b}$ can be further derived via the chain rule by defining

$$f(b) = s\left(u(b)\right), \tag{4.31}$$
$$u(b) = \left((t-\tau)(1-b)\right). \tag{4.32}$$

Applying the chain rule yields

$$\frac{\partial f}{\partial b} = \frac{ds}{du}\frac{du}{db} = -\frac{ds}{du}(t-\tau), \tag{4.33}$$

which can be expressed as a derivative with respect to t by applying the chain rule again

$$\frac{ds}{dt} = \frac{ds}{du}\frac{du}{dt} = \frac{ds}{du}(1-b) \Rightarrow \frac{ds}{du} = \frac{ds}{dt}\frac{1}{(1-b)}. \tag{4.34}$$

Therefore, (4.32) becomes,

$$\frac{\partial f}{\partial b} = -\frac{ds}{du}(t-\tau), \tag{4.35}$$

which yields

$$\frac{\partial c((t-\tau)(1-b))}{\partial b} = -\frac{(t-\tau)}{(1-b)}\frac{\partial c((t-\tau)(1-b))}{\partial t}. \tag{4.36}$$

This result allows to express equation (4.29) in matrix form as,

$$\frac{\partial a(t;\boldsymbol{\eta})}{\partial \boldsymbol{\eta}} = -\mathbf{Q}\mathbf{v}(t-\boldsymbol{\eta})e^{-j\psi(t;\boldsymbol{\eta})}, \tag{4.37}$$

where

$$\mathbf{Q} = \begin{bmatrix} jw_c(1-b) & 0 & (1-b) & 0 \\ 0 & jw_c & 0 & 1 \end{bmatrix}, \quad \mathbf{v}(t-\boldsymbol{\eta}) = \begin{bmatrix} c(t;\boldsymbol{\eta}) \\ (t-\tau)c(t;\boldsymbol{\eta}) \\ \dot{c}(t;\boldsymbol{\eta}) \\ (t-\tau)\dot{c}(t;\boldsymbol{\eta}) \end{bmatrix}. \tag{4.38}$$

By applying the Nyquist-Shannon equivalence as in equations (3.33), the derivative products in equation (4.29) can be expressed similarly to equation (3.33) as,

$$\left(\frac{\partial \mathbf{a}(\boldsymbol{\eta})}{\partial \boldsymbol{\eta}^{\mathrm{T}}}\right)^{\mathrm{H}} \frac{\partial \mathbf{a}(\boldsymbol{\eta})}{\partial \boldsymbol{\eta}^{\mathrm{T}}} = f_s \mathbf{Q}\mathbf{W}\mathbf{Q}^{\mathrm{H}}, \quad \mathbf{a}(\boldsymbol{\eta})^{\mathrm{H}} \frac{\partial \mathbf{a}(\boldsymbol{\eta})}{\partial \boldsymbol{\eta}^{\mathrm{T}}} = -f_s \left(\mathbf{Q}\mathbf{w}\right)^{\mathrm{T}}, \tag{4.39a}$$

except that, in this case, $\mathbf{W}$ and $\mathbf{w}$ are

$$\mathbf{w} = \begin{bmatrix} w_1 \\ w_2 \\ w_3 \\ w_4 \end{bmatrix}, \quad \mathbf{W} = \begin{bmatrix} w_1 & w_2^* & w_3^* & w_4^* \\ w_2 & W_{2,2} & w_4^* & W_{4,2}^* \\ w_3 & w_4 & W_{3,3} & W_{4,3}^* \\ w_4 & W_{4,2} & W_{4,3} & W_{4,4} \end{bmatrix}. \tag{4.40}$$

where the individual elements from $\mathbf{W}$ and $\mathbf{w}$ are derived in (B.3). Under this formulation, the CRB in equation (4.27) becomes,

$$\mathbf{CRB}_{\boldsymbol{\eta}|\boldsymbol{\epsilon}} = \frac{\sigma_n^2}{2\alpha^2 f_s}\left[\boldsymbol{\Phi}_{\mathrm{op}}(\boldsymbol{\eta})\right]^{-1} \tag{4.41}$$

$$= \frac{\sigma_n^2}{2\alpha^2 f_s}\left[\Re\left\{\mathbf{Q}\mathbf{W}\mathbf{Q}^{\mathrm{H}}\right\} - \frac{\Re\left\{\mathbf{Q}\mathbf{w}\right\}\Re\left\{\mathbf{Q}\mathbf{w}\right\}^{\mathrm{T}}}{w_1}\right]^{-1} \tag{4.42}$$

The matrix Q used to compute the terms in the CRB is different from that of the state of the art. Comparing $\boldsymbol{\Phi}_{\mathrm{op}}(\boldsymbol{\eta})$ to $\boldsymbol{\Phi}_{\mathrm{co}}(\boldsymbol{\eta})$ from (3.36) reveals two key structural differences: the absence of the subtractive imaginary term $\frac{\Im\{\mathbf{Q}\mathbf{w}\}\Im\{\mathbf{Q}\mathbf{w}\}^{\mathrm{T}}}{w_1}$ and the substitution of b by $(1-b)$ in the top-left element of matrix $\mathbf{Q}$.

By unpacking the terms in $\mathbf{Q}$ and $\mathbf{w}$, a more explicit representation of the CRB is obtained. The FIM in (4.27) is a 2×2 matrix that can be decomposed as,

$$\mathbf{F}_{\boldsymbol{\eta}|\boldsymbol{\epsilon}}(\boldsymbol{\epsilon}) = \frac{2f_s\alpha^2}{\sigma_n^2}\begin{bmatrix} \Phi_{1,1} & \Phi_{1,2} \\ \Phi_{1,2}^{\mathrm{T}} & \Phi_{2,2} \end{bmatrix}, \tag{4.43}$$

where the elements are given by

$$\Phi_{1,1} = (1-b)^2\left(\mathrm{Re}\{W_{3,3}\} + \omega_c^2 w_1 + 2\omega_c \mathrm{Im}\{w_3\} - \frac{\mathrm{Re}\{w_3\}^2}{w_1}\right),$$

$$\Phi_{2,2} = \omega_c^2\mathrm{Re}\{W_{2,2}\} + \omega_c^2\frac{\mathrm{Im}\{w_2\}^2}{w_1} - 2\omega_c\mathrm{Im}\{W_{4,2}\} + \mathrm{Re}\{W_{4,4}\} + 2\omega_c\frac{\mathrm{Re}\{w_4\}\mathrm{Im}\{w_2\}}{w_1} - \frac{\mathrm{Re}\{w_4\}^2}{w_1},$$

$$\Phi_{1,2} = (1-b)\left(\omega_c^2\mathrm{Re}\{w_2\} + 2\omega_c\mathrm{Im}\{w_4\} + \mathrm{Re}\{W_{4,3}\} + \omega_c\frac{\mathrm{Re}\{w_3\}\mathrm{Im}\{w_2^*\}}{w_1} - \frac{\mathrm{Re}\{w_3 w_4^*\}}{w_1}\right).$$

The wide-band formulation reveals the structure of the FIM through explicit expressions involving the signal correlation matrices $\mathbf{W}$ and vector $\mathbf{w}$. The element $\Phi_{1,1}$ contains the dominant carrier frequency contribution $\omega_c^2 w_1$ scaled by $(1-b)^2 \approx 1$, representing the primary information source for time-delay estimation. The element $\Phi_{2,2}$ incorporates terms involving $W_{4,4}$ and cross-products with w_4, which arise from the time-derivative terms in the wide-band signal model and provide additional information for Doppler estimation. The cross-coupling element $\Phi_{1,2}$ exhibits a complex structure involving mixed terms, reflecting the correlation between time-delay and Doppler parameters in the presence of signal time dilation and compression effects.

Narrow-band assumption

The closed-form CRB expression under the narrow-band assumption follows an analogous derivation process to that presented in Section 3.5.2. The signal model is redefined, which modifies the previously introduced matrices $\mathbf{Q}$ and v, and consequently affects the matrices $\mathbf{W}$ and vector $\mathbf{w}$. These terms are replaced by their narrow-band counterparts and used identically in the parameters of interest given in (5.4.2). Under the narrow-band assumption, the derivative term becomes,

$$\frac{\partial a(t;\boldsymbol{\eta})}{\partial \boldsymbol{\eta}} = \begin{pmatrix} \frac{\partial a(t;\boldsymbol{\eta})}{\partial \tau} \\ \frac{\partial a(t;\boldsymbol{\eta})}{\partial b} \end{pmatrix} = - \begin{pmatrix} \dot{c}(t-\tau) + jw_c(1-b)c(t-\tau) \\ jw_c(t-\tau)c(t-\tau) \end{pmatrix} e^{-j\psi(t;\boldsymbol{\eta})}, \tag{4.45}$$

This expression can again be written in matrix form as,

$$\frac{\partial a(t;\boldsymbol{\eta})}{\partial \boldsymbol{\eta}} = -\mathbf{Q}'\mathbf{v}'(t-\tau)e^{-j\psi(t;\boldsymbol{\eta})}, \tag{4.46}$$

where

$$\mathbf{Q}' = \begin{bmatrix} jw_c(1-b) & 0 & 1 \\ 0 & jw_c & 0 \end{bmatrix}, \quad \mathbf{v}'(t-\tau) = \begin{bmatrix} c(t-\tau) \\ (t-\tau)c(t-\tau) \\ \dot{c}(t-\tau) \end{bmatrix}. \tag{4.47a}$$

The matrix $\mathbf{Q}'$ can be directly compared with the corresponding matrix derived from the conventional CSM in (Medina 2020, §11), showing that the presence of the factor $(1-b)$ is the key structural difference between the phase-compensated and conventional narrow-band formulations.

In this case, $\mathbf{W}$ and $\mathbf{w}$ from the closed-form representation in (4.39) become $\mathbf{W}'$ and $\mathbf{w}'$, with

$$\mathbf{W}' = \begin{bmatrix} w_1 & w_2^* & w_3^* \\ w_2 & W_{2,2} & w_4^* \\ w_3 & w_4 & W_{3,3} \end{bmatrix}, \quad \mathbf{w}' = \begin{bmatrix} w_1 \\ w_2 \\ w_3 \end{bmatrix}. \tag{4.47b}$$

The elements in $\mathbf{W}'$ and $\mathbf{w}'$ have the same definitions as those in equation (4.40). The CRB terms for the narrow-band case is that of

$$\mathrm{CRB}_{\boldsymbol{\eta}|\boldsymbol{\epsilon}} = \frac{\sigma_n^2}{2\alpha^2 f_s} \left(\Re\left\{ \mathbf{Q}'\mathbf{W}'\mathbf{Q}'^{\mathrm{H}} \right\} - \frac{\Re\left\{\mathbf{Q}'\mathbf{w}'\right\} \Re\left\{\mathbf{Q}'\mathbf{w}'\right\}^{\mathrm{T}}}{w_1} \right)^{-1}. \tag{4.48}$$

By unpacking the terms in $\mathbf{Q}'$ and $\mathbf{w}'$, the explicit representation of the narrow-band FIM is obtained. The FIM can be decomposed as in (4.43), where the elements are given by

$$\Phi_{1,1} = W_{3,3} + \mathrm{Re}\{w_1\}(1-b)^2\omega_c^2 - \frac{\mathrm{Re}\{w_3\}^2}{w_1} + \mathrm{Im}\{w_3\}(1-b)2\omega_c, \tag{4.49a}$$

$$\Phi_{2,2} = W_{2,2}\omega_c^2 - \frac{\mathrm{Im}\{w_2\}^2}{w_1}\omega_c^2, \tag{4.49b}$$

$$\Phi_{1,2} = \mathrm{Re}\{w_2\}(1-b)\omega_c^2 - \frac{\mathrm{Re}\{w_3\}\mathrm{Im}\{w_2\}}{w_1}\omega_c - \mathrm{Im}\{w_4^*\}\omega_c. \tag{4.49c}$$

The narrow-band formulation exhibits a simpler structure compared to the wide-band case in quation (4.44). The element $\Phi_{2,2}$ lacks the additional terms involving $W_{4,4}$ and cross-products with w_4 that appear in the wide-band formulation, as these terms arise from the time-derivative components associated with signal time dilation effects. Similarly, $\Phi_{1,2}$ contains fewer mixed terms, reflecting the reduced complexity of the narrow-band signal model where time dilation and compression effects are neglected.

Compared to the conventional formulation in equation (3.36), the crossed terms maintain non-zero values even for real-valued baseband signals through the carrier-phase contribution $\omega_c^2 \mathrm{Re}\{w_2\}$ in $\Phi_{1,2}$. This coupling between time-delay and Doppler parameters introduces a performance penalty for joint estimation, as discussed in Section 4.6.3.

Delay-only narrowband assumption

Under the delay-only narrow-band assumption, $\boldsymbol{\eta} = \tau$, and the derivative term

$$\frac{\partial a(t;\tau)}{\partial \tau} = -\left(\ \dot{c}(t-\tau) + jw_c c(t-\tau) \ \right) e^{-jw_c\tau}. \tag{4.50}$$

This expression can again be formulated as,

$$\frac{\partial a(t;\tau)}{\partial \tau} = -\mathbf{Q}''\mathbf{v}''(t-\tau)e^{-jw_c\tau}. \tag{4.51}$$

where,

$$\mathbf{Q}'' = \begin{bmatrix} jw_c & 1 \end{bmatrix}, \quad \mathbf{v}''(t-\tau) = \begin{bmatrix} c(t-\tau) \\ \dot{c}(t-\tau) \end{bmatrix}. \tag{4.52a}$$

with,

$$\mathbf{W}'' = \begin{bmatrix} w_1 & w_3^* \\ w_3 & W_{3,3} \end{bmatrix}, \quad \mathbf{w}'' = \begin{bmatrix} w_1 \\ w_3 \end{bmatrix}. \tag{4.53}$$

Consequently, the CRB becomes,

$$\mathrm{CRB}_{\tau|\boldsymbol{\epsilon}} = \frac{\sigma_n^2}{2\alpha^2 f_s} \left(\Re\left\{ \mathbf{Q}''\mathbf{W}''\mathbf{Q}''^{\mathrm{H}} \right\} - \frac{\Re\left\{\mathbf{Q}''\mathbf{w}''\right\} \Re\left\{\mathbf{Q}''\mathbf{w}''\right\}^{\mathrm{T}}}{w_1} \right)^{-1}. \tag{4.54}$$

In this case, the explicit FIM expression is,

$$\Phi_\tau = f_s \left(W_{3,3} - \frac{\mathrm{Re}\{w_3\}^2}{w_1} + w_c^2 w_1 + 2w_c \mathrm{Im}\{w_3\} \right). \tag{4.55}$$

The carrier frequency contribution $w_c^2 w_1 + 2w_c \mathrm{Im}\{w_3\}$ represents the dominant information source for time-delay estimation, consistent with the structure observed in $\Phi_{1,1}$ for the joint estimation case in (4.49). Since the parameter vector reduces to the scalar $\boldsymbol{\eta} = \tau$, the FIM becomes a scalar quantity rather than a 2×2 matrix, eliminating the cross-coupling terms $\Phi_{1,2}$ that appear in the joint time-delay and Doppler estimation framework.

4.5 Ambiguity Function Analysis

Since the MLE in equation (4.1) seeks to maximize the projection of the received signal onto the steering vector $\mathbf{a}(\boldsymbol{\eta})$, the AF characterizes this function in the absence of noise. Under high SNR condition, the discrete-time AF becomes,

$$\Xi(\boldsymbol{\eta}';\boldsymbol{\eta}) = (\alpha^0)^2 \frac{\Re\left\{\mathbf{a}(\boldsymbol{\eta}')^{\mathrm{H}}\mathbf{a}(\boldsymbol{\eta})\right\}^2}{\Re\left\{\|\mathbf{a}(\boldsymbol{\eta}')\|^2\right\}} = (\alpha^0)^2 \|\mathbf{a}(\boldsymbol{\eta})\|^2 \Re\left\{ \frac{\mathbf{a}(\boldsymbol{\eta}')^{\mathrm{H}}\mathbf{a}(\boldsymbol{\eta})}{\|\mathbf{a}(\boldsymbol{\eta}')\|\|\mathbf{a}(\boldsymbol{\eta})\|} \right\}^2, \tag{4.56}$$

where $\boldsymbol{\eta}' = \boldsymbol{\eta} + d\boldsymbol{\eta}$ repressents an offset version from the true $\boldsymbol{\eta}$ value.

For the delay-only case where $\eta = \tau$ and $\tau' = \tau + d\tau$, expanding the signal model structure yields

$$\Xi(\tau';\tau) = (\alpha^0)^2 \|\mathbf{c}(\tau)\|^2 \Re\left\{ \frac{\mathbf{c}(\tau')^{\mathrm{H}}\mathbf{c}(\tau)}{\|\mathbf{c}(\tau')\|\|\mathbf{c}(\tau)\|} e^{j(\psi(\tau)-\psi(\tau'))} \right\}^2. \tag{4.57}$$

Considering,

$$\psi(\tau) - \psi(\tau') = -\omega_c\tau - (-\omega_c(\tau + d\tau)) = \omega_c d\tau = -\frac{\partial\psi(\tau)}{\partial\tau} d\tau, \tag{4.58}$$

equation (4.57) becomes,

$$\Xi(\tau';\tau) = \Xi_0(\tau';\tau)\cos^2\left(-\frac{\partial\psi(\tau)}{\partial\tau} d\tau\right), \tag{4.59}$$

where the AF for the conventional signal model in equation (3.14) is,

$$\Xi_0(\tau';\tau) = (\alpha^0)^2 \left| \frac{\mathbf{c}(\tau')^{\mathrm{H}}\mathbf{c}(\tau)}{\|\mathbf{c}(\tau')\|} \right|^2. \tag{4.60}$$

Note that, $\frac{\partial\psi(\tau)}{\partial\tau} = -\omega_c$ produces a cosine-squared modulation that creates a comb structure with lobe spacing $\Delta\tau = \frac{\pi}{\omega_c} = \frac{1}{2f_c}$.

The complete AF therefore consists of the baseband signal AF modulated by a cosine function with frequency f_c. This creates a Dirac comb sampling effect on the baseband AF, with the $\cos^2$ term forming a rapidly oscillating envelope with lobe spacing $\Delta\tau = \frac{\pi}{\omega_c} = \frac{1}{2f_c}$. For GPS L1 ($f_c = 1575.42$ MHz), this yields approximately 0.32 nanoseconds between lobes.

The phase-induced modulation creates amplitude variations between the main lobe and secondary lobes. For correct MLE identification of the main lobe, this amplitude difference must exceed the noise floor. Figure 4.1 provides a simplified illustration of this principle: while not representing the actual correlation process, it demonstrates how signal structure becomes masked under noisy conditions. In this didactic visualization, a carrier signal $e^{j\omega_c\tau}$ is shown with high ($\sigma_n = 1$) and low ($\sigma_n = 0.1$) noise levels, analogous to how the fine comb structure in the AF becomes indistinguishable when noise exceeds the modulation-induced amplitude variations. Below a defined SNR threshold, noise masks the fine comb structure of $\Xi(\tau';\tau)$, causing random selection among adjacent lobes and creating the plateau behavior observed in the CRB analysis. As SNR increases, the estimation error becomes confined to the main lobe, restoring the MLE efficiency property where it achieves the CRB. This mechanism explains the transition from plateau to asymptotic performance regions identified in the theoretical bounds.

Both AFs $\Xi(\tau';\tau)$ and $\Xi_0(\tau';\tau)$ structures are illustrated in Figures 4.6, for various sampling frequency ($\mathrm{F_s}$) and carrier frequency ($\mathrm{F_c}$) scaling factors, that is, multiples of the base sampling and carrier-frequency values. The sampling frequency $\mathrm{F_s}$ primarily determines the resolution and affects quantization, as higher sampling rates increase the probability of capturing samples closer to the correlation peak maximum (maximum of the maximorum). The carrier frequency $\mathrm{F_c}$ determines the lobe width: as $\mathrm{F_c}$ increases, the individual lobes become narrower while the baseband component Ξ_0 becomes flatter and more spread around zero amplitude.

4.5.1 Connection to Cramér-Rao Bound

The AF second derivative relates directly to the FIM in (4.28). Through Taylor expansion around the true parameter value of the AF in (4.56),

$$\Xi(\boldsymbol{\eta}';\boldsymbol{\eta}) \simeq \Xi(\boldsymbol{\eta};\boldsymbol{\eta}) + \frac{1}{2} d\boldsymbol{\eta}^{\mathrm{T}} \left.\frac{\partial^2\Xi(\boldsymbol{\eta}';\boldsymbol{\eta})}{\partial\boldsymbol{\eta}'\partial\boldsymbol{\eta}'}^{\mathrm{T}}\right|_{\boldsymbol{\eta}} d\boldsymbol{\eta}. \tag{4.61}$$

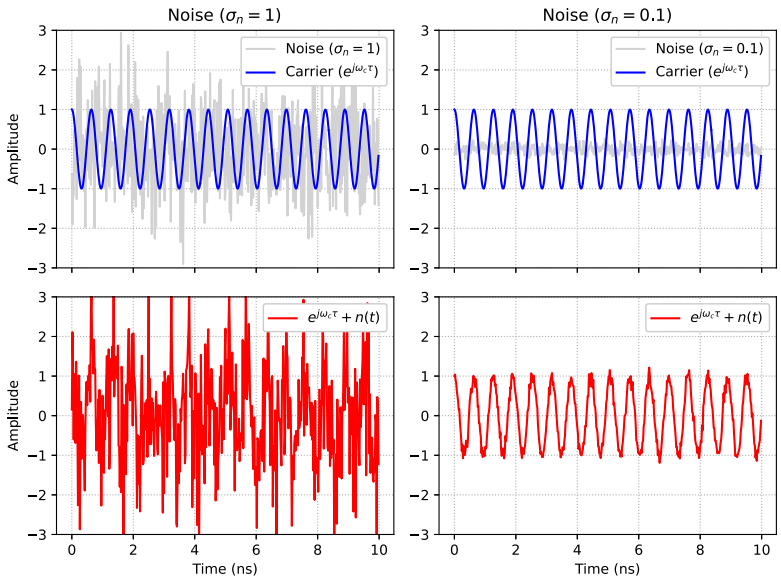

Figure 4.1: Didactic illustration of signal structure degradation under different noise conditions. Top row: carrier signal $e^{j\omega_c\tau}$ with (left) high noise $\sigma_n = 1$ and (right) low noise $\sigma_n = 0.1$. Bottom row: corresponding noisy signals showing how noise masks the underlying carrier structure, where $n(t) \sim N(0, \sigma_n^2)$. This simplified visualization demonstrates the principle of SNR-dependent signal detection but does not represent the actual correlation process or ambiguity function structure.

where the first-order term vanishes at the maximum. At the true parameter value, the AF achieves its maximum

$$\Xi(\boldsymbol{\eta}; \boldsymbol{\eta}) = \alpha^2 \|\underline{\mathbf{a}}(\boldsymbol{\eta})\|^2. \tag{4.62}$$

where the real-valued representation in (4.6) was employed. To derive the second-order derivative, starting from the definition,

$$\Xi(\boldsymbol{\eta}'; \boldsymbol{\eta}) = \alpha^2 \underline{\mathbf{a}}(\boldsymbol{\eta})^{\mathrm{T}} \boldsymbol{\Pi}_{\underline{\mathbf{a}}(\boldsymbol{\eta}')} \underline{\mathbf{a}}(\boldsymbol{\eta}) \tag{4.63}$$

the first derivative is,

$$\frac{\partial \Xi(\boldsymbol{\eta}'; \boldsymbol{\eta})}{\partial \boldsymbol{\eta}_p} = \alpha^2 \underline{\mathbf{a}}(\boldsymbol{\eta})^{\mathrm{T}} \frac{\partial \boldsymbol{\Pi}_{\underline{\mathbf{a}}(\boldsymbol{\eta}')}}{\partial \boldsymbol{\eta}_p} \underline{\mathbf{a}}(\boldsymbol{\eta}). \tag{4.64}$$

Since $\boldsymbol{\Pi}_{\underline{\mathbf{a}}(\boldsymbol{\eta}')} = \frac{\underline{\mathbf{a}}(\boldsymbol{\eta}')\underline{\mathbf{a}}(\boldsymbol{\eta}')^{\mathrm{T}}}{\underline{\mathbf{a}}(\boldsymbol{\eta}')^{\mathrm{T}}\underline{\mathbf{a}}(\boldsymbol{\eta}')}$ and using $\boldsymbol{\Pi}^{\perp}_{\underline{\mathbf{a}}(\boldsymbol{\eta}')} = \mathbf{I} - \boldsymbol{\Pi}_{\underline{\mathbf{a}}(\boldsymbol{\eta}')}$ then,

$$\frac{\partial \Xi(\boldsymbol{\eta}'; \boldsymbol{\eta})}{\partial \boldsymbol{\eta}_p} = -\alpha^2 \underline{\mathbf{a}}(\boldsymbol{\eta})^{\mathrm{T}} \frac{\partial \boldsymbol{\Pi}^{\perp}_{\underline{\mathbf{a}}(\boldsymbol{\eta}')}}{\partial \boldsymbol{\eta}_p} \underline{\mathbf{a}}(\boldsymbol{\eta}). \tag{4.65}$$

The second derivative,

$$\frac{\partial^2 \Xi(\boldsymbol{\eta}'; \boldsymbol{\eta})}{\partial \boldsymbol{\eta}_p \partial \boldsymbol{\eta}_{p'}} = -\alpha^2 \underline{\mathbf{a}}(\boldsymbol{\eta})^{\mathrm{T}} \frac{\partial^2 \boldsymbol{\Pi}^{\perp}_{\underline{\mathbf{a}}(\boldsymbol{\eta}')}}{\partial \boldsymbol{\eta}_p \partial \boldsymbol{\eta}_{p'}} \underline{\mathbf{a}}(\boldsymbol{\eta}), \tag{4.66}$$

can be manipulated algebraically considering $\boldsymbol{\Pi}^{\perp}_{\underline{\mathbf{a}}(\boldsymbol{\eta}')} = \boldsymbol{\Pi}^{\perp}_{\underline{\mathbf{a}}(\boldsymbol{\eta}')} \boldsymbol{\Pi}^{\perp}_{\underline{\mathbf{a}}(\boldsymbol{\eta}')}$, and

$$\frac{\partial^2 \boldsymbol{\Pi}^{\perp}_{\underline{\mathbf{a}}(\boldsymbol{\eta}')}}{\partial \boldsymbol{\eta}_p \partial \boldsymbol{\eta}_{p'}} = \frac{\partial \boldsymbol{\Pi}^{\perp}_{\underline{\mathbf{a}}(\boldsymbol{\eta}')}}{\partial \boldsymbol{\eta}_{p'}} \frac{\partial \boldsymbol{\Pi}^{\perp}_{\underline{\mathbf{a}}(\boldsymbol{\eta}')}}{\partial \boldsymbol{\eta}_p} + \frac{\partial \boldsymbol{\Pi}^{\perp}_{\underline{\mathbf{a}}(\boldsymbol{\eta}')}}{\partial \boldsymbol{\eta}_p} \frac{\partial \boldsymbol{\Pi}^{\perp}_{\underline{\mathbf{a}}(\boldsymbol{\eta}')}}{\partial \boldsymbol{\eta}_{p'}} + \boldsymbol{\Pi}^{\perp}_{\underline{\mathbf{a}}(\boldsymbol{\eta}')} \frac{\partial^2 \boldsymbol{\Pi}^{\perp}_{\underline{\mathbf{a}}(\boldsymbol{\eta}')}}{\partial \boldsymbol{\eta}_{p'} \partial \boldsymbol{\eta}_p} + \frac{\partial^2 \boldsymbol{\Pi}^{\perp}_{\underline{\mathbf{a}}(\boldsymbol{\eta}')}}{\partial \boldsymbol{\eta}_p \partial \boldsymbol{\eta}_{p'}} \boldsymbol{\Pi}^{\perp}_{\underline{\mathbf{a}}(\boldsymbol{\eta}')}, \tag{4.67}$$

where, at $\boldsymbol{\eta}' = \boldsymbol{\eta}$, since $\boldsymbol{\Pi}^{\perp}_{\underline{\mathbf{a}}(\boldsymbol{\eta})} \underline{\mathbf{a}}(\boldsymbol{\eta}) = \mathbf{0}$, the last two terms in (4.67) vanish

$$\left. \frac{\partial^2 \Xi(\boldsymbol{\eta}'; \boldsymbol{\eta})}{\partial \boldsymbol{\eta}_p \partial \boldsymbol{\eta}_{p'}} \right|_{\boldsymbol{\eta}} = -2\alpha^2 \left(\frac{\partial \boldsymbol{\Pi}^{\perp}_{\underline{\mathbf{a}}(\boldsymbol{\eta})}}{\partial \boldsymbol{\eta}_p} \underline{\mathbf{a}}(\boldsymbol{\eta}) \right)^{\mathrm{T}} \left(\frac{\partial \boldsymbol{\Pi}^{\perp}_{\underline{\mathbf{a}}(\boldsymbol{\eta})}}{\partial \boldsymbol{\eta}_{p'}} \underline{\mathbf{a}}(\boldsymbol{\eta}) \right), \tag{4.68}$$

and differentiation yields

$$\frac{\partial \boldsymbol{\Pi}^{\perp}_{\underline{\mathbf{a}}(\boldsymbol{\eta}')}}{\partial \boldsymbol{\eta}_p}\underline{\mathbf{a}}(\boldsymbol{\eta}') + \boldsymbol{\Pi}^{\perp}_{\underline{\mathbf{a}}(\boldsymbol{\eta}')}\frac{\partial \underline{\mathbf{a}}(\boldsymbol{\eta}')}{\partial \boldsymbol{\eta}_p} = \mathbf{0} \Rightarrow \frac{\partial \boldsymbol{\Pi}^{\perp}_{\underline{\mathbf{a}}(\boldsymbol{\eta}')}}{\partial \boldsymbol{\eta}_p}\underline{\mathbf{a}}(\boldsymbol{\eta}') = -\boldsymbol{\Pi}^{\perp}_{\underline{\mathbf{a}}(\boldsymbol{\eta}')}\frac{\partial \underline{\mathbf{a}}(\boldsymbol{\eta}')}{\partial \boldsymbol{\eta}_p}, \tag{4.69}$$

which helps rewrite (4.68) as,

$$\left.\frac{\partial^2 \Xi(\boldsymbol{\eta}';\boldsymbol{\eta})}{\partial \boldsymbol{\eta}_p \partial \boldsymbol{\eta}_{p'}}\right|_{\boldsymbol{\eta}} = -2\alpha^2 \frac{\partial \underline{\mathbf{a}}(\boldsymbol{\eta})}{\partial \boldsymbol{\eta}_p}^{\mathrm{T}} \boldsymbol{\Pi}^{\perp}_{\underline{\mathbf{a}}(\boldsymbol{\eta})}\frac{\partial \underline{\mathbf{a}}(\boldsymbol{\eta})}{\partial \boldsymbol{\eta}_{p'}}. \tag{4.70}$$

Finally, (4.66) becomes

$$\left.\frac{\partial^2 \Xi(\boldsymbol{\eta}';\boldsymbol{\eta})}{\partial \boldsymbol{\eta}' \partial \boldsymbol{\eta}'}^{\mathrm{T}}\right|_{\boldsymbol{\eta}} = -2\alpha^2 \frac{\partial \underline{\mathbf{a}}(\boldsymbol{\eta})}{\partial \boldsymbol{\eta}^{\mathrm{T}}}^{\mathrm{T}} \boldsymbol{\Pi}^{\perp}_{\underline{\mathbf{a}}(\boldsymbol{\eta})}\frac{\partial \underline{\mathbf{a}}(\boldsymbol{\eta})}{\partial \boldsymbol{\eta}^{\mathrm{T}}} = -2\alpha^2 \boldsymbol{\Phi}(\boldsymbol{\eta}), \tag{4.71}$$

where $\boldsymbol{\Phi}(\boldsymbol{\eta})$ is the matrix defined in equation (4.28). Substituting back into the Taylor expansion in equation (4.61)

$$\Xi(\boldsymbol{\eta}';\boldsymbol{\eta}) \simeq \alpha^2 \|\mathbf{a}(\boldsymbol{\eta})\|^2 - \alpha^2 d\boldsymbol{\eta}^{\mathrm{T}} \boldsymbol{\Phi}(\boldsymbol{\eta}) d\boldsymbol{\eta}, \tag{4.72}$$

which can be rewritten as,

$$\Xi(\boldsymbol{\eta}';\boldsymbol{\eta}) \simeq \alpha^2 \|\mathbf{a}(\boldsymbol{\eta})\|^2 \left(1 - d\boldsymbol{\eta}^{\mathrm{T}} \left(\frac{\boldsymbol{\Phi}(\boldsymbol{\eta})}{\|\mathbf{a}(\boldsymbol{\eta})\|^2}\right) d\boldsymbol{\eta}\right). \tag{4.73}$$

This establishes

$$\mathbf{F}_{\boldsymbol{\eta}|\boldsymbol{\epsilon}} = \frac{2\alpha^2}{\sigma_n^2}\boldsymbol{\Phi}(\boldsymbol{\eta}) = \frac{-1}{\sigma_n^2}\left.\frac{\partial^2 \Xi(\boldsymbol{\eta}';\boldsymbol{\eta})}{\partial \boldsymbol{\eta}' \partial \boldsymbol{\eta}'}^{\mathrm{T}}\right|_{\boldsymbol{\eta}}, \tag{4.74}$$

and therefore

$$\mathrm{CRB}_{\boldsymbol{\eta}|\boldsymbol{\epsilon}} = \mathbf{F}^{-1}_{\boldsymbol{\eta}|\boldsymbol{\epsilon}} = -\sigma_n^2 \left(\left.\frac{\partial^2 \Xi(\boldsymbol{\eta}';\boldsymbol{\eta})}{\partial \boldsymbol{\eta}' \partial \boldsymbol{\eta}'}^{\mathrm{T}}\right|_{\boldsymbol{\eta}}\right)^{-1}. \tag{4.75}$$

This connection matches the definition of the FIM, in which the curvature of the ambiguity function at the true parameter value $\boldsymbol{\eta}$ directly determines the Fisher information and consequently the CRB derived in equation (4.42).

4.6 Simulation Results and Discussion

This section presents numerical results that validate the theoretical framework developed in the preceding sections and reveal fundamental characteristics of carrier-phase information in TDE assessments under perfect phase compensation conditions. The methodology is designed to systematically evaluate both the mathematical correctness of the derived expressions and their practical utility under realistic operating conditions. The simulations employ the narrow-band signal model from Section 4.4.1, as this formulation enables efficient Monte Carlo evaluation while preserving the essential carrier-phase enhancement effects through the $\omega_c \tau$ term.

4.6.1 Test Signal Configurations

Two representative code sequences are employed to validate the framework across distinct application domains and frequency regimes:

- **GPS L1 C/A Signal:** A 1,023-chip periodic Gold sequence with BPSK modulation, chipping frequency of 1.023 MHz, carrier frequency $f_c = 1,575.42$ MHz, baseband sampling frequency $f_s = 4$ MHz, and 1 ms integration time. This configuration represents high-frequency navigation applications where carrier-phase effects are pronounced.
- **Kasami Code:** A 15-bit sequence with 15 kHz chipping frequency, 1.5 MHz carrier frequency, and 30 kHz baseband sampling frequency. This shorter sequence enables detailed analysis of estimation dynamics while representing lower-frequency communication systems with different phase sensitivity characteristics.

These configurations span different frequency regimes and sequence lengths, providing comprehensive validation of the theoretical predictions across diverse system parameters. The selection ensures that the derived bounds and estimators demonstrate generality beyond specific application constraints.

4.6.2 CRB Variants and Theoretical Benchmarks

The performance analysis employs three distinct CRB formulations to characterize different aspects of the estimation problem:

- CRB^m (Medina 2020): The conventional CRB (3.27) from Sec. 3.5.2, derived by absorbing the hardware-related phase term φ into the signal amplitude, yielding a simplified signal model that provides more straightforward expressions. This approach represents traditional TDE methods where phase information is not explicitly utilized.
- CRB^o (Bernabeu 2024a): The theoretical lower bound derived in Sec. 4.4, specified for wide-band (4.42), narrow-band (4.48) and delay-only (4.54) scenarios, that analyzes optimal estimation performance by assuming the phase term φ to be completely compensated.

4.6.3 Estimation Performance Characteristics

The Monte Carlo simulations presented in Figure 4.2 demonstrate five distinct operational regions in the MLE performance. Two more than what was known in the state of the art from the conventional model. At low SNR values (Region I), the estimator exhibits high variance without convergent behavior. As SNR increases, the RMSE decreases exponentially toward the conventional bound CRB^m (Region II), stabilizing at this level in Region III. Before the transition to Region IV, a slight MSE increase appears when the MLE begins to distinguish the fine comb structure within the code envelope but fails to consistently select the correct peak corresponding to the main lobe. This temporary degradation occurs because the estimator becomes sensitive to the carrier-phase structure before reliably discriminating between adjacent lobes separated by $\Delta\tau = 1/(2f_c)$. For the test configurations used, this effect is only visible in the GPS L1 C/A signal due to its carrier frequency and code structure. The transition then occurs in Region IV, where the estimator resolves the ambiguity and begins converging toward the optimal bound CRB^o, ultimately achieving this theoretical limit in Region V.

The performance improvement between conventional and optimal bounds shown in figure 4.2 is substantial, measuring approximately 20 dB for the Kasami configuration and 24.5 dB for GPS L1 C/A. At 50 dB of SNR_{out}, the Kasami sequence achieves 0.7 cm ranging accuracy under perfect phase compensation compared to 18.5 meters using conventional methods. Similarly, GPS L1 C/A demonstrates 1 mm accuracy versus 2.8 cm for the conventional approach. These results confirm the orders-of-magnitude improvement predicted by the theoretical analysis in Section 4.4. This

behavior is directly linked to the additional carrier frequency terms $\omega_c^2 w_1 + 2\omega_c \mathrm{Im}\{w_3\}$ appearing in $\Phi_{1,1}$ of the narrow-band FIM in (4.49), which are absent in the conventional formulation. These terms, scaled by $(1-b)^2 \approx 1$, introduce the dominant contribution of the carrier frequency ω_c to the estimation performance, enabling the substantial accuracy improvements observed in Regions IV and V.

Comparison between delay-only and delay-doppler Models

This section examines the performance degradation introduced when Doppler effects cannot be compensated and must be jointly estimated with the time-delay parameter. The comparison quantifies the cost of including Doppler as an unknown parameter versus scenarios where it can be neglected or independently compensated.

Figure 4.3 presents simulation results comparing under the narrowband delay-doppler (3.4.2) and delay-only (3.4.2) asumptions, whose CRBs where derived in Section 4.4.1 and Section 4.4.1, respectively. The simulation results reveal consistent performance penalties when Doppler remains uncompensated. The CRB for the delay-doppler case, denoted $\mathrm{CRB}^{o\prime}_{\tau|\boldsymbol{\eta}}$ and displayed with dot markers, shows a constant 6 dB rightward $\mathrm{SNR}_{\mathrm{out}}$ shift compared to the delay-only bound $\mathrm{CRB}^{o}_{\tau|\boldsymbol{\epsilon}}$ across the entire $\mathrm{SNR}_{\mathrm{out}}$ range. This degradation persists regardless of signal power, indicating a fundamental limitation imposed by parameter coupling discussed in Section 4.4.1. Both MLEs exhibit similar convergence characteristics. The delay-only estimator $\widehat{\tau}_o$ converges to $\mathrm{CRB}^{o}_{\tau|\boldsymbol{\epsilon}}$, while the delay-doppler estimator $\widehat{\tau}'$ converges to $\mathrm{CRB}^{o\prime}_{\tau|\boldsymbol{\epsilon}}$ at the same $\mathrm{SNR}_{\mathrm{out}}$ threshold but at 4 dB higher RMSE level.

The Doppler parameter estimation exhibits similar coupling effects. Figure 4.4 shows the Doppler estimation performance, where the estimator $\hat{b}$ converges to $\mathrm{CRB}^{o}_{b|\epsilon}$ with approximately 10 dB $\mathrm{SNR}_{\mathrm{out}}$ loss relative to the conventional bound $\mathrm{CRB}^{m}_{b|\epsilon}$ across the entire $\mathrm{SNR}_{\mathrm{out}}$ range. This degradation occurs because the conventional formulation in equation (3.36) exhibits diagonal FIM structure for the real-valued signals employed in the testing setup, with off-diagonal coupling terms vanishing due to $\Im\{w_4 - \frac{w_2 w_3}{w_1}\} = 0$. In contrast, the optimal compensation formulation in equation (4.49) maintains non-zero off-diagonal terms through the carrier-phase contribution $\omega_c^2 \mathrm{Re}\{w_2\}$ in $\Phi_{1,2}$, creating statistical coupling between time-delay and Doppler parameters.

These results establish clear design trade-offs for ranging systems employing carrier-phase information. When system architecture permits Doppler pre-estimation through dedicated pilot sequences or when platform dynamics are negligible over the observation interval, the delay-only model provides superior ranging accuracy with 6 dB $\mathrm{SNR}_{\mathrm{out}}$ improvement. Applications requiring single-shot joint estimation must accept this performance penalty as the cost of simultaneous parameter estimation. Nevertheless, the achieved accuracy under joint estimation still significantly exceeds conventional approaches that absorb carrier-phase into complex amplitude, maintaining the fundamental advantage of carrier-phase exploitation despite the additional parameter coupling.

4.6.4 Sampling and Carrier Frequency Dependencies

Figure 4.5a shows that increasing the sampling frequency scalar multiplier from $\mathrm{F_s} = 2$ to $\mathrm{F_s} = 10$ shifts the convergence threshold to lower $\mathrm{SNR}_{\mathrm{out}}$ values, enabling earlier achievement of optimal performance. The conventional bound CRB^{m} improves with higher sampling rates, while CRB^{o} remains invariant, confirming that carrier-phase information content is independent of sampling density above the Nyquist rate.

The carrier frequency analysis in Figure 4.5b reveals that increasing the carrier-frequency multiplier $\mathrm{F_c}$ from 10 to 30 improves the optimal bound by reducing the AF lobe width according to $\Delta\tau = 1/(2f_c)$. However, this improvement comes at the cost of requiring higher $\mathrm{SNR}_{\mathrm{out}}$ values

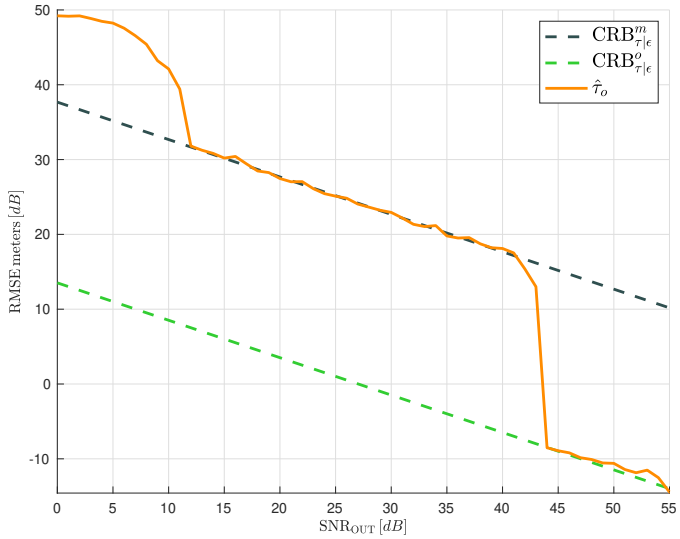

(**a**)

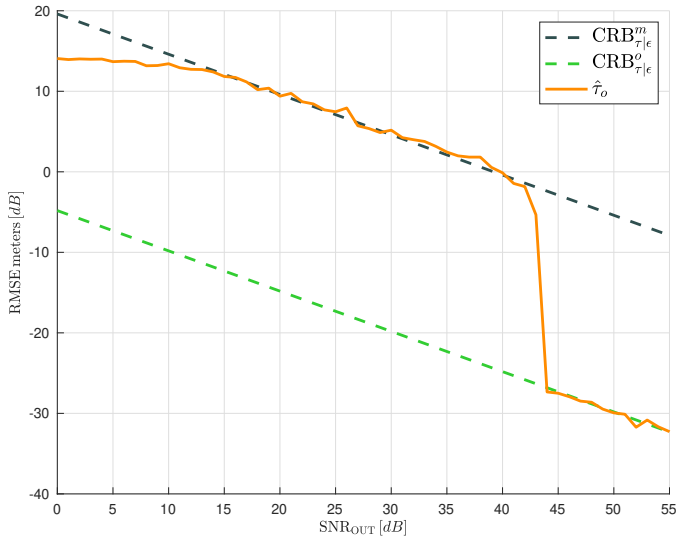

(**b**)

Figure 4.2: (a) Simulation using a Kasami code sequence. There is around a 20dB difference between bounds. For instance at 50dB of SNR_{out}, the conventional bound shows a distance accuracy, after converting to linear RMSE, of 18.5 meters, whilst the one leveraging phase observables 0.7cm. (b) Simulation using a GPS L1/CA Gold code. There is around a 24.5dB difference, where the conventional bound shows a distance accuracy of 2.8cm, whilst the one leveraging phase observables 1mm. The difference between the initial tendency of the MLE in (b) compared to (a) is only due to a code simplification where the search space in of the MLE was reduced to a defined range of 20 GPS L1 C/A codes instead of the full 1023 sequence, to reduce the computational burden of the simulation. Otherwise, the MLE's tendency of arbitrary MSE would have been the same as with the shorter Kasami sequence in (a).

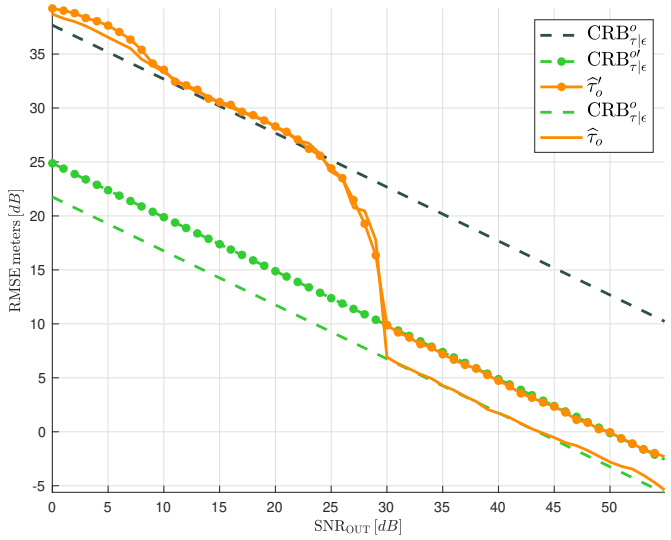

(**a**)

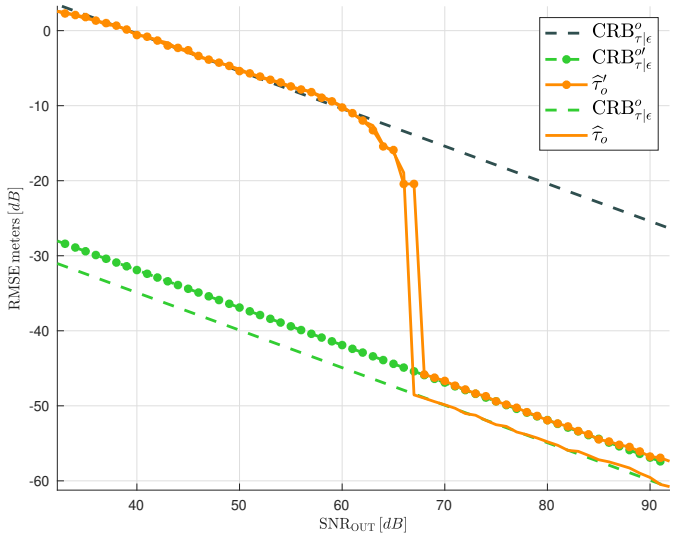

(**b**)

Figure 4.3: Comparison of time-delay estimation performance under perfect phase compensation for delay-only and delay-doppler signal models using (a) Kasami sequence and (b) GPS L1 C/A signal configurations. The delay-doppler model (dot markers) shows $\widehat{\tau}'$ converging to $\text{CRB}^{o\prime}_{\tau|\boldsymbol{\epsilon}}$ with 4 dB RMSE degradation compared to the delay-only model (solid lines) where $\widehat{\tau}_o$ converges to $\text{CRB}^{o}_{\tau|\boldsymbol{\epsilon}}$. The consistent performance gap of around 6 dB SNR_{out} across both signal configurations confirms that the cost of Doppler uncertainty is independent of the specific ranging signal employed.

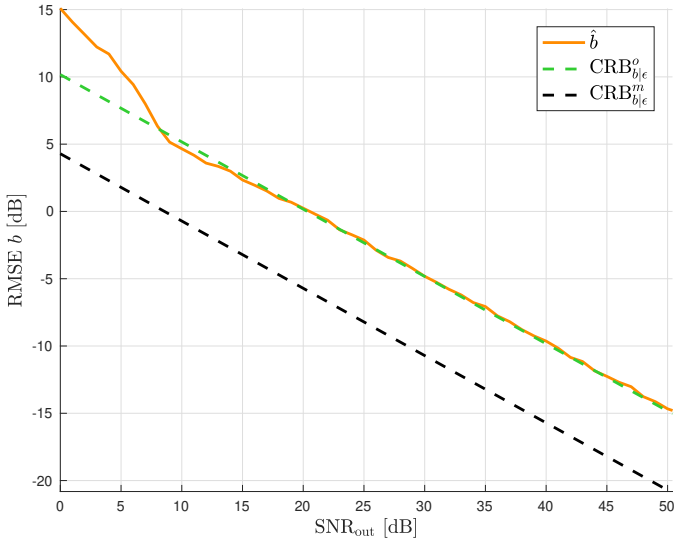

Figure 4.4: Doppler parameter b estimation performance under optimal phase compensation showing approximately 12 dB SNR$_{\text{out}}$ degradation. The estimator $\hat{b}$ converges to CRB$^{o}_{b|\epsilon}$, which is 6 dB higher in Root-Mean-Squared Error (RMSE) than the conventional bound CRB$^{m}_{b|\epsilon}$ due to parameter coupling introduced by the additional carrier-phase term $\omega_c\tau$ in the signal model.

to achieve convergence, as the denser lobe structure becomes more susceptible to noise-induced ambiguities. This result is closely related to the analysis of the AF, as explained in the next section.

4.6.5 Ambiguity Function Analysis

The AF structure shown in Figure 4.6 confirms the theoretical predictions from Section 4.5. The complete AF $\Xi(\tau';\tau)$ exhibits the characteristic comb structure arising from the cosine-squared modulation of the baseband component $\Xi_0(\tau';\tau)$. The individual lobes, clearly visible in Figure 4.6a, act as a Dirac comb that samples the underlying baseband AF at intervals of $\Delta\tau = 1/(2f_c)$.

The comparison between Figures 4.6a and 4.6b demonstrates the direct impact of carrier frequency on lobe structure. The tenfold increase in $\mathrm{F_c}$ produces proportionally narrower lobes, with the observation window in Figure 4.6b containing significantly more lobes despite covering a narrower delay range (-0.1 to 0.1) compared to the three lobes visible in the zoomed region of Figure 4.6a. This densification of the lobe structure enhances timing discrimination capability by providing finer delay resolution.

The relationship between lobe width and estimation performance is directly reflected in the results of Figure 4.5b. Higher carrier frequencies produce narrower lobes that enable improved RMSE performance at the optimal bound, consistent with the reduced lobe spacing. However, the denser lobe structure requires higher SNR$_{\text{out}}$ values to resolve unambiguously, explaining why the convergence point shifts toward stronger signal conditions as $\mathrm{F_c}$ increases. This fundamental tradeoff between ultimate accuracy and the signal strength required to achieve it emerges directly from the AF structure, where narrower lobes provide finer discrimination but become more susceptible to noise-induced ambiguity between adjacent peaks.

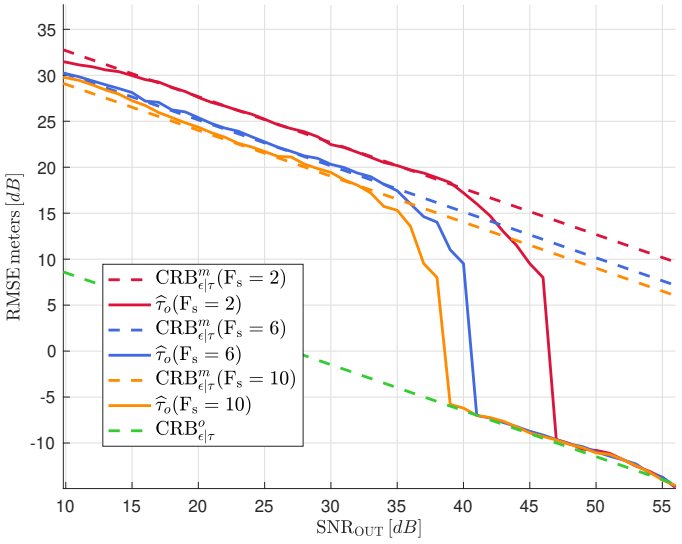

(**a**)

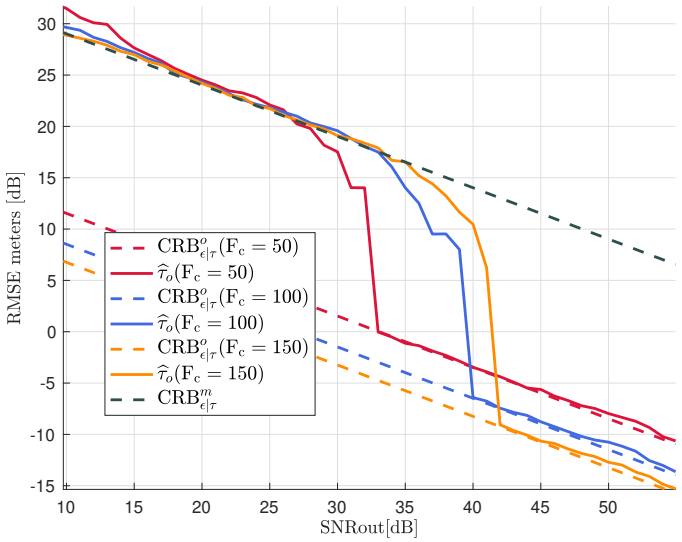

(**b**)

Figure 4.5: Impact of sampling and carrier frequency on estimation performance using a Kasami code sequence. (a) Carrier frequency $\mathrm{F_c} = 100$ with varying sampling frequencies $\mathrm{F_s} \in \{2, 6, 10\}$. Higher sampling rates shift the convergence threshold to lower $\mathrm{SNR_{out}}$ values while improving the conventional bound CRB^m but leaving CRB^o unchanged. (b) Sampling frequency $\mathrm{F_s} = 2$ with varying carrier frequencies $\mathrm{F_c} \in \{50, 100, 150\}$. Increased carrier frequencies improve the optimal bound CRB^o through narrower AF lobes but require higher $\mathrm{SNR_{out}}$ values for convergence, demonstrating the fundamental tradeoff between ultimate accuracy and signal strength requirements.

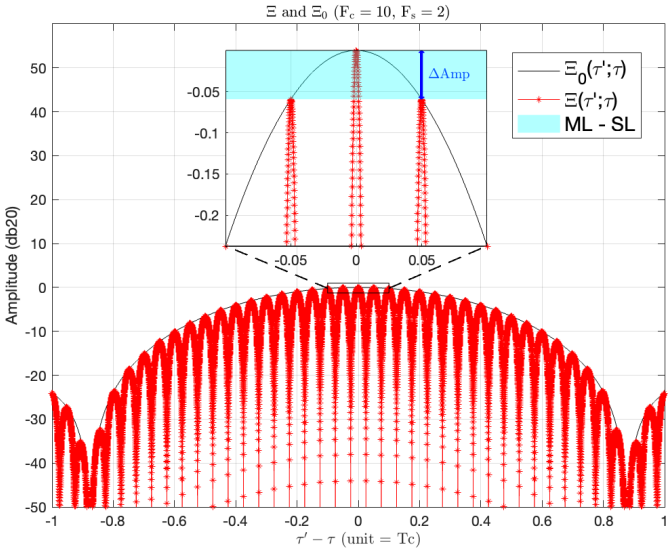

(**a**)

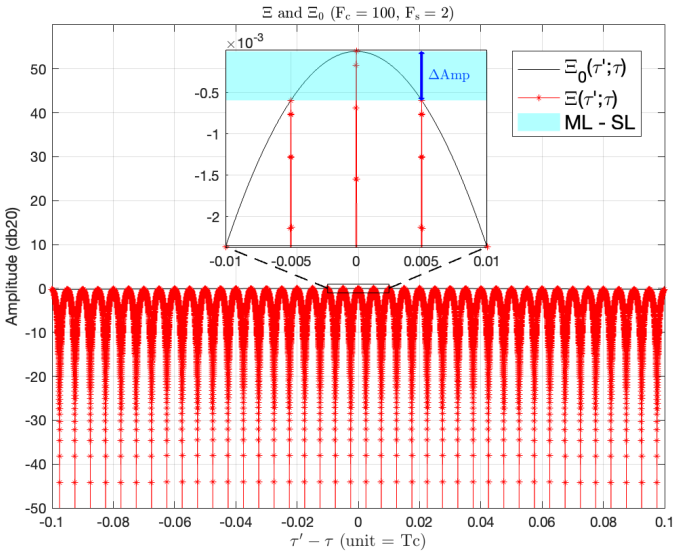

(**b**)

Figure 4.6: Ambiguity function structure for different sampling and carrier frequency parameters. (a) $F_s = 2$, $F_c = 10$: displays the complete ambiguity function with three distinct lobes visible in the zoomed region. (b) $F_s = 2$, $F_c = 100$: shows a narrower delay range (-0.1 to 0.1) containing significantly more lobes due to the higher carrier frequency. The sampling frequency F_s determines the resolution of the ambiguity function structure through the discrete sampling of the analytic signal. Higher sampling rates increase the probability of capturing samples near the correlation peak maximum, reducing quantization effects. The carrier frequency F_c determines the spacing of the Dirac comb structure, with lobe spacing $\Delta\tau = 1/(2f_c)$ as established in equation (4.59). The tenfold increase in F_c between (a) and (b) produces proportionally denser lobe spacing, demonstrating the direct relationship between carrier frequency and timing discrimination capability.

4.7 Conclusion

This chapter established the theoretical framework for time-delay estimation under optimal phase compensation, assuming complete knowledge and removal of hardware-induced phase offsets from the received signal. Three interconnected components were developed: a signal model formulation using real-valued amplitude, contrasting with the complex-valued amplitude of the conventional approach; a constrained MLE that explicitly utilizes carrier-phase information through $\psi(\boldsymbol{\eta})$; and CRB expressions that quantify the optimal achievable estimation performance. The closed-form CRB expressions derived for wide-band, narrow-band, and delay-only scenarios reveal how baseband signal structure, carrier frequency, and Doppler effects jointly determine estimation accuracy. The AF analysis demonstrates that carrier-phase information creates a characteristic comb structure with lobe spacing $\Delta\tau = 1/(2f_c)$. The second derivative of this structure directly determines the FIM and establishes the link to the CRB. Monte Carlo simulations validate the theoretical derivations and quantify the performance improvement relative to conventional approaches. The optimal bound demonstrates gains of 20-25 dB in RMSE across different signal configurations. These results translate to centimeter or millimeter-level ranging accuracy, meeting NOIRE's sub-centimeter requirement, compared to decimeter or meter-level performance when carrier-phase is absorbed into complex amplitude. The identified SNR_{out} threshold of approximately 45 dB separates regimes where carrier-phase exploitation is effective from those where noise masks the fine AF structure. Below this threshold, noise-induced ambiguities between adjacent lobes prevent the estimator from exploiting carrier-phase information, causing convergence to the conventional bound. Above this threshold, estimation errors become confined to the main lobe, enabling achievement of the optimal bound. Joint estimation of time-delay and Doppler parameters incurs a $\approx$4 dB penalty in RMSE, representing the cost of parameter coupling in the FIM. System design implications emerge from the interplay between carrier frequency, sampling rate, and convergence threshold. Higher carrier frequencies improve the optimal bound but require stronger SNR conditions for convergence. Increased sampling rates shift convergence thresholds to lower SNR_{out} values while improving conventional bounds, though optimal bounds remain invariant. The improvement exhibits non-linear behavior with gains diminishing as sampling frequency increases, indicating saturation beyond a threshold where further oversampling provides negligible enhancement. The optimal phase compensation scenario analyzed represents an idealization not achievable in practice. However, it defines the theoretical performance limit for carrier-phase enhanced time-delay estimation and serves to analyze realistic scenarios where phase knowledge is imperfect.

Chapter 5

Time-Delay Estimation with Phase Uncertainty

5.1 Introduction

The preceding chapter presented the theoretical framework for time-delay estimation under perfect phase compensation, demonstrating the performance gains achievable when hardware-induced phase offsets are completely eliminated. This idealized scenario, while providing essential theoretical benchmarks, represents a limiting case rarely encountered in practical implementations. The present chapter extends this framework to address the more realistic scenario where phase information is available through auxiliary measurements but contains quantifiable uncertainty.

The transition from perfect to partial phase knowledge fundamentally alters the estimation problem structure. Where Chapter 4 demonstrated that complete phase compensation yields the tightest theoretical bounds through the elimination of φ from the parameter space, practical systems must contend with phase measurements corrupted by calibration errors, thermal noise, and environmental variations. These imperfections, characterized by the variance $\sigma_{n_a}^2$, necessitate a reformulation that explicitly accounts for phase observation quality.

This chapter develops three distinct estimation approaches that span the continuum from computationally simple to statistically optimal. The naive estimator directly applies available phase measurements without accounting for their statistical properties, the phase-aware estimator incorporates the full statistical characterization of phase uncertainty into the optimization framework, and the limiting case of perfect compensation serves as a theoretical benchmark. Through systematic analysis of these estimators and their associated performance bounds, the framework quantifies precisely when sophisticated phase-aware processing justifies its computational complexity over simpler approaches. The theoretical developments presented in this chapter build upon the framework established in (Bernabeu 2024a; Bernabeu 2024b; Bernabeu 2025).

The chapter is organized as follows. Section 5.2 formulates the extended CSM incorporating auxiliary phase observables with quantifiable uncertainty. Section 5.3 derives the MLE under phase uncertainty, presenting both the naive estimator in Section 5.3 and the statistically optimal phase-aware estimator in Section 5.3.3. Section 5.4 develops the corresponding CRB expressions, with edge case analysis in Section 5.4.1 demonstrating convergence to both conventional and optimal bounds as limiting cases. Section 5.5 presents simulation results that validate the theoretical predictions and characterize the operational regimes where phase-aware processing provides tangible benefits over simpler implementations.

5.2 CSM for Time-Delay Estimation including available phase observables

The identifiability analysis presented in Section 3.6.1 established that both hardware-induced phase φ and propagation-dependent phase $\psi(\boldsymbol{\eta})$ components can be uniquely determined from observations when the signal structure satisfies the non-collinearity condition in equation (3.44). This theoretical result supports the explicit treatment of phase components as separable parameters rather than absorbed nuisance terms, motivating the incorporation of auxiliary phase measurements into the estimation framework.

The conventional treatment, as discussed in Section 3.5, absorbs the unknown hardware phase and time-delay term into a redefined complex amplitude parameter, effectively discarding potentially valuable phase information. However, the established identifiability conditions reveal that when calibration procedures or reference measurements provide noisy observations of φ, this information can be systematically incorporated to enhance parameter estimation performance.

The extended signal model incorporating phase observables takes the form

$$\begin{cases} \mathbf{x} &= \alpha\mathbf{c}(\boldsymbol{\eta})e^{j(\varphi+\psi(\boldsymbol{\eta}))} + \mathbf{n}, & \mathbf{n} \sim \mathcal{CN}\left(\mathbf{0}, \sigma_n^2\mathbf{I}_N\right) \\ x_a &= \varphi + n_a, & n_a \sim \mathcal{N}\left(0, \sigma_{n_a}^2\right) \end{cases}, \quad \alpha \in \mathbb{R}^+, \tag{5.1}$$

where $\psi(\boldsymbol{\eta})$ (3.14) varies its form depending on the assumptions in Section 3.4.2. The auxiliary phase measurement x_a can be interpreted as the output of the MLE algorithm during the calibration stage, where the carrier phase φ is estimated and n_a represents the associated estimation error. The Gaussian approximation for x_a remains valid provided $\sigma_{n_a} \ll \pi$, ensuring that phase wrapping effects at $\pm\pi$ are negligible and the linear error model adequately represents the circular nature of phase observables. For larger phase uncertainties where this condition is violated, circular distributions such as the Vom Mises distribution would be required, as discussed in Section 6.2.5.

The joint PDF of the observed quantities becomes,

$$P(\mathbf{x}, x_a; \boldsymbol{\epsilon}) = P(\mathbf{x}; \boldsymbol{\epsilon})P(x_a; \varphi),\ \boldsymbol{\epsilon} = [\sigma_n^2, \boldsymbol{\zeta}]^{\mathrm{T}},\ \boldsymbol{\zeta}^{\mathrm{T}} = [\alpha, \boldsymbol{\theta}^{\mathrm{T}}],\ \boldsymbol{\theta}^{\mathrm{T}} = [\varphi, \boldsymbol{\eta}^{\mathrm{T}}], \tag{5.2}$$

The practical relevance of this formulation manifests through two limiting cases that connect to the frameworks established in previous chapters:

• When $\sigma_{n_a}^2 \to 0$, the phase measurement becomes exact, yielding $x_a = \varphi$. This scenario corresponds to the perfect compensation framework analyzed in Chapter 4, where

$$\mathbf{x} \ \to\ \mathbf{x}e^{-j\varphi} = \alpha\mathbf{c}(\boldsymbol{\eta})e^{j\psi(\boldsymbol{\eta}))} + \mathbf{n},\ \mathbf{n} \sim \mathcal{CN}\left(\mathbf{0}, \sigma_n^2\mathbf{I}_N\right),\ \alpha \in \mathbb{R}^+. \tag{5.3a}$$

• When $\sigma_{n_a}^2 \to \infty$, the phase measurement provides no information, and the model reduces to the conventional formulation from Section 3.5

$$\mathbf{x} = \tilde{\alpha}\mathbf{c}(\boldsymbol{\eta})e^{j\psi(\boldsymbol{\eta}))} + \mathbf{n},\ \mathbf{n} \sim \mathcal{CN}\left(\mathbf{0}, \sigma_n^2\mathbf{I}_N\right),\ \tilde{\alpha} \in \mathbb{C} \tag{5.3b}$$

where $\tilde{\alpha} = \alpha e^{j\varphi}$ absorbs the unknown phase into the complex amplitude.

The relationship between phase uncertainty and estimation performance emerges through the dependence of φ estimation accuracy on the propagation phase term $\psi(\boldsymbol{\eta})$). This coupling implies that the hardware phase may not correspond to the minimum mean-squared error phase estimate, an observation that explains the prevalence of joint phase-delay formulations in practical systems as noted in (Medina 2020, §20.10).

For practical implementation, the continuous-time formulation requires discretization. Sam-

pling $N' = N_2' - N_1' + 1$ observations from the extended model yields

$$\mathbf{x} = \alpha \mathbf{c}(\boldsymbol{\eta}) e^{j\phi} + \mathbf{n},\ \mathbf{x} = \begin{pmatrix} x(N_1' \mathrm{T_s}) \\ \vdots \\ x(N_2' \mathrm{T_s}) \end{pmatrix},\ \mathbf{n} = \begin{pmatrix} n(N_1' \mathrm{T_s}) \\ \vdots \\ n(N_2' \mathrm{T_s}) \end{pmatrix}, \tag{5.4}$$

where the discrete steering vector becomes,

$$\mathbf{c}(\boldsymbol{\eta}) = \begin{pmatrix} c(N_1' \mathrm{T_s}; \boldsymbol{\eta}) e^{j\psi(N_1' \mathrm{T_s}; \boldsymbol{\eta})} \\ \vdots \\ c(N_2' \mathrm{T_s}; \boldsymbol{\eta}) e^{j\psi(N_2' \mathrm{T_s}; \boldsymbol{\eta})} \end{pmatrix}, \tag{5.5}$$

with $\mathbf{n} \sim \mathcal{CN}(0, \sigma_n^2 \mathbf{I}_{N'})$ and sampling period $\mathrm{T_s} = 1/\mathrm{F_s}$ where $f_s \geq B$. The discrete formulation preserves the limiting behaviors described in equations (5.3a) and (5.3b), enabling its direct use in digital implementation.

5.3 Maximum-Likelihood Estimator

The theoretical bounds established in the preceding sections provide performance benchmarks against which practical estimators must be evaluated. This section derives a phase-aware MLE that explicitly incorporates the auxiliary phase observable x_a and its associated uncertainty $\sigma_{n_a}^2$. Two reference implementations frame this development: the optimal estimator from Chapter 4 assuming perfect phase knowledge, and a naive implementation that directly applies phase measurements without statistical consideration.

The relationship between these estimators sheds light to the conditions under which sophisticated statistical processing provides tangible benefits over simpler implementations.

5.3.1 Constrained Maximum Likelihood Framework

To derive the phase-aware estimator, the joint probability density function introduced in equation (5.2) serves as the starting point. The log-likelihood cost function reads

$$\mathcal{S}_0(\mathbf{x}, x_a; \boldsymbol{\epsilon}) = \frac{\|\mathbf{x} - \mathbf{a}(\boldsymbol{\eta}) e^{j\varphi} \alpha\|^2}{\sigma_n^2} + N \ln(\pi \sigma_n^2) + \frac{(x_a - \varphi)^2}{2\sigma_{n_a}^2} + \frac{1}{2} \ln(2\pi \sigma_{n_a}^2). \tag{5.6}$$

The nuisance parameters σ_n^2 and α must be eliminated through their maximum likelihood estimates. For σ_n^2, setting the derivative with respect to σ_n^2 to zero yields

$$\widehat{\sigma_n^2} = \frac{\|\mathbf{x} - \mathbf{a}(\boldsymbol{\eta}) e^{j\varphi} \alpha\|^2}{N}. \tag{5.7}$$

Substituting this estimate back into $\mathcal{S}_0$ produces

$$\begin{aligned} \mathcal{S}_1(\mathbf{x}, x_a; \boldsymbol{\eta}, \varphi, \alpha) &= N + N \ln\left(\frac{\pi \|\mathbf{x} - \mathbf{a}(\boldsymbol{\eta}) e^{j\varphi} \alpha\|^2}{N} \right) + \frac{(x_a - \varphi)^2}{2\sigma_{n_a}^2} + \frac{1}{2} \ln(2\pi \sigma_{n_a}^2) \\ &= N \ln\left(\|\mathbf{x} - \mathbf{a}(\boldsymbol{\eta}) e^{j\varphi} \alpha\|^2 \right) + \frac{(x_a - \varphi)^2}{2\sigma_{n_a}^2} + \text{const}, \end{aligned} \tag{5.8}$$

where the constant terms do not depend on the parameters of interest. The optimal α is obtained by minimizing $\|\mathbf{x} - \mathbf{a}(\boldsymbol{\eta}) e^{j\varphi} \alpha\|^2$, which under the constraint $\alpha \in \mathbb{R}^+$ yields

$$\widehat{\alpha} = \frac{\Re\left\{ e^{-j\varphi} \mathbf{a}(\boldsymbol{\eta})^{\mathrm{H}} \mathbf{x} \right\}}{\|\mathbf{a}(\boldsymbol{\eta})\|^2}. \tag{5.9}$$

Using orthogonal projection properties, the residual term becomes,

$$\|\mathbf{x} - \mathbf{a}(\boldsymbol{\eta})e^{j\varphi}\widehat{\alpha}\|^2 = \|\mathbf{x}\|^2 - \frac{|\mathbf{a}(\boldsymbol{\eta})^{\mathrm{H}}e^{-j\varphi}\mathbf{x}|^2}{\|\mathbf{a}(\boldsymbol{\eta})\|^2}. \tag{5.10}$$

Since $\|\mathbf{x}\|^2$ is constant with respect to the parameters, and using the property that $|\cdot|^2 = \Re\{\cdot\}^2 + \Im\{\cdot\}^2$ with the constraint $\Re\left\{e^{-j\varphi}\mathbf{a}(\boldsymbol{\eta})^{\mathrm{H}}\mathbf{x}\right\} > 0$ ensuring $\widehat{\alpha} > 0$, the cost function simplifies to

$$\mathcal{S}_2(\mathbf{x}; \widehat{\alpha}, \boldsymbol{\eta}, \varphi) = \frac{\sigma_n^2}{2\sigma_{n_a}^2}(x_a - \varphi)^2 - \Re\left\{e^{-j\varphi}\frac{\mathbf{a}(\boldsymbol{\eta})^{\mathrm{H}}\mathbf{x}}{\|\mathbf{a}(\boldsymbol{\eta})\|}\right\}^2. \tag{5.11}$$

This can be further expanded by factoring out the phase compensation through x_a

$$\mathcal{S}_2(\mathbf{x}; \widehat{\alpha}, \boldsymbol{\eta}) = \frac{\sigma_n^2}{2\sigma_{n_a}^2}(x_a - \varphi)^2 - \Re\left\{e^{j(x_a-\varphi)}\gamma(\boldsymbol{\eta})\right\}^2, \tag{5.12}$$

where $\gamma(\boldsymbol{\eta})$ is defined as the normalized correlation function

$$\gamma(\boldsymbol{\eta}) = \frac{\mathbf{a}(\boldsymbol{\eta})^{\mathrm{H}}(e^{-jx_a}\mathbf{x})}{\|\mathbf{a}(\boldsymbol{\eta})\|}. \tag{5.13}$$

Introducing the phase compensation error $\varepsilon = \varphi - x_a$ transforms the cost function to

$$\mathcal{S}_2(\mathbf{x}; \boldsymbol{\theta}) = \frac{\sigma_n^2}{2\sigma_{n_a}^2}\varepsilon^2 - \Re\left\{e^{-j\varepsilon}\gamma(\boldsymbol{\eta})\right\}^2. \tag{5.14}$$

This formulation reveals the fundamental structure: the estimation problem requires jointly optimizing over both the phase error ε and the parameters of interest $\boldsymbol{\eta}$.

5.3.2 Naive Estimator

The naive approach emerges when the available phase observable x_a is directly applied for compensation without consideration of its measurement uncertainty. This corresponds to setting $\varepsilon = 0$ in the cost function despite the presence of noise n_a in the phase measurement, yielding

$$\widehat{\boldsymbol{\eta}_n} = \underset{\{\boldsymbol{\eta}|\Re\{\gamma(\boldsymbol{\eta})\}>0\}}{\arg\max} \left\{\Re\left\{\gamma(\boldsymbol{\eta})\right\}^2\right\}, \tag{5.15}$$

where $\gamma(\boldsymbol{\eta})$ represents the normalized correlation function of $\mathbf{a}(\boldsymbol{\eta})$ weighted by e^{-jx_a}. This estimator provides a computationally efficient implementation applicable whenever auxiliary phase measurements are available.

The naive estimator serves as a practical benchmark, representing a common engineering approach of directly applying available measurements without sophisticated statistical processing. Its performance relative to the phase-aware estimator quantifies the value of proper uncertainty characterization.

5.3.3 Phase-aware Estimator

The phase-aware estimator properly accounts for the phase measurement uncertainty characterized by $\sigma_{n_a}^2$. The relationship to the naive estimator becomes apparent through examination of the cost function: setting $\varepsilon = 0$ in the general formulation recovers the naive estimator from the phase-aware framework. To incorporate uncertainty, the optimization must jointly consider both ε (representing the phase error) and $\boldsymbol{\eta}$.

To reduce computational complexity, the cost function can be reformulated using the identity $\Re\{z\}^2 = \frac{\Re\{z^2\}+|z|^2}{2}$ for any complex number z. Applying this identity

$$\Re\left\{e^{-j\varepsilon}\gamma\left(\boldsymbol{\eta}\right)\right\}^2 = \frac{\Re\left\{\left(e^{-j\varepsilon}\gamma\left(\boldsymbol{\eta}\right)\right)^2\right\} + \left|e^{-j\varepsilon}\gamma\left(\boldsymbol{\eta}\right)\right|^2}{2} = \frac{\Re\left\{e^{-j2\varepsilon}\gamma\left(\boldsymbol{\eta}\right)^2\right\} + \left|\gamma\left(\boldsymbol{\eta}\right)\right|^2}{2}. \tag{5.16}$$

Within the asymptotic regime where $\sigma_{n_a}^2 \ll 1$ implies $\varepsilon \ll 1$, a fifth-order Taylor expansion approximates $e^{-j2\varepsilon}$

$$\begin{aligned} e^{-j2\varepsilon} &\simeq 1 + (-j2\varepsilon) + \frac{1}{2}(-j2\varepsilon)^2 + \frac{1}{6}(-j2\varepsilon)^3 + \frac{1}{24}(-j2\varepsilon)^4 + \frac{1}{120}(-j2\varepsilon)^5 \\ &1 - 2\varepsilon^2 + \frac{2}{3}\varepsilon^4 - j\left(2\varepsilon - \frac{4}{3}\varepsilon^3 + \frac{4}{15}\varepsilon^5\right). \end{aligned} \tag{5.17}$$

The choice of fifth-order truncation balances approximation accuracy with computational complexity. The resulting fourth-degree polynomial in equation (5.21) can be solved analytically using Ferrari's method (D. 1990), which reduces the dimensionality of the optimization problem by eliminating the need for numerical search over ε. The next term in the Taylor series is $-\frac{4\varepsilon^6}{45}$, which becomes negligible compared to the fifth-order term for $|\varepsilon| \ll 1$. Figure 5.1 validates this approximation, demonstrating that the absolute error $|e^{-j2\varepsilon} - \text{approximation}|$ remains below 10^{-3} for $|\varepsilon| \leq 0.1$. The threshold $|\varepsilon| \leq 0.1$ radians is chosen such that the neglected sixth-order term $\frac{4\varepsilon^6}{45}$ remains at least two orders of magnitude smaller than the retained fifth-order term $\frac{4\varepsilon^5}{15}$, confirming sufficient accuracy within the asymptotic regime where $\varepsilon \ll 1$ radians. The logarithmic scale in the error subplot reveals that the approximation error decreases rapidly as $|\varepsilon|$ approaches zero, validating the asymptotic assumption leveraged for the Taylor expansion.

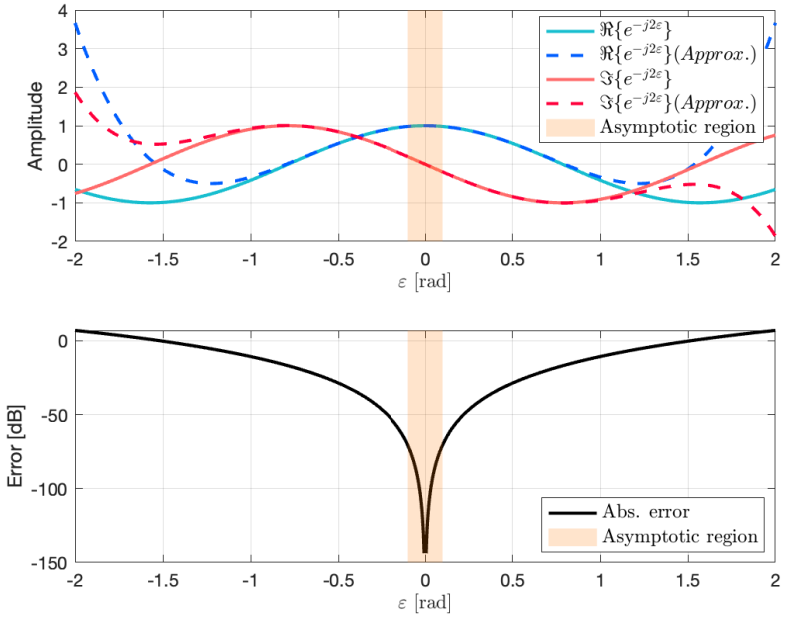

Figure 5.1: Validation of fifth-order Taylor approximation of $e^{-j2\varepsilon}$. Upper subplot: comparison between exact function and approximation for real and imaginary parts. Lower subplot: absolute approximation error $|e^{-j2\varepsilon} - \text{approximation}|$ on logarithmic scale. The shaded region indicates the asymptotic regime where $|\varepsilon| \leq 0.1$.

Consequently, (5.16) becomes,

$$\Re\left\{e^{-j\varepsilon}\gamma\left(\boldsymbol{\eta}\right)\right\}^2 \simeq \frac{2}{15}\Im\left\{\gamma\left(\boldsymbol{\eta}\right)^2\right\}\varepsilon^5 + \frac{1}{3}\Re\left\{\gamma\left(\boldsymbol{\eta}\right)^2\right\}\varepsilon^4 - \frac{2}{3}\Im\left\{\gamma\left(\boldsymbol{\eta}\right)^2\right\}\varepsilon^3 - \Re\left\{\gamma\left(\boldsymbol{\eta}\right)^2\right\}\varepsilon^2 + \Im\left\{\gamma\left(\boldsymbol{\eta}\right)^2\right\}\varepsilon + \Re\left\{\gamma\left(\boldsymbol{\eta}\right)\right\}^2, \quad (5.18)$$

where $\Im\{\cdot\}$ denotes the imaginary part operator. Incorporating this expansion into (5.14) produces

$$\mathcal{S}_2\left(\mathbf{x};\theta\right) \simeq -\frac{2}{15}\Im\left\{\gamma\left(\boldsymbol{\eta}\right)^2\right\}\varepsilon^5 - \frac{1}{3}\Re\left\{\gamma\left(\boldsymbol{\eta}\right)^2\right\}\varepsilon^4 + \frac{2}{3}\Im\left\{\gamma\left(\boldsymbol{\eta}\right)^2\right\}\varepsilon^3 + \frac{1}{2}\left(\frac{\sigma_n^2}{\sigma_{n_a}^2} + 2\Re\left\{\gamma\left(\boldsymbol{\eta}\right)^2\right\}\right)\varepsilon^2 - \Im\left\{\gamma\left(\boldsymbol{\eta}\right)^2\right\}\varepsilon - \Re\left\{\gamma\left(\boldsymbol{\eta}\right)\right\}^2, \quad (5.19)$$

This polynomial form enables sequential optimization: first solving for ε given $\boldsymbol{\eta}$, then optimizing over $\boldsymbol{\eta}$. The phase error estimator is obtained by

$$\widehat{\varepsilon}\left(\boldsymbol{\eta}\right) = \arg\min_{\{\varepsilon|\Re\{e^{-j\varepsilon}\gamma(\boldsymbol{\eta})\}>0\}}\left\{\mathcal{S}_2\left(\mathbf{x};\varepsilon,\boldsymbol{\eta}\right)\right\} = \arg_{\{\varepsilon|\Re\{e^{-j\varepsilon}\gamma(\boldsymbol{\eta})\}>0\}}\left\{\frac{\partial\mathcal{S}_2\left(\mathbf{x};\varepsilon,\boldsymbol{\eta}\right)}{\partial\varepsilon} = 0\right\}. \quad (5.20)$$

Taking the derivative with respect to ε

$$\frac{\partial\mathcal{S}_2\left(\mathbf{x};\varepsilon,\boldsymbol{\eta}\right)}{\partial\varepsilon} \simeq -\frac{2}{3}\Im\left\{\gamma\left(\boldsymbol{\eta}\right)^2\right\}\varepsilon^4 - \frac{4}{3}\Re\left\{\gamma\left(\boldsymbol{\eta}\right)^2\right\}\varepsilon^3 + 2\Im\left\{\gamma\left(\boldsymbol{\eta}\right)^2\right\}\varepsilon^2 - \Im\left\{\gamma\left(\boldsymbol{\eta}\right)^2\right\} + \left(\frac{\sigma_n^2}{\sigma_{n_a}^2} + 2\Re\left\{\gamma\left(\boldsymbol{\eta}\right)^2\right\}\right)\varepsilon. \quad (5.21)$$

The estimator $\widehat{\varepsilon}$ in (5.20) requires solving this fourth-degree polynomial, which yields four possible roots for each $\boldsymbol{\eta}$. The valid root is determined through

$$\widehat{\varepsilon} = \arg\min\left\{\mathcal{S}_2\left(\mathbf{x};\Re\{\widehat{\varepsilon}_1\},\boldsymbol{\eta}\right),\ldots,\mathcal{S}_2\left(\mathbf{x};\Re\{\widehat{\varepsilon}_4\},\boldsymbol{\eta}\right)\right\}, \quad (5.22)$$

selecting the root whose real part minimizes the cost function in (5.19). After determining $\widehat{\varepsilon}$ for each candidate $\boldsymbol{\eta}$, the final phase-aware estimator becomes,

$$\widehat{\boldsymbol{\eta}} = \arg\max_{\boldsymbol{\eta}}\left\{\mathcal{S}_2\left(\mathbf{x};\widehat{\varepsilon}(\boldsymbol{\eta}),\boldsymbol{\eta}\right)\right\} = \arg\max_{\boldsymbol{\eta}}\left\{\frac{\sigma_n^2\widehat{\varepsilon}(\boldsymbol{\eta})^2}{2\sigma_{n_a}^2} - \Re\left\{e^{-j\widehat{\varepsilon}(\boldsymbol{\eta})}\gamma(\boldsymbol{\eta})\right\}^2\right\}. \quad (5.23)$$

This phase-aware estimator explicitly incorporates the statistical properties of the phase observable x_a through the polynomial formulation, providing a computationally tractable alternative to direct joint optimization while accounting for the phase uncertainty characterized by $\sigma_{n_a}^2$.

5.4 Cramér-Rao Bound

The extended signal model incorporating phase observables modifies the structure of the FIM, enabling quantification of performance improvements as a function of phase observation quality. This section derives the CRB for the extended CSM, establishing fundamental performance limits that account for the information content of auxiliary phase measurements.

The joint probability density function in equation (5.2) leads to a FIM with a block structure reflecting the separation between signal and phase observations. The FIM decomposes as,

$$\begin{aligned}\mathbf{F}_{\boldsymbol{\epsilon}} &= E\left\{-\frac{\partial^2\ln P(\mathbf{x},x_a;\boldsymbol{\epsilon})}{\partial\boldsymbol{\epsilon}\partial\boldsymbol{\epsilon}^{\mathrm{T}}}\right\} = E\left\{-\frac{\partial^2\big(\ln P(\mathbf{x};\boldsymbol{\epsilon}) + \ln P(x_a;\varphi)\big)}{\partial\boldsymbol{\epsilon}\partial\boldsymbol{\epsilon}^{\mathrm{T}}}\right\},\\ &= E\left\{-\frac{\partial^2\ln P(\mathbf{x};\boldsymbol{\epsilon})}{\partial\boldsymbol{\epsilon}\partial\boldsymbol{\epsilon}^{\mathrm{T}}}\right\} + E\left\{-\frac{\partial^2\ln P(x_a;\varphi)\big)}{\partial\boldsymbol{\epsilon}\partial\boldsymbol{\epsilon}^{\mathrm{T}}}\right\} = \mathbf{F}(\mathbf{x},\boldsymbol{\epsilon}) + \mathbf{F}(\varphi), \end{aligned} \quad (5.24)$$

where $\mathbf{F}(\mathbf{x},\boldsymbol{\epsilon})$ corresponds to the information contribution from the complex baseband signal observation, and $\mathbf{F}(\varphi)$ accounts for the real-valued information from the noisy phase measurement. $\mathbf{F}(\boldsymbol{\epsilon})$ is obtained from the SBF (2.13) expressions accordingly. $\mathbf{F}(\mathbf{x},\boldsymbol{\epsilon})$ is directly obtained here from (2.13b), instead of, as in the previous chapter, rearranging in a real-valued equivalent form to apply (2.13a), since both operations yield the same result. For $\mathbf{F}(\varphi)$, (2.13a) is also applied revealing a blocks structure organized according to the parameters of interest as

$$\mathbf{F}_{\boldsymbol{\epsilon}} = \begin{bmatrix} \frac{N}{(\sigma_n^2)^2} & \mathbf{0}^{\mathrm{T}} \\ \mathbf{0} & \mathbf{F}_{\boldsymbol{\zeta}|\boldsymbol{\epsilon}} \end{bmatrix}, \quad \mathbf{F}_{\boldsymbol{\zeta}|\boldsymbol{\epsilon}} = \begin{bmatrix} \mathrm{F}_{\alpha|\boldsymbol{\epsilon}} & \mathbf{F}_{\alpha,\boldsymbol{\theta}|\boldsymbol{\epsilon}} \\ \mathbf{F}_{\boldsymbol{\theta},\alpha|\boldsymbol{\epsilon}} & \mathbf{F}_{\boldsymbol{\theta}|\boldsymbol{\epsilon}} \end{bmatrix}, \quad \mathbf{F}_{\boldsymbol{\theta}|\boldsymbol{\epsilon}} = \begin{bmatrix} \mathrm{F}_{\varphi|\boldsymbol{\epsilon}} & \mathbf{F}_{\varphi,\boldsymbol{\eta}|\boldsymbol{\epsilon}} \\ \mathbf{F}_{\boldsymbol{\eta},\varphi|\boldsymbol{\epsilon}} & \mathbf{F}_{\boldsymbol{\eta}|\boldsymbol{\epsilon}} \end{bmatrix}, \tag{5.25a}$$

with,

$$\mathbf{F}_{\boldsymbol{\zeta}|\boldsymbol{\epsilon}} = \frac{2}{\sigma_n^2} \begin{bmatrix} \|\mathbf{a}(\boldsymbol{\eta})\|^2 & \left[0, \quad \alpha\Re\left\{\mathbf{a}(\boldsymbol{\eta})^H \frac{\partial \mathbf{a}(\boldsymbol{\eta})}{\partial \boldsymbol{\eta}^{\mathrm{T}}}\right\}\right] \\ \left[0, \quad \alpha\Re\left\{\mathbf{a}(\boldsymbol{\eta})^H \frac{\partial \mathbf{a}(\boldsymbol{\eta})}{\partial \boldsymbol{\eta}^{\mathrm{T}}}\right\}\right]^{\mathrm{T}} & \mathbf{F}_{\boldsymbol{\theta}|\boldsymbol{\epsilon}} \end{bmatrix}, \tag{5.25b}$$

$$\mathbf{F}_{\boldsymbol{\theta}|\boldsymbol{\epsilon}} = \alpha^2 \begin{bmatrix} \|\mathbf{a}(\boldsymbol{\eta})\|^2 + \frac{\sigma_n^2}{2\sigma_{n_a}^2} & \Im\left\{\mathbf{a}(\boldsymbol{\eta})^H \frac{\partial \mathbf{a}(\boldsymbol{\eta})}{\partial \boldsymbol{\eta}^{\mathrm{T}}}\right\} \\ \Im\left\{\mathbf{a}(\boldsymbol{\eta})^H \frac{\partial \mathbf{a}(\boldsymbol{\eta})}{\partial \boldsymbol{\eta}^{\mathrm{T}}}\right\}^{\mathrm{T}} & \Re\left\{\left(\frac{\partial \mathbf{a}(\boldsymbol{\eta})}{\partial \boldsymbol{\eta}^{\mathrm{T}}}\right)^H \frac{\partial \mathbf{a}(\boldsymbol{\eta})}{\partial \boldsymbol{\eta}^{\mathrm{T}}}\right\} \end{bmatrix}. \tag{5.25c}$$

In the top-left element of (5.25c), the additive term $\frac{\sigma_n^2}{2\sigma_{n_a}^2}$ reflects the information contributed by the noisy measurement of φ. The CRB is directly obtained by inverting $\mathbf{F}_{\boldsymbol{\zeta}|\boldsymbol{\epsilon}}$, by blocks as in Sec. 4.4,

$$\begin{aligned} \mathbf{CRB}_{\boldsymbol{\theta}|\boldsymbol{\epsilon}} &= \frac{\sigma_n^2}{2\alpha^2}\left[\mathbf{F}_{\boldsymbol{\theta}|\boldsymbol{\epsilon}} - \mathbf{F}_{\boldsymbol{\theta},\alpha|\boldsymbol{\epsilon}}\mathbf{F}_{\alpha|\boldsymbol{\epsilon}}^{-1}\mathbf{F}_{\alpha,\boldsymbol{\theta}|\boldsymbol{\epsilon}}\right]^{-1} \\ &= \frac{\sigma_n^2}{2\alpha^2}\left[\mathbf{F}_{\boldsymbol{\theta}|\boldsymbol{\epsilon}} - \frac{\left[0, \quad \alpha\Re\left\{\mathbf{a}(\boldsymbol{\eta})^H \frac{\partial \mathbf{a}(\boldsymbol{\eta})}{\partial \boldsymbol{\eta}^{\mathrm{T}}}\right\}\right]^{\mathrm{T}}\left[0, \quad \alpha\Re\left\{\mathbf{a}(\boldsymbol{\eta})^H \frac{\partial \mathbf{a}(\boldsymbol{\eta})}{\partial \boldsymbol{\eta}^{\mathrm{T}}}\right\}\right]}{\|\mathbf{a}(\boldsymbol{\eta})\|^2}\right]^{-1} \\ &= \frac{\sigma_n^2}{2\alpha^2}\begin{bmatrix} \|\mathbf{a}(\boldsymbol{\eta})\|^2 + \frac{\sigma_n^2}{2\alpha^2}\frac{1}{\sigma_{n_a}^2} & \Im\left\{\mathbf{a}(\boldsymbol{\eta})^H \frac{\partial \mathbf{a}(\boldsymbol{\eta})}{\partial \boldsymbol{\eta}^{\mathrm{T}}}\right\} \\ \Im\left\{\mathbf{a}(\boldsymbol{\eta})^H \frac{\partial \mathbf{a}(\boldsymbol{\eta})}{\partial \boldsymbol{\eta}^{\mathrm{T}}}\right\}^{\mathrm{T}} & \mathbf{F}_{\boldsymbol{\eta}|\boldsymbol{\epsilon}} \end{bmatrix}^{-1}. \end{aligned} \tag{5.26}$$

where,

$$\mathbf{F}_{\boldsymbol{\eta}|\boldsymbol{\epsilon}} = \Re\left\{\left(\frac{\partial \mathbf{a}(\boldsymbol{\eta})}{\partial \boldsymbol{\eta}^{\mathrm{T}}}\right)^H \frac{\partial \mathbf{a}(\boldsymbol{\eta})}{\partial \boldsymbol{\eta}^{\mathrm{T}}}\right\} - \frac{\Re\left\{\mathbf{a}(\boldsymbol{\eta})^H \frac{\partial \mathbf{a}(\boldsymbol{\eta})}{\partial \eta^{\mathrm{T}}}\right\}^{\mathrm{T}}\Re\left\{\mathbf{a}(\boldsymbol{\eta})^H \frac{\partial \mathbf{a}(\boldsymbol{\eta})}{\partial \boldsymbol{\eta}^{\mathrm{T}}}\right\}}{\|\mathbf{a}(\boldsymbol{\eta})\|^2}. \tag{5.27}$$

Placing focus to the matrix element corresponding to $\boldsymbol{\eta}$, when the block inversion operation is again applied to $\mathrm{F}_{\boldsymbol{\eta}|\boldsymbol{\epsilon}}$ it yields

$$\mathbf{CRB}_{\boldsymbol{\eta}|\boldsymbol{\epsilon}} = \frac{\sigma_n^2}{2\alpha^2}\left[\mathbf{F}_{\boldsymbol{\eta}|\boldsymbol{\epsilon}} - \frac{\Im\left\{\mathbf{a}(\boldsymbol{\eta})^H \frac{\partial \mathbf{a}(\boldsymbol{\eta})}{\partial \eta^{\mathrm{T}}}\right\}^{\mathrm{T}}\Im\left\{\mathbf{a}(\boldsymbol{\eta})^H \frac{\partial \mathbf{a}(\boldsymbol{\eta})}{\partial \boldsymbol{\eta}^{\mathrm{T}}}\right\}}{\|\mathbf{a}(\boldsymbol{\eta})\|^2 + \frac{\sigma_n^2}{2\alpha^2}\frac{1}{\sigma_{n_a}^2}}\right]^{-1}. \tag{5.28}$$

Considering, the SNR at the output of the receiver's matched filter (Kay 1993), for the true parameter $\boldsymbol{\eta}^0$ can be determined as,

$$\mathrm{SNR}_{\mathrm{out}} = \left.\frac{\Re\left\{\left(\frac{\mathbf{a}(\eta)}{\|\mathbf{a}(\eta)\|}\right)^{\mathrm{H}}\left(\alpha^0\mathbf{a}\left(\eta^0\right)\right)\right\}^2}{\mathrm{E}\left[\Re\left\{\left(\frac{\mathbf{a}(\eta)}{\|\mathbf{a}(\eta)\|}\right)^{\mathrm{H}}\mathbf{n}\right\}^2\right]}\right|_{\eta} = \frac{\left(\alpha^0\right)^2\left\|\mathbf{a}\left(\eta^0\right)\right\|^2}{\frac{(\sigma_n^0)^2}{2}} = \frac{2\|\mathbf{a}\|^2}{\left(\sigma_n^0\right)^2}\left(\alpha^0\right)^2 \tag{5.29}$$

The denominator in (5.28) can be reformulated as,

$$\frac{1}{\|\mathbf{a}(\boldsymbol{\eta})\|^2+\frac{\sigma_n^2}{2\alpha^2}\frac{1}{\sigma_{n_a}^2}}=\frac{1}{\|\mathbf{a}(\boldsymbol{\eta})\|^2+\frac{\|\mathbf{a}(\boldsymbol{\eta})\|^2}{2\mathrm{SNR}_{\mathrm{out}}\sigma_{n_a}^2}}=\frac{1}{\|\mathbf{a}(\boldsymbol{\eta})\|^2\left(1+\frac{1}{2\mathrm{SNR}_{\mathrm{out}}\sigma_{n_a}^2}\right)}, \tag{5.30}$$

$$=\frac{1}{\|\mathbf{a}(\boldsymbol{\eta})\|^2\left(\frac{1+2\mathrm{SNR}_{\mathrm{out}}\sigma_{n_a}^2}{2\mathrm{SNR}_{\mathrm{out}}\sigma_{n_a}^2}\right)}=\frac{2\mathrm{SNR}_{\mathrm{out}}\sigma_{n_a}^2}{\|\mathbf{a}(\boldsymbol{\eta})\|^2\left(1+2\mathrm{SNR}_{\mathrm{out}}\sigma_{n_a}^2\right)}, \tag{5.31}$$

$$=\frac{1}{\|\mathbf{a}(\boldsymbol{\eta})\|^2}-\frac{1}{\|\mathbf{a}(\boldsymbol{\eta})\|^2\left(1+2\sigma_{n_a}^2\mathrm{SNR}_{\mathrm{out}}\right)}. \tag{5.32}$$

Such result can be leveraged to refactor the righ-and-side term in (5.28) as,

$$\begin{aligned}&\frac{\Im\left\{\mathbf{a}(\boldsymbol{\eta})^H\frac{\partial\mathbf{a}(\boldsymbol{\eta})}{\partial\eta^{\mathrm{T}}}\right\}^{\mathrm{T}}\Im\left\{\mathbf{a}(\boldsymbol{\eta})^H\frac{\partial\mathbf{a}(\boldsymbol{\eta})}{\partial\boldsymbol{\eta}^{\mathrm{T}}}\right\}}{\|\mathbf{a}(\boldsymbol{\eta})\|^2+\frac{\sigma_n^2}{2\alpha^2}\frac{1}{\sigma_{n_a}^2}}\\&=\frac{\Im\left\{\mathbf{a}(\boldsymbol{\eta})^H\frac{\partial\mathbf{a}(\boldsymbol{\eta})}{\partial\eta^{\mathrm{T}}}\right\}^{\mathrm{T}}\Im\left\{\mathbf{a}(\boldsymbol{\eta})^H\frac{\partial\mathbf{a}(\boldsymbol{\eta})}{\partial\boldsymbol{\eta}^{\mathrm{T}}}\right\}}{\|\mathbf{a}(\boldsymbol{\eta})\|^2}-\frac{\Im\left\{\mathbf{a}(\boldsymbol{\eta})^H\frac{\partial\mathbf{a}(\boldsymbol{\eta})}{\partial\eta^{\mathrm{T}}}\right\}^{\mathrm{T}}\Im\left\{\mathbf{a}(\boldsymbol{\eta})^H\frac{\partial\mathbf{a}(\boldsymbol{\eta})}{\partial\boldsymbol{\eta}^{\mathrm{T}}}\right\}}{\|\mathbf{a}(\boldsymbol{\eta})\|^2\left(1+2\sigma_{n_a}^2\mathrm{SNR}_{\mathrm{out}}\right)}.\end{aligned} \tag{5.33}$$

which transforms (5.28) into,

$$\mathbf{CRB}_{\boldsymbol{\eta}|\boldsymbol{\epsilon}}=\frac{\sigma_n^2}{2\alpha^2}\left[\mathbf{F}_{\boldsymbol{\eta}|\boldsymbol{\epsilon}}-\frac{\Im\left\{\mathbf{a}(\boldsymbol{\eta})^H\frac{\partial\mathbf{a}(\boldsymbol{\eta})}{\partial\eta^{\mathrm{T}}}\right\}^{\mathrm{T}}\Im\left\{\mathbf{a}(\boldsymbol{\eta})^H\frac{\partial\mathbf{a}(\boldsymbol{\eta})}{\partial\boldsymbol{\eta}^{\mathrm{T}}}\right\}}{\|\mathbf{a}(\boldsymbol{\eta})\|^2+\frac{\sigma_n^2}{2\alpha^2}\frac{1}{\sigma_{n_a}^2}}\right]^{-1}, \tag{5.34a}$$

$$\begin{aligned}&=\frac{\sigma_n^2}{2\alpha^2}\left[\Re\left\{\left(\frac{\partial\mathbf{a}(\boldsymbol{\eta})}{\partial\boldsymbol{\eta}^{\mathrm{T}}}\right)^H\Pi_{\mathbf{a}(\boldsymbol{\eta})}^{\perp}\frac{\partial\mathbf{a}(\boldsymbol{\eta})}{\partial\boldsymbol{\eta}^{\mathrm{T}}}\right\}+\frac{\Im\left\{\mathbf{a}(\boldsymbol{\eta})^H\frac{\partial\mathbf{a}(\boldsymbol{\eta})}{\partial\eta^{\mathrm{T}}}\right\}^{\mathrm{T}}\Im\left\{\mathbf{a}(\boldsymbol{\eta})^H\frac{\partial\mathbf{a}(\boldsymbol{\eta})}{\partial\boldsymbol{\eta}^{\mathrm{T}}}\right\}}{\|\mathbf{a}(\boldsymbol{\eta})\|^2\left(1+2\sigma_{n_a}^2\mathrm{SNR}_{\mathrm{out}}\right)}\right]^{-1}\\&=\frac{\sigma_n^2}{2\alpha^2}\left[\boldsymbol{\Phi}_{\mathrm{co}}(\boldsymbol{\eta})+\frac{\Im\left\{\mathbf{a}(\boldsymbol{\eta})^H\frac{\partial\mathbf{a}(\boldsymbol{\eta})}{\partial\eta^{\mathrm{T}}}\right\}^{\mathrm{T}}\Im\left\{\mathbf{a}(\boldsymbol{\eta})^H\frac{\partial\mathbf{a}(\boldsymbol{\eta})}{\partial\boldsymbol{\eta}^{\mathrm{T}}}\right\}}{\|\mathbf{a}(\boldsymbol{\eta})\|^2\left(1+2\sigma_{n_a}^2\mathrm{SNR}_{\mathrm{out}}\right)}\right]^{-1},\end{aligned} \tag{5.34b}$$

where the relationship (4.24) was applied, and the FIM term $\boldsymbol{\Phi}_{\mathrm{co}}(\boldsymbol{\eta})$ is the FIM in (3.27) derived from the conventional signal model.

Applying block matrix inversion to the remaining matrix elements in equation (5.26) yields the individual bounds,

$$\mathbf{CRB}_{\varphi|\boldsymbol{\epsilon}}=\frac{\sigma_n^2}{2\alpha^2}\left[\frac{1}{\sigma_{n_a}^2}+\frac{1}{\frac{1}{2\mathrm{SNR}_{\mathrm{out}}}+\frac{\Im\left\{\mathbf{a}(\boldsymbol{\eta})^{\mathrm{H}}\frac{\partial\mathbf{a}(\boldsymbol{\eta})}{\partial\boldsymbol{\eta}^{\mathrm{T}}}\right\}^{\mathrm{T}}\Im\left\{\mathbf{a}(\boldsymbol{\eta})^{\mathrm{H}}\frac{\partial\mathbf{a}(\boldsymbol{\eta})}{\partial\boldsymbol{\eta}^{\mathrm{T}}}\right\}}{\boldsymbol{\Phi}_{\mathrm{op}}(\boldsymbol{\eta})\|\mathbf{a}(\boldsymbol{\eta})\|^4}}\right]^{-1} \tag{5.35a}$$

$$\mathbf{CRB}_{\boldsymbol{\eta},\varphi|\boldsymbol{\epsilon}}=-\mathbf{CRB}_{\boldsymbol{\eta}|\boldsymbol{\epsilon}}\frac{\Im\left\{\mathbf{a}(\boldsymbol{\eta})^{\mathrm{H}}\frac{\partial\mathbf{a}(\boldsymbol{\eta})}{\partial\boldsymbol{\eta}^{\mathrm{T}}}\right\}^{\mathrm{T}}}{\|\mathbf{a}(\boldsymbol{\eta})\|^2}\frac{1}{1+\frac{1}{2\mathrm{SNR}_{\mathrm{out}}\sigma_{n_a}^2}}, \tag{5.35b}$$

It is worth noting that

$$\mathbf{CRB}_{\varphi|\boldsymbol{\epsilon}}\geq\sigma_{n_a}^2\frac{1}{1+2\sigma_{n_a}^2\mathrm{SNR}_{\mathrm{out}}}=\frac{1}{2\mathrm{SNR}_{\mathrm{out}}}\frac{1}{1+\frac{1}{2\sigma_{n_a}^2\mathrm{SNR}_{\mathrm{out}}}}, \tag{5.36}$$

with equality if $\Im\left\{\mathbf{a}\left(\boldsymbol{\eta}\right)^{H}\left(\frac{\partial\mathbf{a}(\boldsymbol{\eta})}{\partial\boldsymbol{\eta}^{\mathrm{T}}}\right)\right\}=\mathbf{0}$.

Equation (5.34) reveals the fundamental structure of phase-enhanced estimation for time-delay and Doppler parameters. The additional term beyond $\boldsymbol{\Phi}_{\mathrm{co}}(\boldsymbol{\eta})$ vanishes as $2\sigma_{n_a}^2\mathrm{SNR}_{\mathrm{out}}\to\infty$, quantifying precisely when phase information becomes negligible. The cross-correlation terms in equation (5.35b) demonstrate that statistical coupling between phase and propagation parameters is modulated by the factor $(1+\frac{1}{2\mathrm{SNR}_{\mathrm{out}}\sigma_{n_a}^2})^{-1}$, which approaches zero under high phase uncertainty, justifying the traditional assumption of parameter decoupling. These theoretical limits establish the performance continuum across which practical estimators must operate, providing quantitative criteria for technology selection and system design.

5.4.1 Edge cases

The derived expressions reveal two limiting cases that connect to the frameworks established in previous chapters. As $\sigma_{n_a}^2\to\infty$, the phase measurement becomes uninformative and the additional term in equation (5.34) vanishes, recovering the conventional FIM (3.27) without side information as presented in Section 3.5:

$$\lim_{\sigma_{n_a}^2\to\infty}\frac{1}{1+2\sigma_{n_a}^2\mathrm{SNR}_{\mathrm{out}}}=0, \tag{5.37a}$$

yielding

$$\lim_{\sigma_{n_a}^2\to\infty}\mathbf{CRB}_{\boldsymbol{\eta}|\boldsymbol{\epsilon}}=\frac{\sigma_n^2}{2\alpha^2}(\boldsymbol{\Phi}_{\mathrm{co}}(\boldsymbol{\eta}))^{-1}, \tag{5.37b}$$

$$\lim_{\sigma_{n_a}^2\to\infty}\mathbf{CRB}_{\varphi|\boldsymbol{\epsilon}}=\frac{1}{2\mathrm{SNR}_{\mathrm{out}}}+\frac{\Im\left\{\mathbf{a}(\boldsymbol{\eta})^{\mathrm{H}}\frac{\partial\mathbf{a}(\boldsymbol{\eta})}{\partial\boldsymbol{\eta}^{\mathrm{T}}}\right\}^{\mathrm{T}}}{\|\mathbf{a}(\boldsymbol{\eta})\|^2}\mathbf{CRB}_{\boldsymbol{\eta}|\boldsymbol{\epsilon}}\frac{\Im\left\{\mathbf{a}(\boldsymbol{\eta})^{\mathrm{H}}\frac{\partial\mathbf{a}(\boldsymbol{\eta})}{\partial\boldsymbol{\eta}^{\mathrm{T}}}\right\}}{\|\mathbf{a}(\boldsymbol{\eta})\|^2}, \tag{5.37c}$$

$$\lim_{\sigma_{n_a}^2\to\infty}\mathbf{CRB}_{\boldsymbol{\eta},\varphi|\boldsymbol{\epsilon}}=-\mathbf{CRB}_{\boldsymbol{\eta}|\boldsymbol{\epsilon}}\frac{\Im\left\{\mathbf{a}(\boldsymbol{\eta})^{\mathrm{H}}\frac{\partial\mathbf{a}(\boldsymbol{\eta})}{\partial\boldsymbol{\eta}^{\mathrm{T}}}\right\}^{\mathrm{T}}}{\|\mathbf{a}(\boldsymbol{\eta})\|^2}. \tag{5.37d}$$

The expressions for $\mathbf{CRB}_{\boldsymbol{\eta}|\boldsymbol{\epsilon}}$, $\mathbf{CRB}_{\varphi|\boldsymbol{\epsilon}}$ and $\mathbf{CRB}_{\boldsymbol{\eta},\varphi|\boldsymbol{\epsilon}}$ align with those in (Medina 2020, (15)) when considering the signal model (5.3b), corresponding to the conventional treatment where phase information is absorbed into the complex amplitude. Note that $\boldsymbol{\Phi}_{\mathrm{co}}(\boldsymbol{\eta})$ is the expression in (3.27).

Conversely, when $\sigma_{n_a}^2\to 0$, perfect phase knowledge becomes available, leading to the enhanced performance analyzed in Chapter 4:

$$\lim_{\sigma_{n_a}^2\to 0}\frac{1}{1+2\sigma_{n_a}^2\mathrm{SNR}_{\mathrm{out}}}=1,\quad \lim_{\sigma_{n_a}^2\to 0}\frac{1}{1+\frac{1}{2\mathrm{SNR}_{\mathrm{out}}\sigma_{n_a}^2}}=0, \tag{5.38}$$

yielding:

$$\lim_{\sigma_{n_a}^2 \to 0} \mathbf{CRB}_{\boldsymbol{\eta}|\boldsymbol{\epsilon}} = \frac{\sigma_n^2}{2\alpha^2} \left[\boldsymbol{\Phi}_{\mathrm{co}}(\boldsymbol{\eta}) + \frac{\Im\left\{\mathbf{a}(\boldsymbol{\eta})^H \frac{\partial \mathbf{a}(\boldsymbol{\eta})}{\partial \eta^{\mathrm{T}}}\right\}^{\mathrm{T}} \Im\left\{\mathbf{a}(\boldsymbol{\eta})^H \frac{\partial \mathbf{a}(\boldsymbol{\eta})}{\partial \boldsymbol{\eta}^{\mathrm{T}}}\right\}}{\|\mathbf{a}(\boldsymbol{\eta})\|^2} \right]^{-1} \tag{5.39}$$

$$= \frac{\sigma_n^2}{2\alpha^2} \left[\Re\left\{ \left(\frac{\partial \mathbf{a}(\boldsymbol{\eta})}{\partial \boldsymbol{\eta}^{\mathrm{T}}} \right)^H \Pi^{\perp}_{\mathbf{a}(\boldsymbol{\eta})} \frac{\partial \mathbf{a}(\boldsymbol{\eta})}{\partial \boldsymbol{\eta}^{\mathrm{T}}} \right\} + \frac{\Im\left\{\mathbf{a}(\boldsymbol{\eta})^H \frac{\partial \mathbf{a}(\boldsymbol{\eta})}{\partial \eta^{\mathrm{T}}}\right\}^{\mathrm{T}} \Im\left\{\mathbf{a}(\boldsymbol{\eta})^H \frac{\partial \mathbf{a}(\boldsymbol{\eta})}{\partial \boldsymbol{\eta}^{\mathrm{T}}}\right\}}{\|\mathbf{a}(\boldsymbol{\eta})\|^2} \right]^{-1}$$

$$= \frac{\sigma_n^2}{2\alpha^2} \left[\Re\left\{ \left(\frac{\partial \mathbf{a}(\boldsymbol{\eta})}{\partial \boldsymbol{\eta}^{\mathrm{T}}} \right)^H \frac{\partial \mathbf{a}(\boldsymbol{\eta})}{\partial \boldsymbol{\eta}^{\mathrm{T}}} \right\} + \frac{\Re\left\{\mathbf{a}(\boldsymbol{\eta})^H \frac{\partial \mathbf{a}(\boldsymbol{\eta})}{\partial \eta^{\mathrm{T}}}\right\}^{\mathrm{T}} \Re\left\{\mathbf{a}(\boldsymbol{\eta})^H \frac{\partial \mathbf{a}(\boldsymbol{\eta})}{\partial \boldsymbol{\eta}^{\mathrm{T}}}\right\}}{\|\mathbf{a}(\boldsymbol{\eta})\|^2} \right]^{-1}$$

$$= \frac{\sigma_n^2}{2\alpha^2} \left[\boldsymbol{\Phi}_{\mathrm{op}}(\boldsymbol{\eta}) \right]^{-1}, \tag{5.40}$$

and

$$\lim_{\sigma_{n_a}^2 \to 0} \mathbf{CRB}_{\boldsymbol{\varphi}|\boldsymbol{\epsilon}} = \mathbf{0}, \quad \lim_{\sigma_{n_a}^2 \to 0} \mathbf{CRB}_{\boldsymbol{\eta},\boldsymbol{\varphi}|\boldsymbol{\epsilon}} = \mathbf{0}. \tag{5.41}$$

The CRB for $\boldsymbol{\eta}$ parameter in (5.40) matches that of (4.28), which represents the theoretical optimum achievable with perfect phase compensation.

5.4.2 Closed-form expression

The closed-form CRB expressions for the present scenario build upon the mathematical framework developed in Sec. 4.4.1. The matrix formulations involving $\mathbf{Q}$, $\mathbf{v}$, $\mathbf{W}$, $\mathbf{w}$ and the associated variants, i.e. for narrow-band and delay-only cases, remain identical, as the signal structure and derivative computations are unchanged by the presence of phase uncertainty.

The fundamental modification appears in the final CRB expression, where the phase uncertainty manifests through an additional term in the FIM. Using the formulation established for the perfect compensation case, the CRB for the phase uncertainty framework becomes,

$$\mathbf{CRB}_{\boldsymbol{\eta}|\boldsymbol{\epsilon}} = \frac{f_s w_1}{2\mathrm{SNR}_{\mathrm{out}}} \left(\Re\left\{\mathbf{Q}\mathbf{W}\mathbf{Q}^H\right\} - \frac{\Re\left\{(\mathbf{Q}\mathbf{w})^H(\mathbf{Q}\mathbf{w})\right\}^T}{w_1} + \frac{\Im\left\{(\mathbf{Q}\mathbf{w})^H(\mathbf{Q}\mathbf{w})\right\}^T}{w_1(1+2\sigma_{n_a}^2\mathrm{SNR}_{\mathrm{out}})} \right)^{-1}.$$

5.4.3 Analysis of Global Phase Estimation

The global phase $\phi = \varphi - 2\pi f_c \tau$ combines hardware-induced and propagation-induced phase components. This formulation corresponds to rearranging the signal model in equation (5.1) by explicitly factoring the time-delay dependent carrier-phase term $e^{-j2\pi f_c \tau}$ from $\psi(\boldsymbol{\eta})$ and grouping it with the hardware phase φ, while maintaining τ as a separate parameter within $\boldsymbol{\eta}$. The CRB for the global phase derives from the linear transformation

$$\phi = \varphi - 2\pi f_c \tau = \begin{bmatrix} 1 \\ \boldsymbol{\lambda} \end{bmatrix}^T \boldsymbol{\theta}, \quad \boldsymbol{\lambda} = \begin{bmatrix} -2\pi f_c \\ \mathbf{0} \end{bmatrix} = -2\pi f_c \mathbf{e}_1, \quad \mathbf{e}_1 = \begin{bmatrix} 1 \\ \mathbf{0} \end{bmatrix}. \tag{5.42}$$

Application of the covariance transformation formula yields

$$\mathbf{CRB}_{\phi|\boldsymbol{\epsilon}} = \begin{bmatrix} 1 \\ \boldsymbol{\lambda} \end{bmatrix}^T \mathbf{CRB}_{\boldsymbol{\theta}|\boldsymbol{\epsilon}} \begin{bmatrix} 1 \\ \boldsymbol{\lambda} \end{bmatrix} = \begin{bmatrix} 1 \\ \boldsymbol{\lambda} \end{bmatrix}^T \begin{bmatrix} \mathbf{CRB}_{\boldsymbol{\varphi}|\boldsymbol{\epsilon}} & \mathbf{CRB}_{\boldsymbol{\eta},\boldsymbol{\varphi}|\boldsymbol{\epsilon}}^T \\ \mathbf{CRB}_{\boldsymbol{\eta},\boldsymbol{\varphi}|\boldsymbol{\epsilon}} & \mathbf{CRB}_{\boldsymbol{\eta}|\boldsymbol{\epsilon}} \end{bmatrix} \begin{bmatrix} 1 \\ \boldsymbol{\lambda} \end{bmatrix}. \tag{5.43}$$

Matrix multiplication produces

$$\mathbf{CRB}_{\phi|\boldsymbol{\epsilon}} = \mathbf{CRB}_{\varphi|\boldsymbol{\epsilon}} + \mathbf{CRB}^T_{\boldsymbol{\eta},\varphi|\boldsymbol{\epsilon}}\boldsymbol{\lambda} + \boldsymbol{\lambda}^T\mathbf{CRB}_{\boldsymbol{\eta},\varphi|\boldsymbol{\epsilon}} + \boldsymbol{\lambda}^T\mathbf{CRB}_{\boldsymbol{\eta}|\boldsymbol{\epsilon}}\boldsymbol{\lambda} \tag{5.44}$$

$$= \mathbf{CRB}_{\varphi|\boldsymbol{\epsilon}} + 2\boldsymbol{\lambda}^T\mathbf{CRB}_{\boldsymbol{\eta},\varphi|\boldsymbol{\epsilon}} + \boldsymbol{\lambda}^T\mathbf{CRB}_{\boldsymbol{\eta}|\boldsymbol{\epsilon}}\boldsymbol{\lambda}. \tag{5.45}$$

Substituting $\boldsymbol{\lambda} = -2\pi f_c \mathbf{e}_1$ yields

$$\mathbf{CRB}_{\phi|\boldsymbol{\epsilon}} = \mathbf{CRB}_{\varphi|\boldsymbol{\epsilon}} - 4\pi f_c \mathbf{e}_1^T\mathbf{CRB}_{\boldsymbol{\eta},\varphi|\boldsymbol{\epsilon}} + (2\pi f_c)^2\mathbf{e}_1^T\mathbf{CRB}_{\boldsymbol{\eta}|\boldsymbol{\epsilon}}\mathbf{e}_1. \tag{5.46}$$

Under the limiting case $\sigma^2_{n_a} \to \infty$, substituting the cross-term from equation (5.35b)

$$\mathbf{CRB}_{\phi|\boldsymbol{\epsilon}} = \mathbf{CRB}_{\varphi|\boldsymbol{\epsilon}} - \frac{4\pi f_c}{\|\mathbf{a}(\boldsymbol{\eta})\|^2}\mathbf{e}_1^T\Im\left\{\mathbf{a}(\boldsymbol{\eta})^H\frac{\partial\mathbf{a}(\boldsymbol{\eta})}{\partial\boldsymbol{\eta}^T}\right\}^T\mathbf{CRB}_{\boldsymbol{\eta}|\boldsymbol{\epsilon}} + (2\pi f_c)^2\mathbf{e}_1^T\mathbf{CRB}_{\boldsymbol{\eta}|\boldsymbol{\epsilon}}\mathbf{e}_1. \tag{5.47}$$

The derivative relationships for the time-delay signal model are

$$\frac{\partial\mathbf{a}(\boldsymbol{\eta})}{\partial\boldsymbol{\eta}^T} = \left(-\mathbf{c}(\boldsymbol{\eta})j2\pi f_c\mathbf{e}_1 + \frac{\partial\mathbf{c}(\boldsymbol{\eta})}{\partial\boldsymbol{\eta}^T}\right)e^{-j2\pi f_c\tau}, \tag{5.48a}$$

$$\mathbf{a}(\boldsymbol{\eta})^H\frac{\partial\mathbf{a}(\boldsymbol{\eta})}{\partial\boldsymbol{\eta}^T} = -\|\mathbf{c}(\boldsymbol{\eta})\|^2 j2\pi f_c\mathbf{e}_1^T + \mathbf{c}(\boldsymbol{\eta})^H\frac{\partial\mathbf{c}(\boldsymbol{\eta})}{\partial\boldsymbol{\eta}^T}. \tag{5.48b}$$

Using $\|\mathbf{a}(\boldsymbol{\eta})\|^2 \equiv \|\mathbf{c}(\boldsymbol{\eta})\|^2$, equation (5.47) becomes,

$$\mathbf{CRB}_{\phi|\boldsymbol{\epsilon}} = \mathbf{CRB}_{\varphi|\boldsymbol{\epsilon}} + \frac{4\pi f_c}{\|\mathbf{c}(\boldsymbol{\eta})\|^2}\mathbf{e}_1^T\Im\left\{\mathbf{c}(\boldsymbol{\eta})^H\frac{\partial\mathbf{c}(\boldsymbol{\eta})}{\partial\boldsymbol{\eta}^T}\right\}^T\mathbf{CRB}_{\boldsymbol{\eta}|\boldsymbol{\epsilon}} - (2\pi f_c)^2\mathbf{e}_1^T\mathbf{CRB}_{\boldsymbol{\eta}|\boldsymbol{\epsilon}}\mathbf{e}_1. \tag{5.49}$$

Expressing $\mathbf{CRB}_{\varphi|\boldsymbol{\epsilon}}$ from equation (5.37c) using equation (5.48)

$$\begin{aligned}\mathbf{CRB}_{\varphi|\boldsymbol{\epsilon}} = \frac{1}{2\mathrm{SNR}_{\mathrm{out}}} &+ \frac{1}{\|\mathbf{c}(\boldsymbol{\eta})\|^4}\Im\left\{\mathbf{c}(\boldsymbol{\eta})^H\frac{\partial\mathbf{c}(\boldsymbol{\eta})}{\partial\boldsymbol{\eta}^T}\right\}\mathbf{CRB}_{\boldsymbol{\eta}|\boldsymbol{\epsilon}}\Im\left\{\mathbf{c}(\boldsymbol{\eta})^H\frac{\partial\mathbf{c}(\boldsymbol{\eta})}{\partial\boldsymbol{\eta}^T}\right\}^T \\ &- \frac{4\pi f_c}{\|\mathbf{c}(\boldsymbol{\eta})\|^2}\Im\left\{\mathbf{c}(\boldsymbol{\eta})^H\frac{\partial\mathbf{c}(\boldsymbol{\eta})}{\partial\boldsymbol{\eta}^T}\right\}\mathbf{CRB}_{\boldsymbol{\eta}|\boldsymbol{\epsilon}}\mathbf{e}_1 + (2\pi f_c)^2\mathbf{e}_1^T\mathbf{CRB}_{\boldsymbol{\eta}|\boldsymbol{\epsilon}}\mathbf{e}_1.\end{aligned} \tag{5.50}$$

Substituting equation (5.50) into equation (5.49) produces systematic cancellation of carrier frequency-dependent terms, yielding

$$\mathbf{CRB}_{\phi|\boldsymbol{\epsilon}} = \frac{1}{2\mathrm{SNR}_{\mathrm{out}}} + \frac{1}{\|\mathbf{c}(\boldsymbol{\eta})\|^4}\Im\left\{\mathbf{c}(\boldsymbol{\eta})^H\frac{\partial\mathbf{c}(\boldsymbol{\eta})}{\partial\boldsymbol{\eta}^T}\right\}\mathbf{CRB}_{\boldsymbol{\eta}|\boldsymbol{\epsilon}}\Im\left\{\mathbf{c}(\boldsymbol{\eta})^H\frac{\partial\mathbf{c}(\boldsymbol{\eta})}{\partial\boldsymbol{\eta}^T}\right\}^T. \tag{5.51}$$

By comparing $\mathbf{CRB}_{\phi|\boldsymbol{\epsilon}}$ in (5.51) against $\mathbf{CRB}_{\varphi|\boldsymbol{\epsilon}}$ in (5.50), one observes that $\mathbf{CRB}_{\phi|\boldsymbol{\epsilon}}$ lacks the $(2\pi f_c)^2$ and $(4\pi f_c)$ amplification terms affecting $\mathbf{CRB}_{\varphi|\boldsymbol{\epsilon}}$, which causes the resulting CRB to increase the value of the variance it designates, providing theoretical justification for conventional approaches that estimate combined phase parameters.

Comparing equation (5.51) with the conventional global phase bound in equation (3.26c) from Section 3.5.2, the key distinction lies in which phase terms are incorporated. The conventional formulation absorbs the hardware phase φ into the complex amplitude $\tilde{\alpha} = \alpha e^{j(\varphi - \omega_c\tau)}$ and defines the global phase as the Doppler-induced component $\phi = \omega_c b(t-\tau)$. In contrast, equation (5.51) defines $\phi = \varphi - 2\pi f_c\tau$, incorporating both hardware-induced and time-delay dependent carrier-phase terms. The systematic cancellation of $(2\pi f_c)^2$ amplification terms in equation (5.51) produces a bound that depends only on baseband correlation terms, avoiding the carrier frequency-squared degradation that appears in equation (3.26c). This results in significantly lower bounds for global phase estimation when auxiliary phase measurements are available, demonstrating the theoretical advantage of this phase combination.

5.5 Simulation Results and Discussion

The theoretical framework developed in preceding sections is evaluated using the simulation methodology established in Section 4.6, employing the same GPS L1 C/A and Kasami sequence configurations to enable direct comparison with the perfect compensation results from Chapter 4. This section first presents the delay-only model simplification that eliminates Doppler-induced complexity for computational purposes, while preserving the essential carrier-phase structure, then examines the practical scenario where auxiliary phase measurements contain quantifiable uncertainty characterized by $\sigma_{n_a}^2 > 0$.

5.5.1 Delay-only Model Simplification

For scenarios where auxiliary propagation parameters can be neglected or independently compensated, the general framework reduces to a computationally tractable form. When platform motion is negligible or Doppler effects have been separately estimated and removed, setting $b = 0$ simplifies the parameter vector from $\boldsymbol{\eta} = [\tau, b]^{\mathrm{T}}$ to the scalar delay parameter $\eta = \tau$. The complete parameter set becomes,

$$\boldsymbol{\epsilon} = [\sigma_n^2, \alpha, \boldsymbol{\theta}^{\mathrm{T}}]^{\mathrm{T}}, \quad \boldsymbol{\theta} = [\varphi, \tau]^{\mathrm{T}} \tag{5.52}$$

Under this static assumption, the signal model simplifies to

$$\mathbf{a}(\tau) = \mathbf{c}(t - \tau)e^{-j\omega_c \tau} \tag{5.53}$$

This reduction preserves the essential carrier-phase structure while eliminating the computational burden associated with multi-parameter optimization. The simplified model facilitates detailed analysis of carrier-phase effects on time-delay estimation without confounding influences from Doppler dynamics, forming the basis for the numerical validations presented in subsequent sections.

The following analysis employs this simplified framework to systematically evaluate the impact of phase measurement uncertainty on estimation performance.

5.5.2 Impact of Phase Uncertainty on Theoretical Bounds

Figure 5.2 illustrates the fundamental relationship between phase measurement uncertainty $\sigma_{n_a}^2$ and achievable estimation accuracy through four CRB^f realizations. The systematic variation of $\sigma_{n_a}^2 = \{-40, -30, -20, -10\}$ radians expressed in decibels, reveals the progressive degradation of performance bounds as calibration quality decreases. For the Kasami sequence configuration, the plateau RMSE level exhibits a 1:1 correspondence with phase uncertainty, where each 10 dB increase in $\sigma_{n_a}^2$ elevates the plateau by approximately 10 dB RMSE, establishing a direct quantitative relationship between phase measurement quality and ranging precision limits. The three distinct operational regimes observed in Figure 5.2 arise from the mathematical structure of equation (5.34a). At low $\mathrm{SNR_o}$ut, the additional term beyond $\boldsymbol{\Phi}_{\mathrm{co}}(\boldsymbol{\eta})$ in (5.34b) contributes significantly to the FIM due to the small denominator $(1 + 2\sigma_{n_a}^2 \mathrm{SNR}_{\mathrm{out}})$, causing CRB^f to align with CRB^o, as predicted in (5.40). In this regime, the MLE converges to the main lobe of the Dirac comb structure shown in Figures 4.6, as the $\sigma_{n_a}^2$ remains negligible compared to the SNR. As $\mathrm{SNR}_{\mathrm{out}}$ increases, the denominator $(1 + 2\sigma_{n_a}^2 \mathrm{SNR}_{\mathrm{out}})$ grows linearly, causing the additional term's contribution to the FIM to decrease at rate 1/SNR. In the intermediate $\mathrm{SNR}_{\mathrm{out}}$ regime, the MLE exhibits plateau behavior, converging to CRB^f which remains at a relatively constant error level over a range of $\mathrm{SNR}_{\mathrm{out}}$ values. From the AF perspective, the plateau region corresponds to the MLE detaching from the main lobe and jumping between neighboring peaks separated by $\Delta\tau = 1/(2f_c)$, as illustrated in Figure 4.6. The amplified phase uncertainty prevents reliable lobe distinction, causing random selections that average to the plateau level, where phase uncertainty

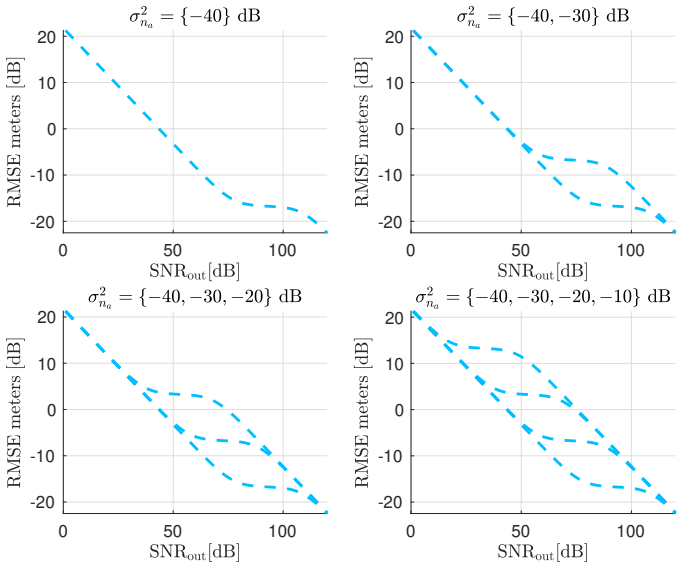

Figure 5.2: Progressive CRB^f realizations for $\sigma^2_{n_a} = \{-40, -30, -20, -10\}$ dB demonstrating the systematic degradation of theoretical bounds with increasing phase uncertainty. Greater uncertainty causes earlier plateau onset, with the plateau RMSE level increasing proportionally at a 1:1 ratio with phase uncertainty for the Kasami sequence configuration.

becomes the fundamental limitation. The plateau level and SNR_{out} range depend on both $\sigma^2_{n_a}$ and the signal configuration.

At sufficiently high SNR_{out} where $(1+2\sigma^2_{n_a}\text{SNR}_{\text{out}}) \to \infty$, the additional term vanishes causing CRB^f to converge toward CRB^m, leaving only $\boldsymbol{\Phi}_{\text{co}}(\boldsymbol{\eta})$ from (5.34b), as shown in (5.37b). Phase uncertainty is amplified such that the MLE can no longer resolve individual lobes within the comb structure (see Figure 4.6). The estimator responds only to the broader envelope of the baseband AF $\Xi_0(\tau';\tau)$, whose curvature is characterized by CRB^m. The fine structure created by the carrier-phase term $\cos^2(2\pi f_c d\tau)$ becomes effectively masked, returning the system to conventional estimation performance where carrier-phase information provides no benefit beyond what the baseband signal structure already offers.

5.5.3 Validation Under CSM conditions

Figures 5.3b and 5.3a validate the mathematical correctness of the derived CRB and MLE expressions through enforced CSM conditions. By maintaining $\sigma^2_{n_a} = \kappa/\text{SNR}_{\text{out}}$ with $\kappa = \{0.10, 0.60, 1.09\}$, the simulations demonstrate asymptotic convergence of $\widehat{\tau}$ to its corresponding CRB across all SNR_{out} levels, confirming the theoretical derivations from Section 5.3. The upper bound $\kappa = 1.09$ ensures that even at the lowest simulated SNR_{out} values, $\sigma_{n_a} = \sqrt{\kappa/\text{SNR}_{\text{out}}} \approx 1.04$ rad remains sufficiently below $\pi \approx 3.14$ rad, maintaining validity of the linear Gaussian approximation rather than requiring circular distributions. The three selected κ values provide distinct CRB levels to validate the theoretical expressions across different phase uncertainty regimes while maintaining the CSM framework.

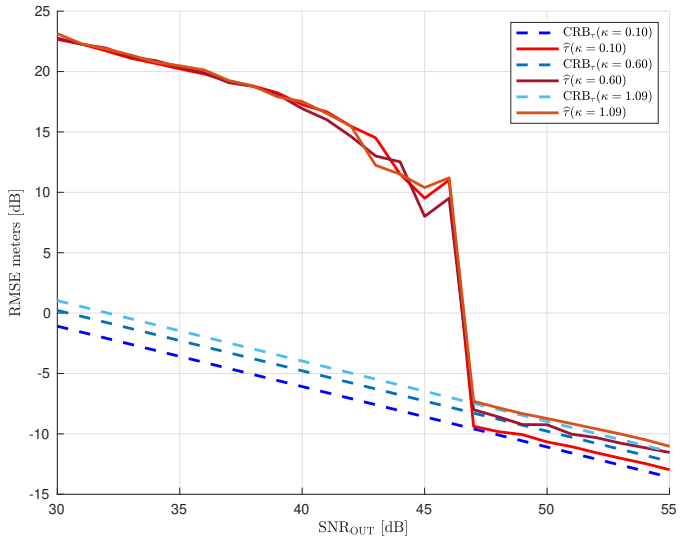

(**a**)

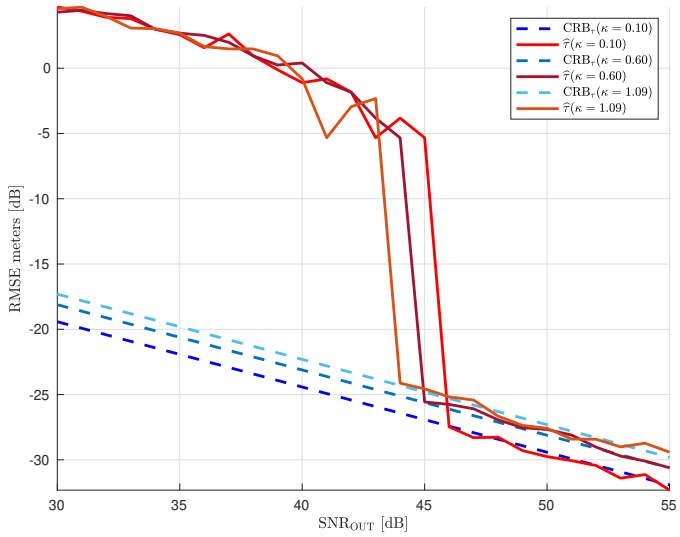

(**b**)

Figure 5.3: Validation of CRB and MLE expressions under CSM conditions for (a) Kasami and (b) GPS L1 C/A signal configurations. The convergence of $\widehat{\tau}$ simulated for $\kappa = \{0.10, 0.60, 1.09\}$ to the associated CRB confirms the asymptotic efficiency behavior of the MLE.

5.5.4 Estimator Performance Comparison

Figures 5.4a and 5.4b compare the three estimation approaches under fixed phase uncertainty $\sigma^2_{n_a}$. At low $\mathrm{SNR}_{\mathrm{out}}$, all estimators converge to CRB^m as noise masks the phase information. As $\mathrm{SNR}_{\mathrm{out}}$ increases beyond the initial threshold, the estimators diverge: $\widehat{\tau}_o$ progresses toward CRB^o, while both $\widehat{\tau}_n$ and $\widehat{\tau}$ exhibit plateau behavior at an error level consistent with CRB^f. The observed plateau behavior of the MLE demonstrates convergence to CRB^f throughout the intermediate $\mathrm{SNR}_{\mathrm{out}}$ regime. At sufficiently high $\mathrm{SNR}_{\mathrm{out}}$, a critical transition occurs where the naive and phase-aware estimators begin to exhibit different behavior. The phase-aware estimator $\widehat{\tau}$, through its statistical treatment of phase uncertainty, begins to depart from the plateau and converges back to CRB^m toward improved performance, while the naive estimator $\widehat{\tau}_n$ remains bounded by the plateau level. This divergence demonstrates that sophisticated phase uncertainty characterization provides tangible benefits only beyond a defined $\mathrm{SNR}_{\mathrm{out}}$ threshold, establishing a criteria for when computational complexity is justified.

Figure 5.5 extends the $\mathrm{SNR}_{\mathrm{out}}$ range to reveal the long-term behavior of the estimators. The testing setup was modified by increasing the oversampling factor by 30, at the cost of increased simulation time and computational resources, to enhance sample resolution over the main lobes and enable analysis of MLE behavior over an extended $\mathrm{SNR}_{\mathrm{out}}$ range. Beyond a critical $\mathrm{SNR}_{\mathrm{out}}$ value, both $\widehat{\tau}_n$ and $\widehat{\tau}$ detach from their respective bounds to form plateaus. This detachment occurs because the fifth-order Taylor expansion used in formulating the MLE in (5.17) no longer provides sufficient accuracy for the fine resolution levels required at high $\mathrm{SNR}_{\mathrm{out}}$. Incorporating higher-order terms in the expansion would extend the region where the estimators attain their bounds. The optimal estimator $\widehat{\tau}_o$ also exhibits degraded performance at the highest simulated $\mathrm{SNR}_{\mathrm{out}}$ levels, indicating that this limitation affects all phase-aware estimators when resolution requirements exceed the approximation accuracy.

The phase estimation performance directly impacts the achievable time-delay accuracy, as the phase error $\varepsilon = \varphi - x_a$ determines the effectiveness of carrier-phase exploitation. Figures 5.6a and 5.6b illustrate the behavior of the phase estimator $\widehat{\varphi}$ under different calibration uncertainty levels. The phase estimators exhibit convergence to their respective $\mathrm{CRB}_{\varphi|\boldsymbol{\epsilon}}$ at the plateau level determined by the calibration uncertainty $\sigma^2_{n_a}$. While the theoretical bounds for different uncertainty values eventually saturate toward a linear decaying RMSE at high $\mathrm{SNR}_{\mathrm{out}}$, the practical estimators remain fixed at the error level established by the initial plateau. This behavior indicates that the phase estimation accuracy is fundamentally limited by the calibration quality rather than the available $\mathrm{SNR}_{\mathrm{out}}$, with direct implications for time-delay estimation performance.

The relationship between phase calibration accuracy and time-delay performance becomes evident when comparing the plateau levels across both sets of figures. The phase estimation error directly translates to a degradation in time-delay accuracy, with the factor $(1 + 2\sigma^2_{n_a}\mathrm{SNR}_{\mathrm{out}})^{-1}$ establishing the quantitative relationship. The phase-aware estimator enables sub-meter ranging accuracy at $\mathrm{SNR}_{\mathrm{out}}$ levels beyond approximately 42 dB for a phase uncertainty of $\sigma^2_{n_a} = -20$ dB, when it converges to $\mathrm{CRB}^f_{\tau|\boldsymbol{\epsilon}}$, representing a significant improvement over the conventional approach which requires $\mathrm{SNR}_{\mathrm{out}}$ levels exceeding 80 dB to achieve comparable performance. This reduction in required SNR demonstrates the practical benefit of incorporating phase information even with imperfect calibration, though the sub-centimeter accuracy target necessitates further refinement of calibration techniques, signal configuration optimization, and operation at elevated SNR levels. For the basic signal configurations employed in this analysis with $\mathrm{F_c}$ and $\mathrm{F_s}$ factors equal to 1 and phase uncertainty of $\sigma^2_{n_a} = -20$ dB, sub-centimeter accuracy is only achievable for the longer GPS L1 C/A sequence at very high $\mathrm{SNR}_{\mathrm{out}}$ ranges, reaching approximately 1 cm RMSE at 100 dB $\mathrm{SNR}_{\mathrm{out}}$, close to the highest value simulated. The shorter Kasami sequence achieves approximately 5 dm RMSE under the same conditions.

This demonstrates that careful signal setup consideration should be undertaken, involving sequence length, F_s and F_c factors, and selection of code sequences with properties more adapted to the target accuracy requirements, to allow sub-centimeter accuracy to be reached at lower SNR_{out} regimes.

5.6 Conclusion

This chapter addressed practical scenarios where hardware-induced phase offsets are observed through auxiliary measurements containing quantifiable uncertainty. Building upon the identifiability conditions applied to the CSM framework established in Chapter 3, which demonstrated that both hardware-related and propagation-induced phase components can be uniquely determined, this chapter developed estimation frameworks that explicitly incorporate auxiliary phase measurements for compensation with characterized uncertainty.

To this end, CRB and MLE expressions were derived that account for phase measurement uncertainty. The phase-aware MLE incorporates uncertainty characterization through polynomial cost function optimization. This estimator was compared against the optimal estimator assuming perfect phase compensation and a naive approach that avoids computational complexity by directly compensating the phase term with available observables without accounting for their statistical uncertainty. The derived CRB equation shows dependence on the quality of the calibration process that generated the auxiliary observations, and two limit cases were analyzed based on the limit values of this uncertainty. When the uncertainty tends to infinity, the CRB aligns with that of the conventional case, which grouped hardware and propagation-induced components into a complex amplitude. For zero uncertainty, the CRB aligns with the optimal bound, which assumed complete hardware-induced phase compensation.

Monte Carlo simulations validate the theoretical predictions. The derived MLE attains its corresponding CRB, which transitions from the optimal bound through a plateau region before converging toward the conventional bound as the observable uncertainty is amplified by increasing SNR. At high SNR, the MLE detaches from its bound to form a second plateau, because the fifth-order Taylor expansion used in its formulation no longer provides sufficient accuracy for the fine resolution levels required in this regime.

The first plateau RMSE level encompasses a wide range of the simulated SNR regime. Both the MLE and its CRB exhibit a 1:1 correspondence with phase uncertainty, showing a 10 dB RMSE degradation for every 10 dB increase in uncertainty. Additionally, for the same 10 dB decrease in calibration quality, the plateau onset shifts toward lower SNR values by over 20 dB. These results demonstrate that higher calibration accuracy on auxiliary phase observables allows the MLE to remain efficient over a wider SNR range while achieving lower error levels.

The connection to the AF, which revealed a fine comb structure sampling the conventional bound, shows that the plateau region corresponds to the MLE jumping between neighboring peaks of the true maximum, with amplified phase uncertainty preventing reliable lobe distinction.

The framework quantifies the performance difference between conventional code-based estimation and optimal carrier-phase enhanced approaches, establishing the range of operations where additional complexity of the statistical treatment of auxiliary phase information is justifiable over naive approaches. For the setup used in simulations, the phase-aware estimator shows the same performance as the naive approach up to a defined SNR level, well after convergence, which depends on the simulation configuration considered. Only for higher SNR regimes, does the sophistication prove worthwhile as the phase-aware MLE improves with increasing SNR, separating progressively from the constant naive implementation which remains at the plateau level.

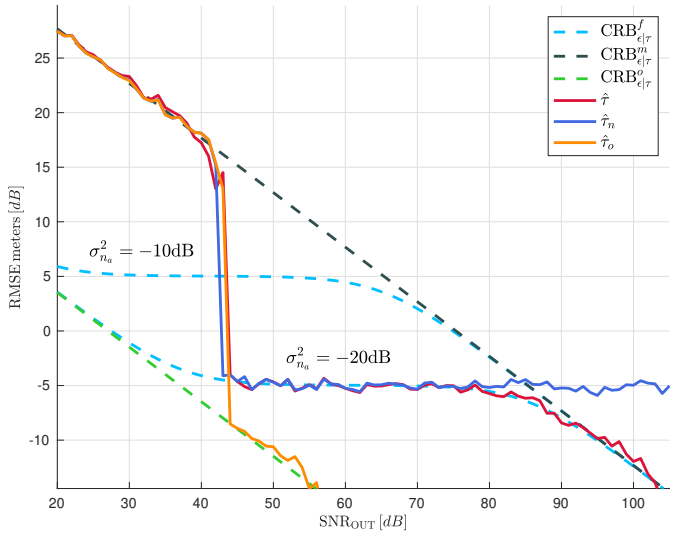

(**a**)

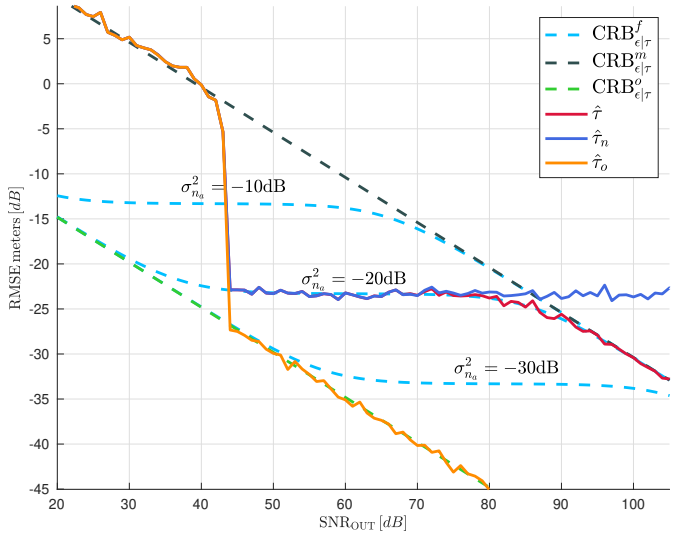

(**b**)

Figure 5.4: Comparative performance of naive, phase-aware, and optimal estimators for (a) Kasami and (b) GPS L1 C/A configurations under fixed phase uncertainty $\sigma^2_{n_a}$. Both naive and phase-aware approaches exhibit similar plateau behavior determined by the phase measurement uncertainty.

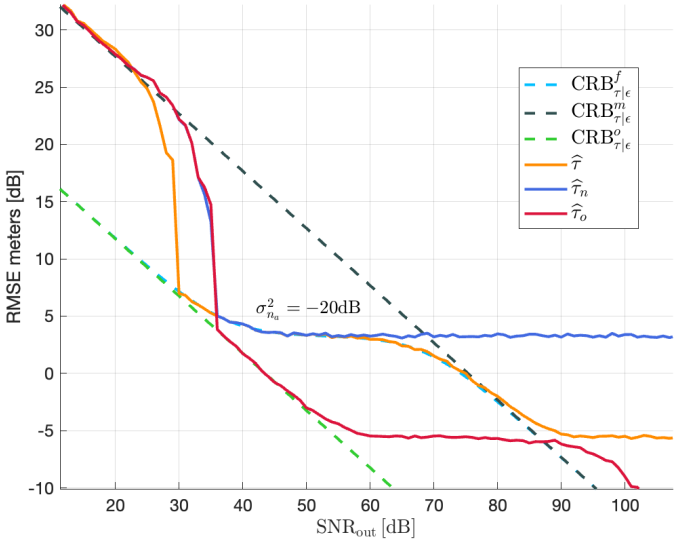

Figure 5.5: MLEs and CRBs simulated for a Kasami sequence over an extended range of SNR_{out} values, showing that beyond a certain SNR_{out} value, both $\widehat{\tau}_o$ and $\widehat{\tau}$ detach from their respective bounds to form a plateau. This behavior arises because the Taylor expansion order used in equation (5.17) to formulate the MLEs no longer provides sufficient accuracy for the fine resolution levels required at high SNR_{out}, causing the phase-aware estimator $\hat{\tau}$ to deviate from $\text{CRB}^m_{\tau|\epsilon}$.

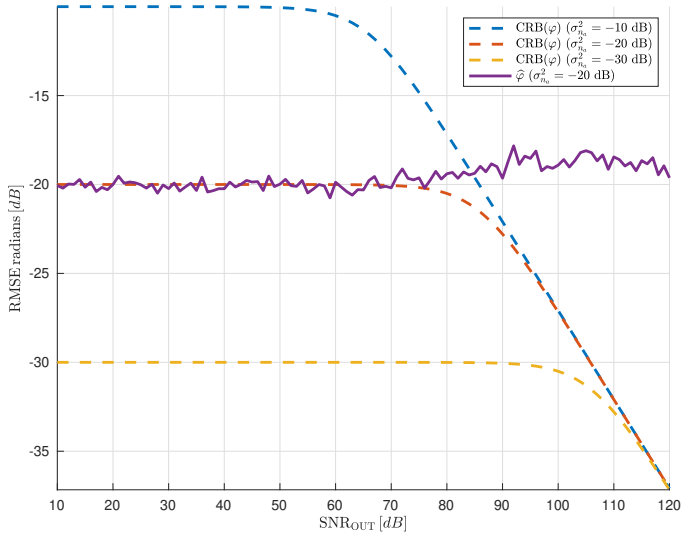

(**a**)

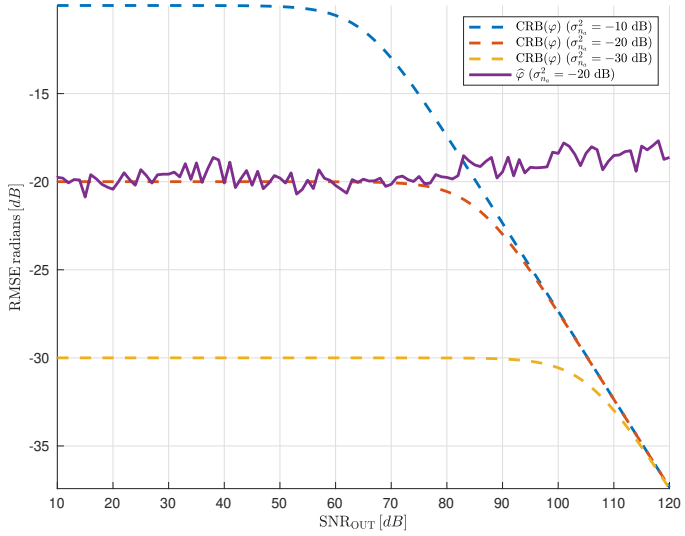

(**b**)

Figure 5.6: Comparative performance of the estimator of the phase $\hat{\varphi}$ for (a) GPS L1 C/A and (b) Kasami configurations under fixed phase uncertainty $\sigma^2_{n_a}$. Both estimators remain aligned with the corresponding CRB for the associated $\sigma^2_{n_a}$, at the same error level of -20dB meters. However, while all CRB simulated for different uncertainty values saturate towards a linear decaying RMSE, the estimators remain at the error level defined by the initial plateau.

Chapter 6

Conclusion and Future Work

6.1 Conclusion

This thesis developed a theoretical framework for carrier-phase enhanced time-delay estimation to achieve centimeter-level inter-satellite ranging accuracy required for the NOIRE mission. Building upon well-established time-delay estimation assessments where hardware-induced and time-delay dependent phase terms were grouped into complex amplitude due to belief they were not independently identifiable, this work demonstrated through identifiability analysis that these phase components are indeed separable. This finding enabled development of compensation strategies for equipment-related phase terms, allowing time-delay dependent carrier-phase information to be explicitly exploited in signal models for improved characterization and potentially tighter variance bounds. The research analyzed two enhanced scenarios beyond conventional approaches: perfect hardware phase compensation representing the theoretical optimum, and realistic scenarios with quantifiable phase measurement uncertainty.

The optimal phase compensation analysis established theoretical performance limits achievable when hardware-induced phase is perfectly known. The derived CRB expressions revealed orders-of-magnitude improvements over conventional bounds, with quadratic dependence on carrier frequency confirming that the supplementary phase terms are not negligible. The AF analysis demonstrated a characteristic comb structure where narrow lobes, spaced at intervals determined by carrier frequency, sample the conventional baseband AF. This structure explains why SNR must exceed specific thresholds before the MLE can distinguish between primary and secondary lobes to converge correctly. The comprehensive MLE characterization revealed five distinct operational regions, extending the previously known three-region model by identifying additional transitional zones. For joint delay-doppler estimation in dynamic scenarios, the analysis quantified an approximately 4 dB RMSE degradation for time-delay estimation, compared to delay-only cases. Doppler estimation exhibits approximately 6 dB RMSE degradation. These penalties represent the cost of statistical coupling between parameters introduced by simultaneous estimation under carrier-phase enhanced processing.

The phase uncertainty framework addressed practical scenarios where hardware phase calibration contains measurement errors. Incorporating auxiliary phase observables with Gaussian-distributed uncertainty, valid for sufficiently small phase ranges, modified both CRB and MLE structures. The naive estimator, which directly applies phase measurements without statistical consideration, provided a reference for assessing when sophisticated processing justifies its complexity. The CRB behavior transitions from the optimal bound through a plateau determined by calibration uncertainty, eventually converging toward the conventional bound as the CRB factor

depending on phase uncertainty modulates performance. At higher SNR values, the Taylor expansion order used in formulating the MLE no longer provides sufficient accuracy for the increasingly fine resolution required, limiting the estimator performance and causing it to deviate from the bound and form a second plateau.

fifth-order Taylor expansion used in deriving the CRB becomes insufficiently accurate, causing the phase-aware MLE to detach from its bound and form a second permanent plateau. Incorporating higher-order terms in the expansion would extend the region of validity.

Throughout the first plateau region, naive and phase-aware estimators perform equivalently, with sophisticated processing providing benefits only near the transition where the bound converges toward conventional performance before detachment occurs.

These results provide quantitative guidelines for system design decisions in precision ranging applications. The framework establishes when carrier-phase exploitation offers practical advantages, identifying SNR thresholds and calibration requirements necessary to achieve specific accuracy targets. The equivalence of estimators across operational regions informs implementation strategies, suggesting adaptive approaches that reserve complex processing for conditions where tangible benefits exist. For the NOIRE mission, achieving centimeter-level accuracy requires both elevated SNR levels and precise phase calibration, with the derived expressions providing explicit design specifications. This comprehensive characterization connects theoretical performance limits with practical constraints, enabling the transition from conventional ranging to carrier-phase enhanced techniques in distributed systems.

6.2 Future Work

The theoretical framework developed in this thesis enables carrier-phase enhanced time-delay estimation, deriving performance bounds and estimators under various phase compensation scenarios. Several research directions remain to be explored to bridge the gap between theoretical analysis and practical implementation, extend the framework to networked systems, and characterize robustness under model uncertainties.

6.2.1 Evaluation of tailored signals

In future work, it would be highly relevant to extend the analysis to more advanced signal designs that are better tailored to the specific requirements of NOIRE or similar swarm missions. While GPS and Kasami codes have been used as well-known references in this study, they were not specifically optimized for combined navigation and communication purposes. Recently, several novel NAVCOM-type signals have been proposed to enable both high-precision ranging and efficient data transmission within inter-satellite links. Among them, the PRN–CSS (Chirp Spread Spectrum) (Ortega 2022), PRN–Zadoff–Chu, and CSK (Chirp Shift Keying) modulations (Ortega 2021; Ortega 2019) stand out as promising candidates. These signals combine the spreading and correlation robustness of pseudo-random noise sequences with the orthogonality and constant-envelope properties of non-binary waveforms, enabling reliable performance even in interference-limited scenarios. In particular, PRN–CSS offers full orthogonality among symbols, PRN–Zadoff–Chu provides excellent autocorrelation and cyclic-shift reuse capabilities, and CSK allows flexible trade-offs between bandwidth, data rate, and complexity. A systematic evaluation of these tailored waveforms under realistic channel and swarm geometry conditions would therefore be an important step forward in future studies.

6.2.2 Comparison with Established TDE Methods

The time-delay estimation framework developed in this thesis derives from first principles using the CSM with explicit carrier-phase modeling, characterizing fundamental performance bounds when phase offsets are known with quantifiable uncertainty. The relationship between this approach and established methods in the positioning and navigation literature remains to be systematically characterized. The Lambda method (Teunissen 2006), widely adopted in GNSS carrier-phase positioning, addresses a complementary but distinct problem: resolving integer cycle ambiguities in carrier-phase measurements through decorrelation and integer least-squares techniques. The framework presented here does not address integer ambiguity resolution, instead characterizing the continuous estimation problem when phase offsets contain quantifiable uncertainty $\sigma^2_{n_a}$. These approaches operate at different system levels and address different aspects of carrier-phase exploitation.

A comparative study should clarify how these frameworks combine in practical systems. The theoretical bounds derived here establish the fundamental ranging accuracy achievable between individual satellite pairs when phase calibration provides partial knowledge with characterized uncertainty. These elemental ranging measurements would then serve as inputs to positioning algorithms that may employ Lambda-type methods if integer ambiguities arise from additional carrier-phase observables. Understanding how ranging variance at the elemental level propagates through network positioning algorithms would reveal whether the enhanced precision from carrier-phase exploitation justifies the additional system complexity for phase calibration and processing.

Furthermore, the developed framework could be extended to multi-carrier and meta-signal architectures (Das 2020a; Ortega 2020), where two or more coherent components are transmitted to improve the trade-off between ambiguity resolution and noise robustness. In such cases, the joint estimation of delay and phase across composite signals introduces coupling effects and cross-frequency constraints that are not captured by conventional single-carrier models. Comparing the proposed CSM-based framework with meta-signal processing techniques would thus provide deeper insight into how carrier-phase uncertainty and multi-frequency coherence jointly impact achievable ranging precision.

Beyond ambiguity resolution methods, comparison with correlation-based and subspace techniques would provide practical context. While the phase-aware MLE derived in Chapter 5 achieves theoretical optimality, its polynomial root-finding formulation may present computational challenges in resource-constrained platforms. Benchmarking against fast correlation-based methods or recursive estimation frameworks would quantify the performance-complexity trade-off, informing practical system design decisions for the NOIRE mission and similar applications.

6.2.3 Performance Assessment in Cooperative Positioning

The theoretical developments in this thesis establish fundamental limits for elemental ranging between satellite pairs under various phase compensation scenarios. However, the NOIRE mission requires determination satellite geometry through cooperative positioning, where multiple inter-satellite ranges are fused to estimate a set of satellite positions simultaneously. Extending the framework to this networked context represents a critical step toward operational implementation. The work in (Chaumette 2025) demonstrated that fundamental limits on achievable positioning precision depend on the variance of elemental distance measurements. Specifically, for fixed inter-agent distance variance σ^2_d, reducing position estimate variance σ^2_p cannot eliminate the MSE floor, establishing that improved elemental ranging accuracy directly enhances overall positioning performance. This result motivates systematic evaluation of how the carrier-phase enhanced ranging techniques developed here propagate through cooperative positioning algorithms. The

performance assessment should address how the different CRB formulations derived in this thesis, i.e. conventional, perfect phase compensation, and compensation with phase uncertainty, affect final constellation geometry accuracy. Additional considerations include the integration of such methodology together with cooperative positioning frameworks such as the EDM (Naouri 2021), particle filters, or factor graph optimization, which would demonstrate practical implementation pathways and validate whether carrier-phase enhanced ranging offer an interesting alternative, and moreover whether it enables the NOIRE constellation to achieve centimeter-level positioning accuracy.

6.2.4 Performance evaluation under model misspecification

The derivations of the CRB throughout this thesis have assumed that the considered signal model accurately represents physical observations, with the CSM and Gaussian noise underpinning all performance analyses. However, in practice, real-world systems invariably deviate from these idealized assumptions due to unmodeled propagation effects, hardware nonlinearities, or environmental variations. The misspecified estimation theory framework (Fortunati 2017; Fortunati 2024) extends classical estimation theory to characterize performance when the assumed model differs from the true data-generating process, thus offering a principled way to evaluate estimator robustness under model mismatch.

In the context of time-delay and carrier-phase estimation, several types of model misspecifications can be particularly relevant to the NOIRE mission:

- *Non-Gaussian noise environments:* The Gaussian noise assumption may not hold in realistic conditions, where interference, impulsive events, or colored noise spectra distort the nominal distribution. Such contamination often leads to heavy-tailed statistics or outlier-dominated behavior, for which standard MLEs become inefficient (Ortega 2024). Within the MCRB framework, the degradation introduced by non-Gaussianity can be formally quantified, and robust estimators such as M-estimators (Ortega 2025) can be employed to mitigate performance loss while preserving near-optimal behavior under nominal conditions.

- *Intra-system interference and NAVCOM signals:* As discussed in section 6.2.1, the NOIRE constellation is expected to employ NAVCOM-type signals (e.g., PRN–CSS) capable of supporting both high-accuracy ranging and data transmission. However, shorter spreading codes and simultaneous multi-satellite transmissions may increase the level of intra-system interference, effectively violating the Gaussian noise assumption and introducing structured contamination. The misspecified estimation framework allows quantifying these losses analytically (Ortega 2023), helping to design signal structures and receiver strategies (Lesouple 2024) that balance data throughput and ranging accuracy.

- *Multipath propagation and environmental effects:* Inter-satellite multipath propagation can introduce delayed replicas of the transmitted signal, generating distortions in both amplitude and phase. These effects yield deterministic model errors that can be captured by the MCRB through the Kullback–Leibler divergence between the assumed and true signal distributions (Lubeigt 2023a). Evaluating such scenarios with the phase-aware models developed in this thesis will provide insight into the robustness of the carrier-phase enhanced estimators.

Finally, it should be noted that computational and energetic constraints in the swarm may impose simplifications on receiver algorithms. For instance, Doppler estimation may be omitted in certain nodes to reduce computational load, effectively introducing deliberate model misspecification in exchange for lower complexity. Similar strategies have already been explored in the state of the art (McPhee 2023a; McPhee 2023b) of high-dynamic positioning systems, where additional

parameters such as acceleration or jerk significantly increase receiver complexity, leading designers to trade off model fidelity for computational feasibility. In this context, the misspecified CRB framework thus offers not only a tool for quantifying performance degradation due to unmodeled effects, but also a means of optimally balancing accuracy and complexity in resource-limited inter-satellite receivers.

6.2.5 Non-Gaussian Phase Observables

The phase uncertainty framework in Chapter 5 models auxiliary phase measurements with Gaussian distributed errors $n_a \sim \mathcal{N}(0, \sigma_{n_a}^2)$. This assumption enables straightforward CRB derivation through the SBF, yielding closed-form performance bounds. However, phase measurements are inherently circular quantities constrained to $[-\pi, \pi)$, and the linear Gaussian model provides adequate approximation only when phase uncertainty is sufficiently small such that $\sigma_{n_a} \ll \pi$. For larger phase uncertainties, circular probability distributions would more appropriately capture the wrapping behavior of angular measurements. The von Mises distribution (Mardia 2010) provides the circular analog of the Gaussian distribution, with a concentration parameter that controls the distribution width. As this concentration increases, the von Mises distribution converges to the Gaussian model, recovering the linear case as a limiting case. Reformulating the framework with Von Mises phase observables would require deriving the FIM through direct differentiation of the likelihood function (Morales-Aguirre ; Morales-Aguirre 2025), as the SBF applies specifically to Gaussian models. The resulting modified CRB expressions would characterize performance degradation when phase uncertainty exceeds the small phase regime, revealing thresholds beyond which carrier-phase information provides diminishing returns and informing practical calibration requirements for ranging systems where phase measurements may experience large uncertainties.

Appendix A

Derivation of the Cauchy–Schwarz Step

Starting from the equality between the noiseless signal models,

$$\alpha_1 e^{j\varphi_1}\mathbf{a}(\boldsymbol{\eta}_1) = \alpha_2 e^{j\varphi_2}\mathbf{a}(\boldsymbol{\eta}_2), \tag{A.1}$$

rearranging terms gives

$$\mathbf{a}(\boldsymbol{\eta}_1) = \mathbf{a}(\boldsymbol{\eta}_2)\,\frac{\alpha_2}{\alpha_1}e^{j(\varphi_2-\varphi_1)}. \tag{A.2}$$

Taking the Hermitian inner product of both sides of (A.2) with $\mathbf{a}(\boldsymbol{\eta}_2)$ yields

$$\mathbf{a}(\boldsymbol{\eta}_2)^H\mathbf{a}(\boldsymbol{\eta}_1) = \mathbf{a}(\boldsymbol{\eta}_2)^H\mathbf{a}(\boldsymbol{\eta}_2)\,\frac{\alpha_2}{\alpha_1}e^{j(\varphi_2-\varphi_1)}. \tag{A.3}$$

Since $\mathbf{a}(\boldsymbol{\eta}_2)^H\mathbf{a}(\boldsymbol{\eta}_2) = \|\mathbf{a}(\boldsymbol{\eta}_2)\|^2$, this becomes

$$\mathbf{a}(\boldsymbol{\eta}_2)^H\mathbf{a}(\boldsymbol{\eta}_1) = \|\mathbf{a}(\boldsymbol{\eta}_2)\|^2\,\frac{\alpha_2}{\alpha_1}e^{j(\varphi_2-\varphi_1)}. \tag{A.4}$$

Taking the modulus of both sides gives

$$\left|\mathbf{a}(\boldsymbol{\eta}_2)^H\mathbf{a}(\boldsymbol{\eta}_1)\right| = \|\mathbf{a}(\boldsymbol{\eta}_2)\|^2\,\frac{|\alpha_2|}{|\alpha_1|}. \tag{A.5}$$

From (A.2), the norm of $\mathbf{a}(\boldsymbol{\eta}_1)$ is

$$\|\mathbf{a}(\boldsymbol{\eta}_1)\| = \|\mathbf{a}(\boldsymbol{\eta}_2)\|\,\frac{|\alpha_2|}{|\alpha_1|}. \tag{A.6}$$

Substituting this into the previous equation leads to

$$\left|\mathbf{a}(\boldsymbol{\eta}_2)^H\mathbf{a}(\boldsymbol{\eta}_1)\right| = \|\mathbf{a}(\boldsymbol{\eta}_1)\|\,\|\mathbf{a}(\boldsymbol{\eta}_2)\|, \tag{A.7}$$

and normalizing both sides by the norms gives

$$\frac{\left|\mathbf{a}(\boldsymbol{\eta}_1)^H\mathbf{a}(\boldsymbol{\eta}_2)\right|}{\|\mathbf{a}(\boldsymbol{\eta}_1)\|\,\|\mathbf{a}(\boldsymbol{\eta}_2)\|} = 1, \tag{A.8}$$

which corresponds to equality in the Cauchy–Schwarz inequality, implying linear dependence of $\mathbf{a}(\boldsymbol{\eta}_1)$ and $\mathbf{a}(\boldsymbol{\eta}_2)$.

Appendix B

CRB Derivations

B.1 Fisher Information Matrix Derivation

This section derives the FIM from the SBF formulas in (2.13) for the signal models in (4.1) and (5.1).

B.1.1 Fisher Information Matrix Structure

The Fisher Information Matrix exhibits a block structure reflecting the parameter decomposition $\boldsymbol{\epsilon}^{\mathrm{T}} = (\sigma_n^2, \boldsymbol{\zeta}^{\mathrm{T}})$ where $\boldsymbol{\zeta}^{\mathrm{T}} = (\alpha, \boldsymbol{\theta}^{\mathrm{T}})$ and $\boldsymbol{\theta}^{\mathrm{T}} = (\varphi, \boldsymbol{\eta}^{\mathrm{T}})$:

$$\mathbf{F}_{\boldsymbol{\epsilon}} = \begin{bmatrix} \frac{N}{(\sigma_n^2)^2} & \mathbf{0}^{\mathrm{T}} \\ \mathbf{0} & \mathbf{F}_{\boldsymbol{\zeta}|\boldsymbol{\epsilon}} \end{bmatrix}. \tag{B.1}$$

B.1.2 Slepian-Bangs Formula Application

B.1.3 Case 1: Known Phase

When the phase φ is perfectly known, the observation model simplifies to $\mathbf{x} = \alpha \mathbf{a}(\boldsymbol{\eta}) e^{j\varphi} + \mathbf{n}$ with $\mathbf{n} \sim \mathcal{CN}(\mathbf{0}, \sigma_n^2 \mathbf{I}_N)$, and the parameter vector reduces to $\boldsymbol{\epsilon}^{\mathrm{T}} = (\sigma_n^2, \alpha, \boldsymbol{\eta}^{\mathrm{T}})$.

Noise Variance Component

For the noise variance parameter σ_n^2 with covariance matrix $\mathbf{C} = \sigma_n^2 \mathbf{I}_N$:

$$\begin{aligned} \mathbf{F}_{\sigma_n^2} &= \mathrm{tr}\left\{ \mathbf{C}^{-1} \frac{\partial \mathbf{C}}{\partial \sigma_n^2} \mathbf{C}^{-1} \frac{\partial \mathbf{C}}{\partial \sigma_n^2} \right\} \\ &= \mathrm{tr}\left\{ \frac{1}{(\sigma_n^2)^2} \mathbf{I}_N \right\} = \frac{N}{(\sigma_n^2)^2}. \end{aligned} \tag{B.2}$$

Amplitude Component

For the amplitude parameter α with mean vector $\boldsymbol{\mu} = \alpha\mathbf{a}(\boldsymbol{\eta})e^{j\varphi}$:

$$\begin{aligned}\mathbf{F}_{\alpha,\alpha} &= 2\Re\left\{\left[\mathbf{a}(\boldsymbol{\eta})e^{j\varphi}\right]^{\mathrm{H}}\frac{1}{\sigma_n^2}\left[\mathbf{a}(\boldsymbol{\eta})e^{j\varphi}\right]\right\} \\ &= \frac{2}{\sigma_n^2}\|\mathbf{a}(\boldsymbol{\eta})\|^2. \end{aligned} \tag{B.3}$$

Cross-Terms and Delay Parameters

The cross-terms between amplitude and delay parameters:

$$\mathbf{F}_{\alpha,\boldsymbol{\eta}} = \frac{2\alpha}{\sigma_n^2}\Re\left\{\mathbf{a}(\boldsymbol{\eta})^{\mathrm{H}}\frac{\partial\mathbf{a}(\boldsymbol{\eta})}{\partial\boldsymbol{\eta}^{\mathrm{T}}}\right\}. \tag{B.4}$$

The delay parameter components:

$$\mathbf{F}_{\boldsymbol{\eta},\boldsymbol{\eta}} = \frac{2\alpha^2}{\sigma_n^2}\Re\left\{\left(\frac{\partial\mathbf{a}(\boldsymbol{\eta})}{\partial\boldsymbol{\eta}^{\mathrm{T}}}\right)^{\mathrm{H}}\frac{\partial\mathbf{a}(\boldsymbol{\eta})}{\partial\boldsymbol{\eta}^{\mathrm{T}}}\right\}. \tag{B.5}$$

The complete FIM for known phase becomes:

$$\mathbf{F}_{\boldsymbol{\zeta}|\boldsymbol{\epsilon}} = \frac{2}{\sigma_n^2}\begin{bmatrix} \|\mathbf{a}(\boldsymbol{\eta})\|^2 & \alpha\Re\left\{\mathbf{a}(\boldsymbol{\eta})^{\mathrm{H}}\frac{\partial\mathbf{a}(\boldsymbol{\eta})}{\partial\boldsymbol{\eta}^{\mathrm{T}}}\right\} \\ \alpha\Re\left\{\mathbf{a}(\boldsymbol{\eta})^{\mathrm{H}}\frac{\partial\mathbf{a}(\boldsymbol{\eta})}{\partial\boldsymbol{\eta}^{\mathrm{T}}}\right\}^{\mathrm{T}} & \alpha^2\Re\left\{\left(\frac{\partial\mathbf{a}(\boldsymbol{\eta})}{\partial\boldsymbol{\eta}^{\mathrm{T}}}\right)^{\mathrm{H}}\frac{\partial\mathbf{a}(\boldsymbol{\eta})}{\partial\boldsymbol{\eta}^{\mathrm{T}}}\right\} \end{bmatrix}. \tag{B.6}$$

B.1.4 Case 2: Unknown Phase with Uncertainty

When the phase is unknown but measured with uncertainty, the joint probability distribution combines the complex observation vector and phase measurement:

$$p(\mathbf{x}, x_a; \boldsymbol{\epsilon}) = p(\mathbf{x}; \boldsymbol{\epsilon})p(x_a; \varphi), \tag{B.7}$$

where $x_a = \varphi + n_a$ with $n_a \sim \mathcal{N}(0, \sigma_{n_a}^2)$. The FIM is obtained by combining both contributions:

$$\mathbf{F}(\boldsymbol{\epsilon}) = -\mathrm{E}\left\{\frac{\partial^2 \ln p(\mathbf{x}, x_a; \boldsymbol{\epsilon})}{\partial\boldsymbol{\epsilon}\partial\boldsymbol{\epsilon}^{\mathrm{T}}}\right\} = \mathbf{F}_{\mathbf{x}}(\boldsymbol{\epsilon}) + \mathbf{F}_{x_a}(\boldsymbol{\epsilon}). \tag{B.8}$$

Additional Phase-Related Components

The cross-term between amplitude and phase vanishes:

$$\begin{aligned}\mathbf{F}_{\alpha,\varphi} &= 2\Re\left\{\left[\mathbf{a}(\boldsymbol{\eta})e^{j\varphi}\right]^{\mathrm{H}}\frac{1}{\sigma_n^2}\left[j\alpha\mathbf{a}(\boldsymbol{\eta})e^{j\varphi}\right]\right\} \\ &= \frac{2\alpha}{\sigma_n^2}\Re\left\{j\|\mathbf{a}(\boldsymbol{\eta})\|^2\right\} = 0. \end{aligned} \tag{B.9}$$

where the following relationship was applied,

$$A = (a + jb) \Rightarrow \Re\{-j \cdot A\} = \Re\{-ja + b\} = b \equiv \Im\{A\} \tag{B.10}$$

The phase parameter receives contributions from both sources:

$$\begin{aligned}\mathbf{F}_{\varphi,\varphi} &= 2\Re\left\{\left[j\alpha\mathbf{a}(\boldsymbol{\eta})e^{j\varphi}\right]^{\mathrm{H}}\frac{1}{\sigma_n^2}\left[j\alpha\mathbf{a}(\boldsymbol{\eta})e^{j\varphi}\right]\right\}+\frac{1}{\sigma_{n_a}^2}\\ &= \frac{2\alpha^2}{\sigma_n^2}\|\mathbf{a}(\boldsymbol{\eta})\|^2+\frac{1}{\sigma_{n_a}^2},\end{aligned} \tag{B.11}$$

where $\frac{1}{\sigma_{n_a}^2}$ represents the information contribution from the phase measurement. The cross-terms between phase and delay parameters:

$$\begin{aligned}\mathbf{F}_{\varphi,\boldsymbol{\eta}} &= 2\Re\left\{\left[j\alpha\mathbf{a}(\boldsymbol{\eta})e^{j\varphi}\right]^{\mathrm{H}}\frac{1}{\sigma_n^2}\left[\alpha\frac{\partial\mathbf{a}(\boldsymbol{\eta})}{\partial\boldsymbol{\eta}^{\mathrm{T}}}e^{j\varphi}\right]\right\}\\ &= \frac{2\alpha^2}{\sigma_n^2}\Re\left\{j\mathbf{a}(\boldsymbol{\eta})^{\mathrm{H}}\frac{\partial\mathbf{a}(\boldsymbol{\eta})}{\partial\boldsymbol{\eta}^{\mathrm{T}}}\right\}\\ &= -\frac{2\alpha^2}{\sigma_n^2}\mathrm{Im}\left\{\mathbf{a}(\boldsymbol{\eta})^{\mathrm{H}}\frac{\partial\mathbf{a}(\boldsymbol{\eta})}{\partial\boldsymbol{\eta}^{\mathrm{T}}}\right\}.\end{aligned} \tag{B.12}$$

Complete FIM for Unknown Phase

The complete FIM for the parameter subset $\boldsymbol{\zeta}$ with unknown phase:

$$\mathbf{F}_{\boldsymbol{\zeta}|\boldsymbol{\epsilon}} = \frac{2}{\sigma_n^2}\begin{bmatrix}\|\mathbf{a}(\boldsymbol{\eta})\|^2 & 0 & \alpha\Re\left\{\mathbf{a}(\boldsymbol{\eta})^{\mathrm{H}}\frac{\partial\mathbf{a}(\boldsymbol{\eta})}{\partial\boldsymbol{\eta}^{\mathrm{T}}}\right\}\\ 0 & \alpha^2\|\mathbf{a}(\boldsymbol{\eta})\|^2+\frac{\sigma_n^2}{2\sigma_{n_a}^2} & \alpha^2\mathrm{Im}\left\{\mathbf{a}(\boldsymbol{\eta})^{\mathrm{H}}\frac{\partial\mathbf{a}(\boldsymbol{\eta})}{\partial\boldsymbol{\eta}^{\mathrm{T}}}\right\}\\ \alpha\Re\left\{\mathbf{a}(\boldsymbol{\eta})^{\mathrm{H}}\frac{\partial\mathbf{a}(\boldsymbol{\eta})}{\partial\boldsymbol{\eta}^{\mathrm{T}}}\right\}^{\mathrm{T}} & \alpha^2\mathrm{Im}\left\{\mathbf{a}(\boldsymbol{\eta})^{\mathrm{H}}\frac{\partial\mathbf{a}(\boldsymbol{\eta})}{\partial\boldsymbol{\eta}^{\mathrm{T}}}\right\}^{\mathrm{T}} & \alpha^2\Re\left\{\left(\frac{\partial\mathbf{a}(\boldsymbol{\eta})}{\partial\boldsymbol{\eta}^{\mathrm{T}}}\right)^{\mathrm{H}}\frac{\partial\mathbf{a}(\boldsymbol{\eta})}{\partial\boldsymbol{\eta}^{\mathrm{T}}}\right\}\end{bmatrix}. \tag{B.13}$$

The FIM for the parameters of interest $\boldsymbol{\theta}$:

$$\mathbf{F}_{\boldsymbol{\theta}|\boldsymbol{\epsilon}} = \frac{2\alpha^2}{\sigma_n^2}\begin{bmatrix}\|\mathbf{a}(\boldsymbol{\eta})\|^2+\frac{\sigma_n^2}{2\alpha^2\sigma_{n_a}^2} & \mathrm{Im}\left\{\mathbf{a}(\boldsymbol{\eta})^{\mathrm{H}}\frac{\partial\mathbf{a}(\boldsymbol{\eta})}{\partial\boldsymbol{\eta}^{\mathrm{T}}}\right\}\\ \mathrm{Im}\left\{\mathbf{a}(\boldsymbol{\eta})^{\mathrm{H}}\frac{\partial\mathbf{a}(\boldsymbol{\eta})}{\partial\boldsymbol{\eta}^{\mathrm{T}}}\right\}^{\mathrm{T}} & \Re\left\{\left(\frac{\partial\mathbf{a}(\boldsymbol{\eta})}{\partial\boldsymbol{\eta}^{\mathrm{T}}}\right)^{\mathrm{H}}\frac{\partial\mathbf{a}(\boldsymbol{\eta})}{\partial\boldsymbol{\eta}^{\mathrm{T}}}\right\}\end{bmatrix}. \tag{B.14}$$

The term $\frac{\sigma_n^2}{2\alpha^2\sigma_{n_a}^2}$ in the $(1,1)$ element represents the additional uncertainty introduced by the phase measurement, with the FIM converging to the known-phase case as $\sigma_{n_a}^2 \to 0$.

B.2 Block matrix inversion lemma

For a block matrix of the form:

$$\mathbf{M} = \begin{bmatrix}\mathbf{M}_{11} & \mathbf{M}_{12}\\ \mathbf{M}_{21} & \mathbf{M}_{22}\end{bmatrix}, \tag{B.15}$$

where $\mathbf{M}_{11}$ and $\mathbf{M}_{22}$ are square matrices, and $\mathbf{M}$ would correspond to $\mathbf{F}_{\boldsymbol{\zeta}|\boldsymbol{\epsilon}}$ in (4.22). Assuming $\mathbf{M}_{11}$ is invertible, the inverse can be expressed as:

$$\mathbf{M}^{-1} = \begin{bmatrix}\mathbf{M}_{11}^{-1}+\mathbf{M}_{11}^{-1}\mathbf{M}_{12}\mathbf{S}^{-1}\mathbf{M}_{21}\mathbf{M}_{11}^{-1} & -\mathbf{M}_{11}^{-1}\mathbf{M}_{12}\mathbf{S}^{-1}\\ -\mathbf{S}^{-1}\mathbf{M}_{21}\mathbf{M}_{11}^{-1} & \mathbf{S}^{-1}\end{bmatrix}, \tag{B.16}$$

where $\mathbf{S} = \mathbf{M}_{22} - \mathbf{M}_{21}\mathbf{M}_{11}^{-1}\mathbf{M}_{12}$ is the Schur complement of $\mathbf{M}_{11}$ in $\mathbf{M}$.

B.3 Closed-Form Derivative terms

This section shows the derivation of the elements in matrix $\mathbf{W}$ and $\mathbf{w}$, which are computed after applying the Nyquist-Shannon theorem to reconstruct the continuous-time version associated to the products stemming from the derivative terms of the FIM, for instance, as in the wide-band case scenario derivative terms shown in equation (4.29). The Nyquist-Shannon assumption states that any signal that is sampled at a sampling frequency equal or double the maximum frequency of the continuous-time signal can be perfectly reconstructed from its discrete samples. Under this condition, the following applies,

$$\lim_{(N_1',N_2')\to(-\infty,\infty)} T_s \sum_{n=N_1'}^{N2'} \mathbf{v}(n\mathrm{T_s};\boldsymbol{\eta})\,\mathbf{v}^{\mathrm{H}}(n\mathrm{T_s};\boldsymbol{\eta}) = \mathrm{F_s}\int_{-\infty}^{\infty} \mathbf{v}(t;\boldsymbol{\eta})\,\mathbf{v}^{\mathrm{H}}(t;\boldsymbol{\eta})\,dt = \mathrm{F_s}\mathbf{W}, \tag{B.17a}$$

$$\lim_{(N_1',N_2')\to(-\infty,\infty)} T_s \sum_{n=N_1'}^{N2'} \mathbf{v}(n\mathrm{T_s};\boldsymbol{\eta})\mathbf{c}(n\mathrm{T_s};\boldsymbol{\eta}) = \mathrm{F_s}\int_{-\infty}^{\infty} \mathbf{v}(t;\boldsymbol{\eta})c^*(t;\boldsymbol{\eta})\,dt = \mathrm{F_s}\mathbf{w}, \tag{B.17b}$$

noting that $\mathrm{T_s}$ is added in both equations to match the definition in (B.17), together with its $1/\mathrm{T_s}$ counterpart to maintain equivalence, causing $\mathrm{F_s}$ to cancel out in the final result. By grouping the terms involved in the products $\mathbf{v}(t;\boldsymbol{\eta})\mathbf{v}^{\mathrm{H}}(t;\boldsymbol{\eta})$ and $\mathbf{v}(t;\boldsymbol{\eta})c^*(t;\boldsymbol{\eta})$ in (B.17), as

$$\mathbf{M} = \begin{array}{c} \\ c(t;\boldsymbol{\eta}) \\ t\,c(t;\boldsymbol{\eta}) \\ \dot{c}(t;\boldsymbol{\eta}) \\ t\,\dot{c}(t;\boldsymbol{\eta}) \end{array} \begin{array}{c} \begin{array}{cccc} c(t;\boldsymbol{\eta}) & t\,c(t;\boldsymbol{\eta}) & \dot{c}(t;\boldsymbol{\eta}) & t\,\dot{c}(t;\boldsymbol{\eta}) \end{array} \\ \begin{bmatrix} c(t;\boldsymbol{\eta})^{\mathrm{H}}c(t;\boldsymbol{\eta}) & c(t;\boldsymbol{\eta})^{\mathrm{H}}t\,c(t;\boldsymbol{\eta}) & c(t;\boldsymbol{\eta})^{\mathrm{H}}\dot{c}(t;\boldsymbol{\eta}) & c(t;\boldsymbol{\eta})^{\mathrm{H}}t\,\dot{c}(t;\boldsymbol{\eta}) \\ (t\,c(t;\boldsymbol{\eta}))^{\mathrm{H}}c(t;\boldsymbol{\eta}) & (t\,c(t;\boldsymbol{\eta}))^{\mathrm{H}}t\,c(t;\boldsymbol{\eta}) & (t\,c(t;\boldsymbol{\eta}))^{\mathrm{H}}\dot{c}(t;\boldsymbol{\eta}) & (t\,c(t;\boldsymbol{\eta}))^{\mathrm{H}}t\,\dot{c}(t;\boldsymbol{\eta}) \\ \dot{c}(t;\boldsymbol{\eta})^{\mathrm{H}}c(t;\boldsymbol{\eta}) & \dot{c}(t;\boldsymbol{\eta})^{\mathrm{H}}t\,c(t;\boldsymbol{\eta}) & \dot{c}(t;\boldsymbol{\eta})^{\mathrm{H}}\dot{c}(t;\boldsymbol{\eta}) & \dot{c}(t;\boldsymbol{\eta})^{\mathrm{H}}t\,\dot{c}(t;\boldsymbol{\eta}) \\ (t\,\dot{c}(t;\boldsymbol{\eta}))^{\mathrm{H}}c(t;\boldsymbol{\eta}) & (t\,\dot{c}(t;\boldsymbol{\eta}))^{\mathrm{H}}t\,c(t;\boldsymbol{\eta}) & (t\,\dot{c}(t;\boldsymbol{\eta}))^{\mathrm{H}}\dot{c}(t;\boldsymbol{\eta}) & (t\,\dot{c}(t;\boldsymbol{\eta}))^{\mathrm{H}}t\,\dot{c}(t;\boldsymbol{\eta}) \end{bmatrix} \end{array}. \tag{B.18}$$

and assuming the discrete-time redefinition of $c(t;\boldsymbol{\eta})$, i.e. $c(n\mathrm{T_s};\boldsymbol{\eta})$, the Nyquist-Shannon theorem is applied element-wise to matrix $\mathbf{M}$, to obtain the corresponding continuous-time equivalent:

$$\mathbf{W} = \lim_{(N_1',N_2')\to(-\infty,\infty)} T_s \sum_{n=N_1'}^{N2'} \mathbf{M} = \begin{bmatrix} w_1 & w_2^* & w_3^* & w_4^* \\ w_2 & W_{22} & W_{23}^* & W_{24}^* \\ w_3 & W_{23} & W_{33} & W_{34}^* \\ w_4 & W_{24} & W_{34} & W_{44} \end{bmatrix} \tag{B.19}$$

where each of the elements are individually computed as follows. First, considering the transformed complex exponential representation $c(t) = \frac{1}{\mathrm{F_s}}\sum_n c(n\mathrm{T_s})e^{-j2\pi nt/\mathrm{F_s}}$, the element w_1 is derived:

$$\begin{aligned} w_1 &= \int_{-\infty}^{\infty} c(t-\tau)c^*(t-\tau)dt \\ &\quad \text{Making change of variable: } u = t-\tau \Rightarrow t = u+\tau, dt = du \\ &= \int_{-\infty}^{\infty} c(u)c^*(u)du \\ &= \frac{1}{\mathrm{F_s}^2}\int_{-\mathrm{F_s}/2}^{\mathrm{F_s}/2} \left(\sum_n c(n\mathrm{T_s})e^{-j2\pi nu/\mathrm{F_s}}\right)\left(\sum_m c(m\mathrm{T_s})e^{-j2\pi mu/\mathrm{F_s}}\right)^* du \\ &= \frac{1}{\mathrm{F_s}^2}\sum_n\sum_m c(n\mathrm{T_s})c^*(m\mathrm{T_s})\int_{-\mathrm{F_s}/2}^{\mathrm{F_s}/2} e^{j2\pi nu/\mathrm{F_s}}e^{-j2\pi mu/\mathrm{F_s}}du \\ &= \frac{1}{\mathrm{F_s}^2}\sum_n c(n\mathrm{T_s})^{\mathrm{H}}c(n\mathrm{T_s})\cdot\mathrm{F_s} \\ &= \frac{\mathbf{c}^{\mathrm{H}}\mathbf{c}}{\mathrm{F_s}} \end{aligned} \tag{B.20}$$

where $\mathbf{c} = [c(N_1'\mathrm{T_s}), \ldots, c(N_2'\mathrm{T_s})]$. The element w_2 is derived by considering $c(t)^{\mathrm{H}}(tc(t))$:

$$
\begin{aligned}
w_2 &= \int_{-\infty}^{\infty} c(t-\tau)(t-\tau)^* c^*(t-\tau)dt \\
&\quad \text{Making change of variable: } u = t-\tau \Rightarrow t = u+\tau, dt = du \\
&= \int_{-\infty}^{\infty} c(u)uc^*(u)du \\
&= \int_{-\mathrm{F_s}/2}^{\mathrm{F_s}/2} \mathbf{C}(f)\left(\frac{j}{2\pi}\frac{\partial \mathbf{C}^*(f)}{\partial f}\right)df \\
&\quad \text{Making change of variable: } f' = f/\mathrm{F_s} \Rightarrow f = f'\mathrm{F_s}, df = df'\mathrm{F_s} \\
&= \frac{1}{{\mathrm{F_s}}^2}\int_{-1/2}^{1/2}\left(\sum_n c(n\mathrm{T_s})e^{-j2\pi nf'}\right)\left(\frac{j}{2\pi}\frac{\partial}{\partial f'}\left(\sum_m c^*(m\mathrm{T_s})e^{j2\pi mf'}\right)\cdot\frac{1}{\mathrm{F_s}}\right)df'\mathrm{F_s} \\
&= \frac{1}{{\mathrm{F_s}}^2}\int_{-1/2}^{1/2}\left(\sum_n c(n\mathrm{T_s})e^{-j2\pi nf'}\right)\left(\sum_m mc^*(m\mathrm{T_s})e^{j2\pi mf'}\right)df' \\
&= \frac{1}{{\mathrm{F_s}}^2}\sum_n\sum_m mc(n\mathrm{T_s})c^*(m\mathrm{T_s})\int_{-1/2}^{1/2} e^{-j2\pi(n-m)f'}df' \\
&= \frac{1}{{\mathrm{F_s}}^2}\sum_n nc(n\mathrm{T_s})c^*(n\mathrm{T_s}) \\
&= \frac{\mathbf{c}^{\mathrm{H}}\mathbf{D}\mathbf{c}}{{\mathrm{F_s}}^2}
\end{aligned}
\tag{B.21}
$$

where $\mathbf{D}$ is the diagonal matrix defined as:

$$
\mathbf{D} = \mathrm{diag}(N_1', N_1'+1, \ldots, N_2'-1, N_2'). \tag{B.22}
$$

For the element w_3, representing $c(t)^{\mathrm{H}}\dot{c}(t)$:

$$
\begin{aligned}
w_3 &= \int_{-\infty}^{\infty} c(t-\tau)\dot{c}^*(t-\tau)dt \\
&\quad \text{Making change of variable: } u = t-\tau \Rightarrow t = u+\tau, dt = du \\
&= \int_{-\infty}^{\infty} c(u)\dot{c}^*(u)du \\
&= \int_{-\infty}^{\infty} \mathbf{C}(f)\cdot(j2\pi f)^*\mathbf{C}^*(f)df \\
&\quad \text{Making change of variable: } f' = f/\mathrm{F_s} \Rightarrow f = f'\mathrm{F_s}, df = df'\mathrm{F_s} \\
&= \int_{-1/2}^{1/2}\left(\frac{1}{\mathrm{F_s}}\sum_n c(n\mathrm{T_s})e^{-j2\pi nf'}\right)(-j2\pi f'\mathrm{F_s})\left(\frac{1}{\mathrm{F_s}}\sum_m c^*(m\mathrm{T_s})e^{j2\pi mf'}\right)df'\mathrm{F_s} \\
&= \int_{-1/2}^{1/2}(-j2\pi f')\sum_n\sum_m c(n\mathrm{T_s})c^*(m\mathrm{T_s})e^{-j2\pi nf'}e^{j2\pi mf'}df' \\
&= \int_{-1/2}^{1/2}(-j2\pi f')\left(\mathbf{c}^{\mathrm{T}}\boldsymbol{\nu}\right)\left(\mathbf{c}^{\mathrm{T}}\boldsymbol{\nu}\right)^* df' \\
&= \mathbf{c}^{\mathrm{T}}\left(-j2\pi\int_{-1/2}^{1/2} f'\boldsymbol{\nu}\boldsymbol{\nu}^* df'\right)\mathbf{c}^* \\
&= -\mathbf{c}^{\mathrm{H}}\boldsymbol{\Lambda}\mathbf{c}
\end{aligned}
\tag{B.23}
$$

where $\boldsymbol{\nu} = [e^{j2\pi f' N_1'}, \ldots, e^{j2\pi f' N_2'}]$ and Λ derived in Sec. B.3.1. For the element w_4 representing $c(t)^{\mathrm{H}}(t\dot{c}(t))$:

$$
\begin{aligned}
w_4 &= \int_{-\infty}^{\infty} c(t-\tau)(t-\tau)\dot{c}^*(t-\tau)dt \\
&\quad \text{Making change of variable: } u = t-\tau \Rightarrow t = u+\tau, dt = du \\
&= \int_{-\infty}^{\infty} c(u)\cdot u \cdot \dot{c}^*(u)du \\
&= \int_{-\infty}^{\infty} uc(u)\cdot \dot{c}^*(u)du \\
&= \int_{-\infty}^{\infty} \left(\frac{j}{2\pi}\frac{d\mathbf{C}(f)}{df}\right)\cdot (j2\pi f)^*\mathbf{C}^*(f)df \\
&= \int_{-\infty}^{\infty} \left(\frac{j}{2\pi}\frac{d\mathbf{C}(f)}{df}\right)\cdot (-j2\pi f)\mathbf{C}^*(f)df \\
&\quad \text{Making change of variable: } f' = f/\mathrm{F_s} \Rightarrow f = f'\mathrm{F_s}, df = df'\mathrm{F_s} \\
&= \int_{-1/2}^{1/2} \left(\frac{j}{2\pi}\frac{d}{df'}\left(\frac{1}{\mathrm{F_s}}\sum_n c(n\mathrm{T_s})e^{-j2\pi n f'}\right)\cdot\frac{1}{\mathrm{F_s}}\right) \\
&\qquad \times (-j2\pi f'\mathrm{F_s})\left(\frac{1}{\mathrm{F_s}}\sum_m c^*(m\mathrm{T_s})e^{j2\pi m f'}\right)df'\mathrm{F_s} \\
&= \frac{1}{{\mathrm{F_s}}^2}\int_{-1/2}^{1/2}\sum_n\sum_m nc(n\mathrm{T_s})c^*(m\mathrm{T_s})(-j2\pi f')e^{-j2\pi(n-m)f'}df' \\
&= \frac{1}{{\mathrm{F_s}}^2}\sum_n\sum_m nc(n\mathrm{T_s})c^*(m\mathrm{T_s})(-\Lambda_{m,n}) \\
&= -\frac{\mathbf{c}^{\mathrm{H}}\mathbf{D}\boldsymbol{\Lambda}\mathbf{c}}{{\mathrm{F_s}}^2}
\end{aligned}
\tag{B.24}
$$

For W_{22} representing $(tc(t))(tc(t))^{\mathrm{H}}$:

$$
\begin{aligned}
W_{22} &= \int_{-\infty}^{\infty} ((t-\tau)c(t-\tau))((t-\tau)c(t-\tau))^{\mathrm{H}} dt \\
&\quad \text{Making change of variable: } u = t-\tau \Rightarrow t = u+\tau, dt = du \\
&= \int_{-\infty}^{\infty} (uc(u))(uc(u))^{\mathrm{H}} du \\
&= \int_{-\infty}^{\infty} u^2 c(u)c(u)^{\mathrm{H}} du \\
&= \int_{-\infty}^{\infty} \left(\frac{j}{2\pi}\frac{d\mathbf{C}(f)}{df}\right)\left(\frac{j}{2\pi}\frac{d\mathbf{C}(f)}{df}\right)^{\mathrm{H}} df \\
&\quad \text{Making change of variable: } f' = f/\mathrm{F_s} \Rightarrow f = f'\mathrm{F_s}, df = df'\mathrm{F_s} \\
&= \frac{1}{{\mathrm{F_s}}^3}\int_{-1/2}^{1/2} \left(\sum_n nc(n\mathrm{T_s})e^{-j2\pi nf'}\right)\left(\sum_m mc^*(m\mathrm{T_s})e^{j2\pi mf'}\right) df' \\
&= \frac{1}{{\mathrm{F_s}}^3}\sum_n\sum_m nmc(n\mathrm{T_s})c^*(m\mathrm{T_s})\int_{-1/2}^{1/2} e^{-j2\pi(n-m)f'} df' \\
&= \frac{1}{{\mathrm{F_s}}^3}\sum_n n^2 c(n\mathrm{T_s})c^*(n\mathrm{T_s}) \\
&= \frac{\mathbf{c}^{\mathrm{H}}\mathbf{D}^2\mathbf{c}}{{\mathrm{F_s}}^3}
\end{aligned}
\tag{B.25}
$$

For W_{23} representing $(tc(t))\dot{c}(t)^{\mathrm{H}}$:

$$
\begin{aligned}
W_{23} &= \int_{-\infty}^{\infty} ((t-\tau)c(t-\tau))\dot{c}(t-\tau)^{\mathrm{H}} dt \\
&\quad \text{Making change of variable: } u = t-\tau \Rightarrow t = u+\tau, dt = du \\
&= \int_{-\infty}^{\infty} (uc(u))\dot{c}(u)^{\mathrm{H}} du \\
&= \int_{-\infty}^{\infty} uc(u)\dot{c}(u)^{\mathrm{H}} du \\
&= \int_{-\infty}^{\infty} \left(\frac{j}{2\pi}\frac{d\mathbf{C}(f)}{df}\right)(j2\pi f)^*\mathbf{C}^{\mathrm{H}}(f) df \\
&\quad \text{Making change of variable: } f' = f/\mathrm{F_s} \Rightarrow f = f'\mathrm{F_s}, df = df'\mathrm{F_s} \\
&= \int_{-1/2}^{1/2} \left(\frac{1}{\mathrm{F_s}}\sum_n nc(n\mathrm{T_s})e^{-j2\pi nf'}\right)(j2\pi f'\mathrm{F_s})\left(\frac{1}{\mathrm{F_s}}\sum_m c^*(m\mathrm{T_s})e^{j2\pi mf'}\right) df'\mathrm{F_s} \\
&= \int_{-1/2}^{1/2} (j2\pi f')\sum_n\sum_m nc(n\mathrm{T_s})c^*(m\mathrm{T_s})e^{-j2\pi(n-m)f'} df' \\
&= \sum_n\sum_m nc(n\mathrm{T_s})c^*(m\mathrm{T_s})\Lambda_{n,m} \\
&= \mathbf{c}^{\mathrm{H}}\mathbf{D}\Lambda\mathbf{c}
\end{aligned}
\tag{B.26}
$$

For W_{24} representing $(tc(t))(t\dot{c}(t))^{\mathrm{H}}$:

$$
\begin{aligned}
W_{24} &= \int_{-\infty}^{\infty} (t-\tau)c(t-\tau)((t-\tau)\dot{c}(t-\tau))^{\mathrm{H}} dt \\
&\text{Making change of variable: } u = t-\tau \Rightarrow t = u+\tau, dt = du \\
&= \int_{-\infty}^{\infty} uc(u)(u\dot{c}(u))^{\mathrm{H}} du \\
&= \int_{-\infty}^{\infty} u^2 c(u)\dot{c}(u)^{\mathrm{H}} du \\
&= \int_{-\mathrm{F_s}/2}^{\mathrm{F_s}/2} (j2\pi f)^* \mathbf{C}(f) \frac{j}{2\pi} \frac{\partial \mathbf{C}^{\mathrm{H}}(f)}{\partial f} df \\
&= \int_{-\mathrm{F_s}/2}^{\mathrm{F_s}/2} (j2\pi f)^* \left(\frac{1}{\mathrm{F_s}} \sum_n c(n\mathrm{T_s}) e^{-j2\pi nf} \right) \frac{j}{2\pi} \frac{\partial}{\partial f} \left(\frac{1}{\mathrm{F_s}} \sum_m c^*(m\mathrm{T_s}) e^{j2\pi mf} \right) df \\
&\text{Making change of variable: } f' = f/\mathrm{F_s} \Rightarrow f = f'\mathrm{F_s}, df = df'\mathrm{F_s} \\
&= \int_{-1/2}^{1/2} (j2\pi f'\mathrm{F_s})^* \left(\frac{1}{\mathrm{F_s}} \sum_n c(n\mathrm{T_s}) e^{-j2\pi nf'} \right) \frac{j}{2\pi} \frac{\partial}{\partial f'} \left(\frac{1}{\mathrm{F_s}} \sum_m c^*(m\mathrm{T_s}) e^{j2\pi mf'} \right) \cdot \frac{1}{\mathrm{F_s}} df'\mathrm{F_s} \\
&= \int_{-1/2}^{1/2} (j2\pi f')^* \left(\sum_n c(n\mathrm{T_s}) e^{-j2\pi nf'} \right) \frac{j}{2\pi} \frac{\partial}{\partial f'} \left(\sum_m c^*(m\mathrm{T_s}) e^{j2\pi mf'} \right) df' \\
&= \mathrm{F_s} \int_{-1/2}^{1/2} (2\pi f') \left(\sum_n c(n\mathrm{T_s}) e^{-j2\pi nf'} \right) \left(\sum_m m c^*(m\mathrm{T_s}) e^{j2\pi mf'} \right) df' \\
&= \mathrm{F_s} \int_{-1/2}^{1/2} (2\pi f') \left(\mathbf{c}^{\mathrm{T}} \boldsymbol{\nu} \right) \left(\mathbf{D}\mathbf{c}^{\mathrm{T}} \boldsymbol{\nu} \right)^* df' \\
&= \mathrm{F_s} \mathbf{c}^{\mathrm{T}} \left(\int_{-1/2}^{1/2} (2\pi f') \boldsymbol{\nu}\boldsymbol{\nu}^* df' \right) \mathbf{D}^{\mathrm{T}} \mathbf{c}^* \\
&= \frac{\mathbf{c}^{\mathrm{H}} \mathbf{D} \boldsymbol{\Lambda} \mathbf{D} \mathbf{c}}{\mathrm{F_s}^2}
\end{aligned}
\tag{B.27}
$$

For W_{33} representing $\dot{c}(t)\dot{c}(t)^{\mathrm{H}}$:

$$
\begin{aligned}
W_{33} &= \int_{-\infty}^{\infty} \dot{c}(t-\tau)\dot{c}(t-\tau)^{\mathrm{H}} dt \\
&\text{Making change of variable: } u = t-\tau \Rightarrow t = u+\tau, dt = du \\
&= \int_{-\infty}^{\infty} \dot{c}(u)\dot{c}(u)^{\mathrm{H}} du \\
&= \int_{-\infty}^{\infty} (j2\pi f)\mathbf{C}(f)((j2\pi f)\mathbf{C}(f))^{\mathrm{H}} df \\
&\text{Making change of variable: } f' = f/\mathrm{F_s} \Rightarrow f = f'\mathrm{F_s}, df = df'\mathrm{F_s} \\
&= \mathrm{F_s} \int_{-1/2}^{1/2} 4\pi^2 (f')^2 \left(\frac{1}{\mathrm{F_s}} \sum_n c(n\mathrm{T_s}) e^{-j2\pi nf'} \right) \left(\frac{1}{\mathrm{F_s}} \sum_m c^*(m\mathrm{T_s}) e^{j2\pi mf'} \right) df' \\
&= \mathrm{F_s} \int_{-1/2}^{1/2} 4\pi^2 (f')^2 \sum_n \sum_m c(n\mathrm{T_s}) c^*(m\mathrm{T_s}) e^{-j2\pi(n-m)f'} df' \\
&= \mathrm{F_s} \sum_n \sum_m c(n\mathrm{T_s}) c^*(m\mathrm{T_s}) \mathbf{V}_{n,m} \\
&= \mathrm{F_s} \mathbf{c}^{\mathrm{H}} \mathbf{V} \mathbf{c}
\end{aligned}
\tag{B.28}
$$

For W_{34} representing $\dot{c}(t)(t\dot{c}(t))^{\mathrm{H}}$:

$$\begin{aligned}
W_{34} &= \int_{-\infty}^{\infty} \dot{c}(t-\tau)((t-\tau)\dot{c}(t-\tau))^{\mathrm{H}} dt \\
&\quad \text{Making change of variable: } u = t-\tau \Rightarrow t = u+\tau, dt = du \\
&= \int_{-\infty}^{\infty} \dot{c}(u)(u\dot{c}(u))^{\mathrm{H}} du \\
&= \int_{-\infty}^{\infty} (j2\pi f)\mathbf{C}(f)\left(\frac{j}{2\pi}\frac{\partial \mathbf{C}^{\mathrm{H}}(f)}{\partial f}\right) df \\
&\quad \text{Making change of variable: } f' = f/\mathrm{F_s} \Rightarrow f = f'\mathrm{F_s}, df = df'\mathrm{F_s} \\
&= \mathrm{F_s}\int_{-1/2}^{1/2} (j2\pi f')\left(\sum_n c(n\mathrm{T_s})e^{-j2\pi n f'}\right)\left(\sum_m mc^*(m\mathrm{T_s})e^{j2\pi m f'}\right) df' \\
&= \mathrm{F_s}\sum_n\sum_m mc(n\mathrm{T_s})c^*(m\mathrm{T_s})\mathbf{V}_{n,m} \\
&= \mathrm{F_s}\mathbf{c}^{\mathrm{H}}\mathbf{V}\mathbf{D}\mathbf{c}
\end{aligned} \tag{B.29}$$

For W_{44} representing $(t\dot{c}(t))(t\dot{c}(t))^{\mathrm{H}}$:

$$\begin{aligned}
W_{44} &= \int_{-\infty}^{\infty} ((t-\tau)\dot{c}(t-\tau))((t-\tau)\dot{c}(t-\tau))^{\mathrm{H}} dt \\
&\quad \text{Making change of variable: } u = t-\tau \Rightarrow t = u+\tau, dt = du \\
&= \int_{-\infty}^{\infty} (u\dot{c}(u))(u\dot{c}(u))^{\mathrm{H}} du \\
&= \int_{-\infty}^{\infty} u^2\dot{c}(u)\dot{c}(u)^{\mathrm{H}} du \\
&= \int_{-\infty}^{\infty} \left(\frac{j}{2\pi}\frac{d\mathbf{C}(f)}{df}\right)\left(\frac{j}{2\pi}\frac{d\mathbf{C}^{\mathrm{H}}(f)}{df}\right) df \\
&\quad \text{Making change of variable: } f' = f/\mathrm{F_s} \Rightarrow f = f'\mathrm{F_s}, df = df'\mathrm{F_s} \\
&= {\mathrm{F_s}}^3\int_{-1/2}^{1/2} 4\pi^2(f')^2\left(\sum_n nc(n\mathrm{T_s})e^{-j2\pi n f'}\right)\left(\sum_m mc^*(m\mathrm{T_s})e^{j2\pi m f'}\right) df' \\
&= {\mathrm{F_s}}^3\sum_n\sum_m nmc(n\mathrm{T_s})c^*(m\mathrm{T_s})\mathbf{V}_{n,m} \\
&= \mathrm{F_s}\mathbf{c}^{\mathrm{H}}\mathbf{D}\mathbf{V}\mathbf{D}\mathbf{c}
\end{aligned} \tag{B.30}$$

B.3.1 First-order integral term Λ

The matrix Λ arises from integrating the exponential $e^{-j2\pi(n-m)f'}$ weighted by f':

$$\Lambda_{n,m} = -j2\pi\int_{-1/2}^{1/2} f' e^{-j2\pi(n-m)f'} df' \tag{B.31}$$

When $n = m$:

$$\Lambda_{n,n} = -j2\pi\int_{-1/2}^{1/2} f' df' = -j2\pi\left[\frac{(f')^2}{2}\right]_{-1/2}^{1/2} = 0 \tag{B.32}$$

When $n \neq m$, let $N = n - m$. Using integration by parts with $u = f'$, $du = df'$, $dv = e^{-j2\pi N f'} df'$, $v = \frac{e^{-j2\pi N f'}}{-j2\pi N}$:

$$\begin{aligned}\Lambda_{n,m} &= -j2\pi \left[\frac{f' e^{-j2\pi N f'}}{-j2\pi N} \Big|_{-1/2}^{1/2} - \int_{-1/2}^{1/2} \frac{e^{-j2\pi N f'}}{-j2\pi N} df' \right] \\ &= \left[\frac{(1/2)e^{-j\pi N} - (-1/2)e^{j\pi N}}{N} \right] - \left[\frac{e^{-j\pi N} - e^{j\pi N}}{-2\pi N^2} \right] \\ &= \frac{(1/2)e^{-j\pi N} + (1/2)e^{j\pi N}}{N} = \frac{\cos(\pi N)}{N} = \frac{(-1)^N}{N} \end{aligned} \tag{B.33}$$

Therefore:

$$\Lambda_{n,m} = \begin{cases} 0 & \text{if } n = m \\ \frac{(-1)^{n-m}}{n-m} & \text{if } n \neq m \end{cases} \tag{B.34}$$

B.3.2 Second-order integral term V

The matrix $\mathbf{V}$ arises from integrating the exponential $e^{-j2\pi(n-m)f'}$ weighted by $(f')^2$:

$$\mathbf{V}_{n,m} = -4\pi^2 \int_{-1/2}^{1/2} (f')^2 e^{-j2\pi(n-m)f'} df' \tag{B.35}$$

For diagonal elements ($n = m$):

$$\begin{aligned}\mathbf{V}_{n,n} &= -4\pi^2 \int_{-1/2}^{1/2} (f')^2 df' = -4\pi^2 \left[\frac{(f')^3}{3} \right]_{-1/2}^{1/2} \\ &= -4\pi^2 \left(\frac{1/8 - (-1/8)}{3} \right) = -\frac{\pi^2}{3} \end{aligned} \tag{B.36}$$

For off-diagonal elements ($n \neq m$), let $N = n - m$. Using integration by parts twice:

First integration by parts with $u = (f')^2$, $du = 2f'df'$, $dv = e^{-j2\pi N f'} df'$, $v = \frac{e^{-j2\pi N f'}}{-j2\pi N}$:

$$\mathbf{V}_{n,m} = -4\pi^2 \left[\frac{(f')^2 e^{-j2\pi N f'}}{-j2\pi N} \Big|_{-1/2}^{1/2} - \frac{2}{-j2\pi N} \int_{-1/2}^{1/2} f' e^{-j2\pi N f'} df' \right] \tag{B.37}$$

Second integration by parts for the remaining integral:

$$\begin{aligned}\int_{-1/2}^{1/2} f' e^{-j2\pi N f'} df' &= \left[\frac{f' e^{-j2\pi N f'}}{-j2\pi N} \right]_{-1/2}^{1/2} - \int_{-1/2}^{1/2} \frac{e^{-j2\pi N f'}}{-j2\pi N} df' \\ &= \frac{(1/2)e^{-j\pi N} - (-1/2)e^{j\pi N}}{-j2\pi N} - \frac{e^{-j\pi N} - e^{j\pi N}}{(2\pi N)^2} \end{aligned} \tag{B.38}$$

Substituting back and simplifying (using $\sin(\pi N) = 0$ and $\cos(\pi N) = (-1)^N$ for integer N):

$$\mathbf{V}_{n,m} = \begin{cases} -\frac{\pi^2}{3} & \text{if } n = m \\ \frac{2(-1)^{n-m}}{(n-m)^2} & \text{if } n \neq m \end{cases} \tag{B.39}$$

Bibliography

[Bernabeu 2022] J. Bernabeu, F. Palafox, Y. Li et D. M. Akos. *A collection of SDRs for global navigation satellite systems (GNSS).* In Proceedings of the 2022 International Technical Meeting of The Institute of Navigation, pages 906–919, 2022.

[Bernabeu 2023a] J. Bernabeu, L. Ortega, A. Blais, Y. Grégoire et E. Chaumette. *On the asymptotic performance of time-delay and Doppler estimation with a carrier modulated by a band-limited signal.* EURASIP - JASP, 2023. Article ID 295029. DOI: 10.21203/rs.3.rs-3539143/v1.

[Bernabeu 2023b] J. Bernabeu, L. Ortega, A. Blais, Y. Grégoire et E. Chaumette. *Time-Delay and Doppler Estimation with a Carrier Modulated by a Band-Limited Signal.* In 2023 IEEE 9th International Workshop on Computational Advances in Multi-Sensor Adaptive Processing (CAMSAP), pages 346–350, 2023.

[Bernabeu 2024a] J. Bernabeu, L. Ortega, A. Blais, Y. Grégoire et E. Chaumette. *Delay Estimation with a Carrier Modulated by a Band-Limited Signal.* In 32nd European Signal Processing Conference, EUSIPCO 2024, Lyon, France, August 26-30, 2024, pages 1212–1216. IEEE, 2024.

[Bernabeu 2024b] J. Bernabeu, L. Ortega, A. Blais, Y. Grégoire et E. Chaumette. *On Time-Delay Estimation Accuracy Limit Under Phase Uncertainty.* In 2024 27th International Conference on Information Fusion (FUSION), (Accepted), 2024.

[Bernabeu 2025] J. Bernabeu, L. Ortega, A. Blais, Y. Grégoire et E. Chaumette. *Time-Delay Maximum-Likelihood Estimator under Phase Uncertainty.* In 2025 IEEE 10th International Workshop on Computational Advances in Multi-Sensor Adaptive Processing (CAMSAP), 2025.

[Cecconi 2018] B. Cecconi, M. Dekkali, C. Briand, B. Segret, J. N. Girard, A. Laurens, A. Lamy, D. Valat, M. Delpech, M. Bruno, P. Gélard, M. Bucher, Q. Nenon, J.-M. Grießmeier, A.-J. Boonstra et M. Bentum. *NOIRE Study Report: Towards a Low Frequency Radio Interferometer in Space.* In Proc. of the IEEE Aerospace Conference, 2018. arXiv:1710.10245 [astro-ph.IM].

[Chaumette 2025] E. Chaumette, J. Vilà-Valls et Y. Grégoire. *Centralized Cooperative Positioning from Euclidean Distance Matrices: Multidimensional Scaling and Maximum Likelihood.* In 33rd European Signal Processing Conference, EUSIPCO 2025, Palermo, Italy, 2025.

[D. 1990] William D. Journey through genius: The great theorems of mathematics. Wiley, New York, 1990.

[Das 2019] P. Das, J. Vilà-Valls, E. Chaumette, F. Vincent, L. Davain et S. Bonnabel. *On the Accuracy Limit of Time-delay Estimation with a Band-limited Signal.* In Proc. of the IEEE Intl. Conf. on Acoustics, Speech and Signal Processing (ICASSP), Brighton, UK, May 2019.

[Das 2020a] P. Das, L. Ortega, J. Vilà-Valls, F. Vincent, E. Chaumette et Loïc Davain. *Performance Limits of GNSS Code-Based Precise Positioning: GPS, Galileo & Meta-Signals.* Sensors, vol. 20, no. 8, page 2196, 2020.

[Das 2020b] P. Das, J. Vilà-Valls, F. Vincent, L. Davain et E. Chaumette. *A New Compact Delay, Doppler Stretch and Phase Estimation CRB with a Band-Limited Signal for GenE. Remote Sensing Applications.* Remote Sensing, vol. 12, no. 18, page 2913, Sep. 2020.

[De Maio 2016] A. De Maio, M. Greco*et al. Modern radar detection theory.* 2016.

[Dokmanic 2015] Ivan Dokmanic, Reza Parhizkar, Juri Ranieri et Martin Vetterli. *Euclidean Distance Matrices: Essential theory, algorithms, and applications.* IEEE Signal Processing Magazine, vol. 32, no. 6, pages 12–30, 2015.

[Dunn 2012] M. J. Dunn et D Disl. *Global positioning system directorate systems engineering & integration interface specification is-GPS-200.* Global Positioning Systems Directorate, 2012.

[Fortunati 2017] S. Fortunati, F. Gini, M. S. Greco et C. D. Richmond. *Performance Bounds for Parameter Estimation under Misspecified Models: Fundamental Findings and Applications.* IEEE Signal Processing Magazine, vol. 34, no. 6, pages 142–157, Nov. 2017.

[Fortunati 2024] S. Fortunati et L. Ortega. *On the efficiency of misspecified Gaussian inference in nonlinear regression: application to time-delay and Doppler estimation.* Signal Processing, vol. 225, page 109614, 2024.

[Kaplan 2006] E. D. Kaplan, editeur. Understanding gps: principles and applications. Artech House, 2nd édition, 2006.

[Kasami 1966] T. Kasami. Weight distribution formula for some class of cyclic codes. University of Illinois. Coordinated Science Laboratory. University of Illinois, 1966.

[Kay 1993] S. M. Kay. Fundamentals of statistical signal processing: Estimation theory. Prentice-Hall, Englewood Cliffs, New Jersey, USA, 1993.

[Le Chevalier 2002] F. Le Chevalier. Principles of radar and sonar signal processing. Artech House, 2002.

[Lesouple 2024] J. Lesouple et L. Ortega. *Bayesian EM Approach for GNSS Parameters of Interest Estimation Under Constant Modulus Interference.* EURASIP Journal on Advances in Signal Processing, 2024.

[Lubeigt 2020] C. Lubeigt, L. Ortega, J. Vilà-Valls, L. Lestarquit et E. Chaumette. *Joint Delay-Doppler Estimation Performance in a Dual Source Context.* Remote Sensing, vol. 12, no. 23, 2020.

[Lubeigt 2023a] C. Lubeigt, L. Ortega, J. Vilà-Valls et E. Chaumette. *Untangling first and second order statistics contributions in multipath scenarios.* Signal Processing, vol. 205, page 108868, 2023.

[Lubeigt 2023b] C. Lubeigt, F. Vincent, L. Ortega, J. Vilà-Valls et E. Chaumette. *Approximate maximum likelihood time-delay estimation for two closely spaced sources.* Signal Processing, vol. 210, page 109056, 2023.

[Mardia 2010] K. V Mardia. *Bayesian analysis for bivariate von Mises distributions.* Journal of Applied Statistics, vol. 37, no. 3, pages 515–528, 2010.

[McPhee 2023a] H. McPhee, L. Ortega, J. Vilà-Valls et E. Chaumette. *Accounting for Acceleration—Signal Parameters Estimation Performance Limits in High Dynamics Applications*. IEEE Transactions on Aerospace and Electronic Systems, vol. 59, no. 1, pages 610–622, 2023.

[McPhee 2023b] H. McPhee, L. Ortega, J. Vilà-Valls et E. Chaumette. *On the accuracy limits of misspecified delay-Doppler estimation*. Signal Processing, vol. 205, page 108872, 2023.

[Medina 2020] D. Medina, L. Ortega, J. Vilà-Valls, P. Closas, F. Vincent et E. Chaumette. *Compact CRB for Delay, Doppler and Phase Estimation - Application to GNSS SPP & RTK Performance Characterization*. IET Radar, Sonar & Navigation, vol. 14, no. 10, pages 1537–1549, Sep. 2020.

[Mengali 2013] U. Mengali. Synchronization techniques for digital receivers. Springer Science & Business Media, 2013.

[Morales-Aguirre] E. Morales-Aguirre, S. Labsir, B. Priot, C. Gazzino et G. Pages. *Modélisation sur groupes de Lie d'une distribution de Von Mises: application à la phase du signal GNSS*.

[Morales-Aguirre 2025] E. Morales-Aguirre, S. Labsir, B. Priot, C. Gazzino et G. Pages. *Lie Group Based Approach for GNSS Signal Phase Modeling*. In 2025 International Conference on Localization and GNSS (ICL-GNSS), pages 1–6. IEEE, 2025.

[Naouri 2021] A. Naouri, L. Ortega, J. Vilá-Valls et E. Chaumette. *A Multidimensional Scaling Approach for Seamless Indoor/Outdoor Cooperative GNSS Navigation*. In ICL-GNSS, Tampere , Finland., 2021.

[Ollila 2012] E. Ollila, D. E. Tyler, V. Koivunen et H. V. Poor. *Complex Elliptically Symmetric Distributions: Survey, New Results and Applications*. IEEE Transactions on Signal Processing, vol. 60, no. 11, pages 5597–5625, 2012.

[Ortega 2019] L. Ortega, C. Poulliat, M.L. Boucheret, M.Aubault-Roudier et H. Al-Bitar. *Binary Root Protograph LDPC Codes for CSK Modulation to Increase the Data Rate and Reduce the TTD*. ION GNSS+, Miami, Florida, USA, 16/09/19-20/09/19, September 2019. Institute of Navigation (ION).

[Ortega 2020] L. Ortega, D. Medina, J. Vilà-Valls, François Vincent et E. Chaumette. *Positioning Performance Limits of GNSS Meta-Signals and HO-BOC Signals*. Sensors, vol. 20, no. 12, page 3586, 2020.

[Ortega 2021] L. Ortega, J. Vilà-Valls, C. Poulliat et P. Closas. *GNSS Data Demodulation over Fading Environments: Antipodal and M-ary CSK Modulations*. IET Radar, Sonar & Navigation, January 2021.

[Ortega 2022] L. Ortega, J. Vilà-Valls et E. Chaumette. *Non-Binary PRN-Chirp Modulation: A New GNSS Fast Acquisition Signal Waveform*. IEEE Communications Letters, vol. 26, no. 9, pages 2151–2155, 2022.

[Ortega 2023] L. Ortega, C. Lubeigt, J. Vilà-Valls et E. Chaumette. *On GNSS Synchronization Performance Degradation under Interference Scenarios: Bias and Misspecified Cramér-Rao Bounds*. NAVIGATION: Journal of the Institute of Navigation, vol. 70, no. 4, 2023.

[Ortega 2024] L. Ortega et S. Fortunati. *Misspecified Time-delay and Doppler estimation over non Gaussian scenarios,*. In ICCASP, Seoul, Korea, April 2024.

[Ortega 2025] L. Ortega et S. Fortunati. *Robust Semiparametric Time-Delay and Doppler Estimation: Analysis of R- and M-Estimators*. In Eusipco, Parlemo, Italy, Septembre 2025.

[Renaux 2006] A. Renaux, P. Forster, E. Chaumette et P. Larzabal. *On the High-SNR Conditional Maximum-Likelihood Estimator Full Statistical Characterization.* IEEE Trans. Signal Process., vol. 54, no. 12, pages 4840 – 4843, Dec. 2006.

[Seber 2008] G. AF Seber. A matrix handbook for statisticians. John Wiley & Sons, 2008.

[Shannon 2006] Claude E Shannon. *Communication in the presence of noise.* Proceedings of the IRE, vol. 37, no. 1, pages 10–21, 2006.

[Stoica 1990] P. Stoica et A. Nehorai. *Performance study of conditional and unconditional direction-of-arrival estimation.* IEEE Transactions on Acoustics, Speech, and Signal Processing, vol. 38, no. 10, pages 1783–1795, 1990.

[Teunissen 2006] P. J. G. Teunissen. *The LAMBDA Method for the GNSS Compass.* Artificial Satellites, vol. 41, no. 3, pages 89–103, 2006.

[Teunissen 2017] P. J. G. Teunissen et O. Montenbruck, editeurs. Handbook of global navigation satellite systems. Springer, Switzerland, 2017.

[Van Sickle 2023] J. Van Sickle. *The One-percent Rule of Thumb*, 2023. Part of GEOG 862: GPS and GNSS for Geospatial Professionals.

[Van Trees 2001a] H. L. Van Trees. Detection, Estimation, and Modulation Theory, Part III: Radar – Sonar Signal Processing and Gaussian Signals in Noise. J. Wiley & Sons, 2001.

[Van Trees 2001b] Harry L Van Trees. *Radar-Sonar signal processing and Gaussian signals in noise.* (No Title), 2001.

[Van Trees 2002] H. L. Van Trees. Optimum Array Processing. Wiley-Interscience, New-York, 2002.

[Yau 1992] S. F. Yau et Y. Bresler. *A Compact Cramér-Rao Bound Expression for Parametric Estimation of Superimposed Signals.* IEEE Trans. Signal Process., vol. 40, no. 5, pages 1226–1230, May 1992.

ISAE
10, avenue Édouard Belin
BP 54032
31055 Toulouse CEDEX 4